

UCGE Reports  
Number 20356

Department of Geomatics Engineering

**Determining the Polar Cosmic Ray Effect on Cloud  
Microphysics and the Earth's Ozone Layer**

(URL: <http://www.geomatics.ucalgary.ca/graduatetheses>)

by

**Charlene Radons Beckie**

**June, 2012**



UNIVERSITY OF CALGARY

Determining the Polar Cosmic Ray Effect on Cloud Microphysics and the Earth's Ozone  
Layer

by

Charlene Radons Beckie

A THESIS

SUBMITTED TO THE FACULTY OF GRADUATE STUDIES  
IN PARTIAL FULFILMENT OF THE REQUIREMENTS FOR THE  
DEGREE OF MASTER OF ENGINEERING

DEPARTMENT OF GEOMATICS ENGINEERING

CALGARY, ALBERTA

JUNE, 2012

© Charlene Radons Beckie 2012

## Abstract

Earth's changing climate is an important topic where atmospheric ozone plays a critical role. Ozone has a direct influence on the amount and type of solar radiation received by the Earth. This study addresses how cosmic rays may influence the ozone layer by ionizing Earth's atmosphere and enhancing the growth of cloud condensation nuclei and rate of chemical reactions on polar ice cloud surfaces. This theory was largely based on the lifetime work by Lu [2010].

The region of interest was centered over the Thule, Greenland neutron monitor station. Using cosmic ray, satellite-based ISCCP and ICARE project cloud data along with TOMS-OMI-SBUV and TEMIS total column ozone data, data comparisons were done. Plots of cosmic rays versus Antarctic atmospheric ozone from Lu [2009] were reproduced using regional Arctic data and extended to include years from 1983 to 2011. Comparison to research by Harris et al. [2010] was repeated by substituting ice cloud optical thickness for the cloud parameter and seasonal total column ozone for winter stratospheric ozone loss. The results of these data comparisons showed that the regional Arctic view matched very closely to Lu's work from the Antarctic. The ozone 3-point moving average case demonstrated a statistically significant correlation of -0.508. Extending the data duration exposed a cosmic ray data peak that was 14 percent larger than the two previous 11-year cycles. Ice cloud tau / ozone data comparisons did not produce the strong correlations from Harris et al. [2010]. Five years of low stratospheric temperatures and increased volumes of polar stratospheric clouds, identified by Rex et al. [2006], matched significant years of total column ozone minimums. Polar atmospheric CO<sub>2</sub> trended along with ice cloud tau and oppositely to total column ozone, suggesting that lower stratospheric temperatures are instrumental in ozone reduction.

Future work would involve using more extensive datasets, focusing on parameters such as ice water content and effective radius, or altitude specific studies concerning the stratosphere. Continued results from laboratory studies at the CERN facility may lead to

deeper understanding of cosmic ray, cloud microphysics and ozone relationships in nature.

## **Acknowledgements**

I would like to acknowledge my husband, Joe Beckie, for supporting me through the process of advancing my education and allowing my scheduled “overtime” away from the family. I would like to thank my supervisors, Dr. Susan Skone and Dr. Kyle O`Keefe from the University of Calgary for their support of my efforts and flexibility with my schedule.

The people from National Aeronautics and Space Administration (NASA) and the University of Lille in France were exceptionally helpful, willing to answer many of my questions and aid me through my data gathering process. Some of these people were William Rossow, Scientific Contact for the International Satellite Cloud Climatology Project (ISCCP), Susan Tillie, NASA Associate Programmer/Analyst, Julien Delanoë, Nicolas Pascal and Jerome Riedi from the ICARE Project at the University of Lille in France, In addition were John W. Bieber, Paul Evenson and Roger Pyle from the Bartol Research Institute, Gordon Labow, Senior Scientist of SSAI & NASA Goddard Space Flight Center who provided me with NOAA11 and NOAA14 SBUV/2 instrument total ozone profile data. I was also very privileged to have some local support in data working and map generation from Elias Carciente and Beth Young.

I was very fortunate to be allowed access to some very newly modeled and publicized data for my project. The neutron monitors of the Bartol Research Institute are supported by the National Science Foundation. We thank the ICARE Data and Services Center for providing assistance and access to the DARDAR data used in this study.

## **Dedication**

I dedicate this work to my two wonderful children, Lucas and Matthew, who were both born during the time period that it took me to complete this Master of Engineering degree.

## Table of Contents

<b>Abstract</b> .....	ii
<b>Acknowledgements</b> .....	iv
<b>Dedication</b> .....	iv
<b>List of Tables</b> .....	vii
<b>List of Figures</b> .....	viii
<b>List of Symbols, Abbreviations and Nomenclature</b> .....	xiii
<b>CHAPTER 1: INTRODUCTION</b> .....	1
<b>CHAPTER 2: LITERATURE REVIEW</b> .....	5
<b>2.1 Background</b> .....	5
<b>2.1.1 The Ozone Layer</b> .....	5
<b>2.1.2 Chlorofluorocarbons and Their Effect on the Ozone Layer</b> .....	6
<b>2.1.3 Polar Ice Clouds</b> .....	8
<b>2.1.4 Cosmic Ray Theory</b> .....	9
<b>2.2 Previous Theoretical and Laboratory Work</b> .....	15
<b>CHAPTER 3: DATABASES</b> .....	25
<b>3.1 Ozone Data Descriptions</b> .....	28
<b>3.1.1 Satellite Ozone Data</b> .....	28
<b>3.1.1.1 Documented Errors in Ozone Satellite Data Retrievals</b> .....	34
<b>3.1.2 TEMIS Ozone Data</b> .....	35
<b>3.1.2.1 Documented Sources of Error in TEMIS Data Assimilation Technique</b> .....	36
<b>3.2 ISCCP and DARDAR Cloud Data Descriptions</b> .....	38
<b>3.2.1 ISCCP Cloud Data</b> .....	39
<b>3.2.1.1 Documented Errors in ISCCP Measurements</b> .....	49
<b>3.2.2 DARDAR Cloud Data</b> .....	52
<b>3.2.2.1 Documented Errors for the DARDAR ICARE Modeling Technique</b> ...	57
<b>3.3 Cosmic Ray Data</b> .....	59
<b>3.3.1 Cosmic Ray Detection Equipment and Data Sources</b> .....	59
<b>CHAPTER 4: DATA AGGREGATION</b> .....	66
<b>4.1 Ozone Data</b> .....	66
<b>4.1.2 Manipulation of Ozone Data</b> .....	67

4.1.2.1	TOMS-OMI-SBUV Satellite Ozone Data .....	67
4.1.2.2	TEMIS Satellite Ozone Data .....	67
4.1.3.1	TOMS, OMI and SBUV Data .....	68
4.1.3.2	TEMIS Multi-Sensor Data .....	68
4.2	Cloud Data.....	69
4.2.1	Manipulation of Cloud Data .....	71
4.2.1.1	ISCCP Cloud Data .....	71
4.2.1.2	ICARE DARDAR Cloud Data .....	72
4.2.2.1	ISCCP Cloud Data .....	72
4.2.2.2	ICARE DARDAR Cloud Data .....	73
4.3	Cosmic Ray Data .....	75
4.3.1	Manipulation of Cosmic Ray Data .....	75
4.3.2	Treatment of Cosmic Ray Data .....	75
CHAPTER 5:	RESULTS AND DATA ANALYSIS .....	78
5.1	Cosmic Ray and Polar Ice Cloud Comparisons .....	78
5.2	Cosmic Ray and Total Column Ozone Comparisons .....	92
5.3	Polar Ice Cloud and Total Column Ozone Comparisons .....	108
5.4	Other Data Comparisons .....	114
CHAPTER 6:	CONCLUSIONS AND FUTURE WORK .....	118
6.1	Conclusions .....	118
6.2	Recommendations .....	119
REFERENCES	.....	121
Publications	.....	121
Websites and Other References	.....	124
APPENDIX A	.....	128
APPENDIX B	.....	130
APPENDIX C	.....	132
APPENDIX D	.....	135

## List of Tables

<b>Table 3.1: Description of dependencies for radiance satellite retrievals in determining atmospheric ozone profiles. [Corprew, 1997]</b> .....	30
<b>Table 3.2. Input satellite retrieval datasets used in the Multi-Sensor Reanalysis of Total Ozone Project [from Van der A et al., 2010].</b> .....	35
<b>Table 3.3: Assimilation process corrections applied to satellite datasets used in the Multi-Sensor Reanalysis of Total Ozone project [from Van der A et al., 2010].</b> .....	37
<b>Table 3.4: Definitions of liquid and ice clouds for each cloud type based on ranges of mean cloud top temperature and tau. [from Rossow et al., 1996].</b> .....	48
<b>Table 3.5. Cloud cover fraction accuracy showing contributing variables and their effects on the ISCCP data [from Rossow and Schiffer, 1999].</b> .....	51
<b>Table 3.6: Threshold corrections applied to the ISCCP datasets resulting in improved detection limits of cloud top height and cloud optical thickness for total cloud cover [from Rossow and Schiffer, 1999].</b> .....	52
<b>Table 3.7: Satellite missions and their contributions towards data retrievals of cloud properties [from Delanoë and Hogan, 2010].</b> .....	53
<b>Table 3.8: Error sources from Forward Modeling work in combining CloudSat-CALIPSO and MODIS retrievals [from Delanoë and Hogan, 2010].</b> .....	58
<b>Table 4.1: Summary of both Individual Satellite and TEMIS Multi-Sensor Time Series data annual seasonal ozone reduction from 1983 to 2011, for available data.</b> .....	69
<b>Table 4.2. Date ranges of available cloud data over Thule, Greenland; representing ISCCP data on left (columns 2 to 4) and DARDAR ICARE data on right (columns 5 to 7).</b> .	74
<b>Table 5.1: Correlation coefficient results after comparing the percentage variance of the Thule, Greenland cosmic ray intensity to both the TOMS-OMI-SBUV and TEMIS multi-sensor ozone datasets.</b> .....	105

## List of Figures

<b>Figure 2.1: Recorded CFC (single type) concentration over several stations; Alert, Nunavut being of interest for Arctic studies [Barry, 2000].</b>	8
<b>Figure 2.2: Artist depiction of the Heliosphere showing inbound route of Galactic Cosmic Rays as they encounter the Bow Shock, Heliopause and Termination Shock before entering Earth’s Solar System [NASA, 2001].</b>	10
<b>Figure 2.3: Cosmic Ray Intensity as a percentage of 1954 minimum modulation level plotted against Smoothed Sunspot Number to show the inverse relationship [from Ulysses website, University of New Hampshire].</b>	11
<b>Figure 2.4: Depiction of how unipolar space charge collects at the top and bottom of clouds due to the drift ions from cosmic rays [from Kirkby, 2007, with permission].</b>	13
<b>Figure 2.5: “Ion-induced nucleation of new particles from trace condensable vapours and water in the atmosphere” [from Kirkby, 2007, with permission].</b>	14
<b>Figure 2.6: Saturation ratio and critical supersaturation plots [Harrison, and Ambaum, 2008, with permission].</b>	14
<b>Figure 2.7: Percentage variations of cosmic ray intensity and annual Antarctic mean total ozone data from the two neutron monitor stations [from Lu, 2009, with permission].</b>	19
<b>Figure 2.8: Percentage variations of observed Cosmic Ray intensity, averaged from three neutron monitor stations, and monthly average zonal mean total ozone in October in the Antarctic [from Lu, 2009, with permission].</b>	19
<b>Figure 2.9: Integrated ozone loss as a function of polar stratospheric cloud volume [Harris et al., 2010, with permission].</b>	22
<b>Figure 2.10: Plot of ion concentration in the atmospheric pressure reaction chamber versus the formation rate of aerosols at 4 nm, as measured by the condensation particle counter at CERN. Error bars represent the statistical measurement uncertainties [Enghoff et al., 2011, with permission].</b>	23
<b>Figure 3.1: Satellite retrieval co-ordinate space, centered on the Thule, Greenland station.</b>	25
<b>Figure 3.2: Summary of ozone, cloud and cosmic ray data sources.</b>	27
<b>Figure 3.3: Depiction of time-lapse changes in total ozone over the Arctic showing BUW and TOMS satellite readings from March 1971 to March 2000 [from Newman, 2000].</b>	32
<b>Figure 3.4: Depiction of year-to-year changes in daily average total ozone (DU), over the Arctic, from OMI satellite retrievals on March 19, 2010 and 2011 [from Remer, 2011].</b>	34

Figure 3.5: “Fitted offset (MSR-ground) between the MSR level 4 assimilation data and all selected ground measurements for the period 1978-2008” [from Van der A et al., 2010, with permission].	38
Figure 3.6: ISCCP Cloud Analysis Procedure illustrating how data retrievals are handled in the process to output D1 and D2 data types [from Rossow et al., 1996, with permission].	40
Figure 3.7: “Schematic illustrating different assumptions about variations of optical media used to model radiative transfer through cloudy atmospheres [from Rossow et al., 2002, with permission].	43
Figure 3.8: “Observed relationship of $\epsilon_{IR}$ and $\epsilon$ for all special study areas. “ [from Rossow et al., 2002, with permission].	46
Figure 3.9: “(a) Estimated values, $\epsilon_{IR}'$ , vs the true values, $\epsilon_{IR}$ and (b) Estimated values of emissivity, $E'$ , vs. the true values, $E$ “ [from Rossow et al., 2002, with permission].	46
Figure 3.10: “Seasonal variations of $\epsilon$ for high-, mid-, and low-level clouds averaged over the whole globe and over three latitude zones (tropical = $\pm 15^\circ$ , mid-latitudes = $\pm 30-60^\circ$ , high latitudes = $\pm 60-90^\circ$ ) “ [from Rossow et al., 2002, with permission].	47
Figure 3.11: “Conditions for cloud changes based on atmospheric vapour inputs and cooling effects“ [from ISCCP Webmaster, 2005].	49
Figure 3.12: Flowchart detailing the retrieval scheme used in the ICARE modeling technique producing the DARDAR data products [from Delanoë and Hogan, 2008].	54
Figure 3.13: An atmospheric proton-molecule collision. In showers of GCRs, this type of collision can produce billions of particles known as secondary cosmic rays, resulting in an atmospheric cascade [Spaceship Earth, 2000].	60
Figure 3.14: “Standard (BP-28 proportional tubes) NM-64 calculated detection efficiency for secondary particles arriving in the vertical direction“ [from Clem and Dorman, 2000, with permission].	61
Figure 3.15: “Calculated yield function spectra of NM-64 counts at sea level from vertical incident primary protons is shown. The individual contributions made by secondary components to the vertical proton yield function are separated into different curves. “ [from Clem and Dorman, 2000, with permission].	62
Figure 4.1: An example of CloudSat satellite retrieval coverage from the orbital path “quicklook” images for July 23, 2010, showing the flight path over Thule station in northwest Greenland [from ICARE, 2012].	71
Figure 4.2: An example of a “quicklook” image showing radar reflectivity over the Greenland segment of cloud retrievals for July 23, 2010 [from ICARE, 2012].	71
Figure 4.3: Neutron monitor network. Nine of the high geographic latitude stations (filled circles) are able to view the “equatorial region after accounting for bending of particle trajectories in the geomagnetic field, while Thule and McMurdo (MC)	

generally view the northern and southern hemispheres, respectively” [Bieber et al., 2004].	76
Figure 4.4. “Count rate recorded during the Tasmania-Bartol 1994–1995 latitude survey compared with various derived count rates” [from Clem and Dorman, 2000, with permission].	77
Figure 5.1: Ice cloud tau monthly mean data from the ISCCP database from July 1983 to June 2008.	79
Figure 5.2: Percentage variance of cosmic ray intensity plotted against the ISCCP ice cloud tau monthly mean values from July 1983 to June 2008.	80
Figure 5.3. Five-point moving averages of percentage variances of both cosmic ray intensity and ISCCP ice cloud tau monthly mean values from July 1983 to June 2008.	80
Figure 5.4: The calculated number of days per month, from 1983 to 2008, that ice clouds were detected based on the ice cloud tau values from the ISCCP database.	82
Figure 5.5: Percentage variance of cosmic ray intensity and ISCCP Ice Cloud Detection in number of days per month. Peaks in ice cloud detection are indicated by red arrows.	83
Figure 5.6. Percentage variances of ice cloud tau and DARDAR ice cloud optical thickness over the period of dataset overlap between June 2006 and June 2008.	85
Figure 5.7: Ice cloud optical thickness monthly mean from the ICARE DARDAR database from June 2006 to December 2010.	86
Figure 5.8: Percentage variance monthly mean values of cosmic ray intensity and DARDAR ice cloud optical thickness from June 2006 to December 2010.	87
Figure 5.9: Five-point moving averages of percentage variance of both cosmic ray intensity and the DARDAR ice cloud optical thickness monthly mean values from June 2006 to December 2010.	88
Figure 5.10: Number of days per month (2006 to 2011) that ice clouds were detected based on the ice cloud optical thickness parameter from the ICARE DARDAR database.	90
Figure 5.11: Percentage variance of cosmic ray intensity plotted against ice cloud detection from the DARDAR ICARE project in number of days per month.	91
Figure 5.12: Percentage variations of observed cosmic ray intensity and annual mean total ozone for the period of 1983 to 2011.	93
Figure 5.13: Percentage variations of observed cosmic ray intensity and March to August month of maximum loss expressed as monthly mean total ozone for the period of 1983 to 2011.	94
Figure 5.14: Percentage variations of observed cosmic ray intensity and annual mean total ozone 3-point moving average for the period of 1983 to 2011.	95

<b>Figure 5.15: Percentage variations of observed cosmic ray intensity and March to August month of maximum loss expressed as monthly mean total ozone 3-point moving average for the period of 1983 to 2011. ....</b>	<b>96</b>
<b>Figure 5.16: Monthly ozone loss computed as a percent from the TEMIS multi-sensor dataset, representing the time frame from 1983 to 2008.....</b>	<b>98</b>
<b>Figure 5.17: The relationship between neutron monitor cosmic ray intensity data, as a percentage variance, and the seasonal reduction in total ozone over Thule, Greenland.....</b>	<b>102</b>
<b>Figure 5.18: Comparison of total column ozone values from the TOMS-OMI-SBUV collection of satellite data versus the TEMIS Multi-sensor data collaboration.....</b>	<b>104</b>
<b>Figure 5.19: Percentage variance of cosmic ray intensity data charted against the seasonal reduction in total ozone over Thule, Greenland. ....</b>	<b>106</b>
<b>Figure 5.20: Comparison of cosmic ray intensity data and monthly differences in total column ozone from TOMS-OMI-SBUV satellite sources over Thule, Greenland.....</b>	<b>107</b>
<b>Figure 5.21. Comparison of cosmic ray intensity data and monthly differences in total column ozone based on TEMIS multi-sensor data over Thule, Greenland.....</b>	<b>108</b>
<b>Figure 5.22: Satellite ISCCP ice cloud tau annual mean data versus TEMIS multi-sensor annual ozone loss data from 1983 to 2008. ....</b>	<b>110</b>
<b>Figure 5.23: Satellite ISCCP ice cloud tau annual mean data versus TOMS-OMI-SBUV satellite annual ozone loss data from 1983 to 2008.....</b>	<b>110</b>
<b>Figure 5.24: Satellite-based ISCCP annual ice cloud persistence versus TOMS-OMI-SBUV satellite annual ozone loss data from 1983 to 2008.....</b>	<b>111</b>
<b>Figure 5.25: Satellite-based ISCCP annual ice cloud persistence versus TEMIS multi-sensor annual ozone loss data from 1983 to 2008. ....</b>	<b>111</b>
<b>Figure 5.26: Satellite ICARE DARDAR ice cloud optical thickness annual mean data versus TEMIS multi-sensor annual ozone loss data from 2006 to 2010. ....</b>	<b>112</b>
<b>Figure 5.27: Satellite ICARE DARDAR ice cloud optical thickness annual mean data versus TOMS-OMI-SBUV satellite annual ozone loss data from 2006 to 2010. ....</b>	<b>112</b>
<b>Figure 5.28: Satellite-based ICARE DARDAR annual ice cloud persistence versus TOMS-OMI-SBUV satellite annual ozone loss data from 2006 to 2010. ....</b>	<b>113</b>
<b>Figure 5.29: Satellite-based ICARE DARDAR annual ice cloud persistence versus TEMIS multi-sensor annual ozone loss data from 2006 to 2008. ....</b>	<b>113</b>
<b>Figure 5.30: Volume of PSCs sourced from the ECMWF database, computed for temperatures between 380 and 550 K [from Rex et al., 2006, with permission]. ....</b>	<b>115</b>
<b>Figure 5.31: CFC-11 insitu gas chromatograph daily averages from NOAA/ESRL Radiatively Important Trace Species (RITS) and Chromatograph for Atmospheric Trace Species (CATS) programs from Barrow, Alaska (71.3 N, 156.6 W, elevation: 8 m) and Summit, Greenland (72.58 N, 38.45 W, elevation: 3238 m).....</b>	<b>116</b>

**Figure 5.32: Atmospheric Carbon Dioxide (CO<sub>2</sub>) as measured at Alert, Canada for the period of 1975 to 2009 [from Environment Canada, 2012]. .....117**

## List of Symbols, Abbreviations and Nomenclature

BF <sub>3</sub>	boron trifluoride
BRI	Bartol Research Institute
BUV	backscatter ultraviolet
CATS	Chromatograph for Atmospheric Trace Species (NOAA/ESRL programs)
CCD	charge-coupled device
CCN	Cloud Condensation Nuclei
CERN	Conseil Européen pour la Recherche Nucléaire (European Council for Nuclear Research)
CFC	Chlorofluorocarbon
CO <sub>2</sub>	Carbon dioxide
CF <sub>3</sub> Cl	Chlorotrifluoromethane
DARDAR	raDAR/liDAR
DAYNIT	day-night flag (ISCCP parameter)
DEA	dissociative electron attachment
DOAS	Differential Optical Absorption Spectroscopy
DU	Dobson units
DX	Stage of pixel level cloud product used in the ISCCP project
ERA	ECMWF Re-Analysis
ESRL	Earth System Research Laboratory
ECMWF	European Centre for Medium-Range Weather Forecasts
FMI	Finnish Meteorological Institute
GCM	Global Atmospheric Circulation Models
GDP	GOME Data Processor (NL-SCIA-DC)
GOME	Global Ozone Monitoring Experiment
HDF	Hierarchical Data Format
ICARE	Interactions Clouds Aerosols Radiation Etc.
IFOV	instantaneous field of view
IR	infrared
ISCCP	International Satellite Cloud Climatology Project
iwc	ice water content
Kr	Krypton
MSR	Multi-Sensor Reanalysis
N11	NOAA 11 SBUV/2 ozone monitoring instrument
N14	NOAA 14 SBUV/2 ozone monitoring instrument
NASA	National Aeronautics and Space Administration
NIVR	Netherlands Agency for Aerospace Programmes
NL-SCIA-DC	The Netherlands SCIAMACHY Data Center
NO <sub>2</sub>	Nitrogen dioxide
NOAA	National Oceanic and Atmospheric Administration
NO <sub>x</sub>	Nitrogen Oxides (NO + NO <sub>2</sub> )
O <sub>2</sub>	Oxygen

O <sub>3</sub>	Ozone
OCIO	Chlorine Dioxide
OMI	Ozone Monitoring Instrument
OMIDOA03	OMI DOAS Ozone data product (TEMIS)
OMTO3	Aura OMI Total Ozone data product (NASA)
POEM	Polar-Orbit Earth Observation Mission
PSC	Polar Stratospheric Cloud
RITS	NOAA/ESRL Radiatively Important Trace Species (NOAA/ESRL programs)
RMS	Root Mean Square
RTS	Random Telegraph Signal
SAGE	Stratospheric Aerosol and Gas Experiment
SATTYP	SATellite TYPEs (ISCCP parameter)
SBUV	Solar Backscatter Ultra Violet
SCIAMACHY	SCanning Imaging Absorption SpectroMeter for Atmospheric CHartographY
SGP	SCIAMACHY GOME Processor (NL-SCIA-DC)
SO <sub>2</sub>	Sulfur Dioxide
SSAI	
SZA	Solar Zenith Angle
TEMIS	Tropospheric Emission Monitoring Internet Service
THEMIS	Thermal Emission Imaging System
TIROS	Television and Infrared Operational Satellite
TM3DAM	Tracer transport Model 3 ozone Data Assimilation Model
TMPTAB(VPRSIC)	VIS-adjusted ice cloud top pressure (ISCCP parameter)
TMPTAB(VTAUIC)	VIS-retrieved ice cloud tau (ISCCP parameter)
TMPTAB(VTMPIC)	VIS-adjusted ice cloud top temperature (ISCCP parameter)
TOGOMI	Total Ozone algorithm for GOME using the OMI algorithm
TOSOMI	Total Ozone algorithm for SCIAMACHY using the OMI algorithm
TOMS	Total Ozone Mapping Spectrometer
TOVS	TIROS Operational Vertical Sounder
TPD	temperature-programmed desorption
US	United States
UV	Ultra Violet
VIS	VISible
VZA	Viewing Zenith Angle
WCRP	World Climate Research Program
WOUDC	World Ozone and Ultraviolet Data Center

### Equation Variables

$A - Pair$	Variable used to define wavelengths from 313 to 331 nm used in ozone computations
$a_{\ln S}$	slope describing $\ln(S)$ as sampled by lidar (DARDAR)

$a_{mn}$	the primary variation amplitudes (BRI)
$\alpha$	variable used in ISCCP cloud computations defined as $\frac{1+\sigma_{ext}l_c}{\sigma_{ext}l_c}$
$\alpha_v$	visible extinction coefficient (DARDAR)
$b$	coefficient that uses cloud particle phase to relate visible to infrared
	optical thickness (ISCCP).
$b_{lnS}$	the cloud middle value of $\ln(S)$ , as sampled by lidar (DARDAR)
$B' - Pair$	Variable used to define wavelengths from 318 to 340 nm used in ozone computations
$\beta$	attenuation or barometric coefficient (BRI)
$c_{mn}$	the coupling coefficients (BRI)
$C - Pair$	Variable used to define wavelengths from 331 to 340 nm used in ozone computations
C14	unstable isotope of carbon
CF <sub>2</sub> Cl	chlorodifluoromethane
CF <sub>2</sub> Cl <sub>2</sub>	dichlorodifluoromethane
CFCl <sub>2</sub>	dichlorofluoromethane
$\chi_{11}$	phase of the diurnal variation (BRI)
Cl	chlorine
Cl <sup>-</sup>	chlorine ion
Cl <sub>2</sub> (g)	chlorine molecule, gaseous form
Cl <sub>2</sub> O <sub>2</sub>	dichlorinedioxide
ClONO <sub>2</sub> (g)	chlorine nitrate
ClOO	chlorinedioxide
$D_m$	the normalized particle size (DARDAR)
$dN$	the variation in the count rate $N$ (BRI)
$\delta N_{10}$	North-South anisotropy (BRI)
$\delta N_{11}$	diurnal variations (BRI)
$dp$	the barometric pressure change
$E$	definition of emissivity (ISCCP)
$E_{pp}$	the plane-parallel homogeneous emissivity (ISCCP)
$e^-$	electron
$\epsilon$	inhomogeneous remote sensed cloud field (ISCCP)
$\epsilon_{IR}$	the redefinition of $\epsilon$ in infrared signals (ISCCP)
$\epsilon'_{IR}$	emissivity of homogeneous cloud cover, based on pixel-level data from 16 regions (ISCCP)
cloud	
$\epsilon_p$	the correction factor for an inhomogeneous cloud particle density distribution (ISCCP)
$e_s^-$	self-trapped electron
F	the unified size distribution shape (DARDAR)
F <sup>-</sup>	fluoride ion
$F(i)$	the direct solar radiation at wavelength $i$

$g$	an asymmetry parameter used in ISCCP cloud particle derivations
$\gamma$	photon
$H_2O$	water
$HCl(s)$	hydrogen chloride, solid form
$HNO_3(s)$	nitric acid, solid form
$h\nu$	solar light
$I(i)$	backscatter radiance at a particular wavelength $i$ (TOMS)
$I\alpha(i)$	atmospheric component of radiance at wavelength $i$ (TOMS)
$Ig(i)$	contributions of surface reflectance at wavelength $i$ (TOMS)
$j(P_R)$	primary particle intensity spectrum (BRI)
$J_z$	vertical current density
$l_c$	the effective correlation length of the variations in ISCCP
$\ln(S)$	a factor that changes with altitude (DARDAR):
$L$	a parameter used to describe the evaluation over an extensive area,
	much greater than $\lambda$ in the equations for ISCCP
$M_n$	the $n^{\text{th}}$ moment of the ice particle size distribution (DARDAR)
$\mu$	muon
$n$	the number of samples being compared in the two-tailed
statistical	test
$n$	neutron
$N$	counting rate developed from near or at sea-level stations (BRI)
$N_{14}$	nitrogen isotope
$N'$	state vector relationship as a function of temperature
$N(D)$	shape-particle size distribution used in forward modeling
(DARDAR)	
$N(i)$	N Value used in TOMS ozone calculations expressed as $-100 \log \left[ \frac{I(i)}{F(i)} \right]$
$N_0$	the normalization value (BRI)
$N_0^*$	the “normalized number concentration parameter” (DARDAR)
$NH_3$	ammonia
$O_{16}$	oxygen isotope
$p$	atmospheric pressure in mmHg (BRI)
$P$	proton
$\pi$	pion
$P_c$	cloud top pressure
$P_{gc}$	the geomagnetic cutoff rigidity (BRI)
$P_R$	primary cosmic ray rigidity (BRI)
$P_s$	scene pressure
$P_t$	terrain pressure (both in units of mb)
$r$	correlation coefficient for the datasets
$R$	the Lambertian reflectivity of the lower boundary (TOMS)

$R$	the radiative transfer operator that determines the optical
thickness	radiative flux (ISCCP)
$R_c$	columnar resistance of Earth's atmosphere
$r_e$	Effective radius (DARDAR)
$\rho$	the radius of a circle passing through points (0,0) and (1,1) and
that	fits the curvature of the emissivity relationship (ISCCP)
$\rho_i$	the density of solid ice (DARDAR)
$\phi_{11}$	effective asymptotic longitude of the station (BRI)
$s$	unit vector in any arbitrary direction (ISCCP)
$S$	extinction-to-backscatter ratio (DARDAR)
$S(i)$	the portion of radiation, at wavelength $i$ , that goes through
multiple	reflections between the earth and atmosphere before being
	transmitted away from the earth to be detected by the satellite
	(TOMS)
$\sigma_{ext}$	the extinction cross section in cloud computations (ISCCP)
$t$	two-tailed result
$T$	temperature in degrees Celsius (DARDAR)
$T_{eff}$	the effective ozone temperature, in degree Celcius (TEMIS)
$T(i)$	signal retrieved from both the direct plus the diffuse radiation
	reaching the surface and diffusely reflecting back to the satellite
	(TOMS)
$\tau$	cloud tau used in ISCCP analysis
$\tau'$	effective cloud tau (ISCCP)
$\bar{\tau}$	linear mean describing first moment (ISCCP)
$\hat{\tau}$	Radiative mean describing first moment (ISCCP)
$\hat{\tau}'$	the corrected mean cloud tau given by $(1 - \epsilon)\bar{\tau}$
$\tilde{\tau}$	Logarithmic mean describing first moment (ISCCP)
$V$	the relative density of the ISCCP particle density distribution
$V_l$	ionospheric potential
$w$	weighting function that accounts for the presence of surface snow
	or ice in the scene and the conditions of surface reflectivity at
1000	mb
$\omega_0$	single scatter albedo used in ISCCP computations
$x$	state vector (DARDAR)
$X_{corr}$	the corrected ozone value in DU
$X_{dobson}$	the original total ozone value from the ground-based ozone
dataset	in DU
$Y$	the optical path (the line integral of extinction) used in ISCCP
$Z$	unit vector in the vertical direction (ISCCP) or altitude (DARDAR)
$z_{mid}$	height measuring the middle of the cloud,

## CHAPTER 1: INTRODUCTION

Many questions concerning global climate change have arisen since the onset of an ozone hole that was discovered over the Antarctic in 1980 and monitored ozone thinning over the Arctic in the 1990s. Ozone is a naturally occurring molecule in Earth's atmosphere that forms a layer that encircles the globe at about 18 km altitude. This layer protects Earth and living organisms from harmful radiation received from the sun. Ozone layer variability has been linked to changes in stratospheric temperatures, ultimately altering global wind and precipitation patterns and effecting ocean-atmospheric cycles [Meehl et al., 2009].

Besides natural sources of pollutants, the period from the industrial revolution until now introduced the release of masses of new chemicals into Earth's atmosphere due to anthropogenic activity. From this, substantial volumes of chlorofluorocarbons (CFCs), carbon dioxide (CO<sub>2</sub>), nitrogen oxides (NO<sub>x</sub>), and other chemicals now exist in the troposphere. Photolysis of CFCs breaks down dichlorine peroxide (Cl<sub>2</sub>O<sub>2</sub>) into its constituents, resulting in chlorine radicals. These radicals easily react with weakly bonded oxygen atoms in ozone (O<sub>3</sub>) resulting in ClO and oxygen (O<sub>2</sub>). From modeling work, these reactions only contribute to 40% of the total ozone loss, leaving 60% due to currently unexplained mechanisms [Schiermeier, 2007].

Recent studies have examined a possible process that can help to complete the picture of deterioration of the ozone layer. This involves the enhancement of chemical reactions on ice surfaces within clouds with the influence of galactic cosmic rays. Cosmic rays enter Earth's atmosphere during times of reduced solar activity and increase the ionization of the atmosphere below 70 km altitude with a maximum over the poles at about 18 km altitude [Muller, 2003].

In 1999, intriguing evidence from laboratory studies revealed a four-magnitude enhancement of Cl<sup>-</sup> yield from CFCs in the case of electron-stimulated desorption in the

presence of both polar molecules and a cooled rare gas or water film, simulating polar environments [Lu, 1999]. Additional studies and theories were developed since this time, providing credence to the original concept and further evidence of molecular changes during dissociative electron attachment (DEA) processes and vibrational excitation states. Time-series studies were attempted to show relationships that existed between cosmic rays and ozone depletion that exist in nature.

This study will further examine the initial question of global climate change due to ozone layer depletion. The main objective of this research is to establish the strength of the relationships between cosmic ray intensity and polar ice cloud microphysics (optical thickness /  $\tau$ ) as these parameters relate to atmospheric total column ozone in the Arctic. Some of the development of data comparisons will be based on work by Lu [2009] and Harris [2010] using time series data.

For the current study, the Arctic was chosen due to the nature of ozone reduction during the spring and summer, to ensure that a full scale of change would be identified, where areas of the ozone hole and values of near-zero ozone thickness would not be encountered. Additionally, until recently, much of the previously published work of this type was focused on the Antarctic where the ozone hole was initially detected and where most ground-based monitoring stations were first established. Data availability due to satellite monitoring, with access to polar-orbiting weather satellites, allows much-needed retrievals to now be available for study purposes using Arctic data.

Cosmic ray data will be correlated with VIS retrieved average daily ice cloud  $\tau$  and optical thickness measurements to determine which months and /or years host the most suitable atmospheric conditions for chemical reactions to take place on cloud particle surfaces. This data will then be correlated with atmospheric ozone to find if either the influence of cosmic rays or ice cloud  $\tau$  alone or in tandem may compromise the seasonal total thickness of the ozone layer.

From theory, the results are hypothesized to show the greatest periods of springtime polar ozone loss to correlate the most strongly with the annual heightened values of both cosmic ray activity and the presence of polar ice clouds. Any possible causal nature between these elements in the atmosphere will be discussed.

Data gathering and reworking will be the first stage of this process. Several different sources will be used to build a complete dataset for each of the data types from 1983 to the most recent data retrievals (2011). Subsets will be created to portray the area of study which is an approximate 300 square km grid centered over the Thule, Greenland Neutron Monitor station at the U.S. Air Force Base.

This paper is organized as follows. Chapter 2 contains a literature review that provides vital background information on the ozone layer, the impact of chlorofluorocarbons on the ozone layer, polar ice clouds, and the cosmic ray theory. This second chapter will also detail previous theoretical and laboratory work based on studies conducted by the main research and theoretical analysts in the field, outlining their prominent work published between 2006 and 2011. Chapter 3 shows the regional study area for all data retrievals and provides a comprehensive look at the databases used as input for this thesis. This chapter examines two sources for ozone data; the first being a generated collection of Total Ozone Mapping Spectrometer (TOMS), Ozone Monitoring Instrument (OMI) and the solar backscatter ultraviolet (SBUV) data (1983 to 2011) and the second, a modeled resource from 1983 to 2008 obtained from the Tropospheric Emission Monitoring Internet Service (TEMIS, 2011). It also provides information on two sources of Arctic ice cloud data being the International Satellite Cloud Climatology Project (ISCCP) and raDAR/liDAR (DARDAR) Interactions Clouds Aerosols Radiation Etc. Thematic Centre (ICARE) project data. These data span the years of 1983 to 2008 and 2006 to 2010, respectively. The cosmic ray data is described in Chapter 3 with its source being the Thule, Greenland neutron monitor station (1983 to 2011). Each of these database descriptions includes

sources of error. Chapter 4 describes how the data was aggregated, providing details of the types of manipulation and treatment administered to each of these datasets. Chapter 5 documents the results from the study and relevant discussion around these outcomes. Chapter 6 summarizes the paper with conclusions and future recommendations. The final sections include the references and appendices for the paper.

## CHAPTER 2: LITERATURE REVIEW

### 2.1 Background

#### 2.1.1 The Ozone Layer

Living organisms are able to persist on the Earth due to protective mechanisms that allow a balance between our solar system and the environment of land and oceans. As Earth moves and rotates through space, particles from the Sun and galaxy constantly bombard the Earth. The solar wind and heliomagnetic field, geomagnetic field and Earth's atmosphere act as shields from these particles. The ozone layer within the atmosphere plays a key role in protecting the Earth from excess solar radiation. Ozone is a naturally occurring molecule in Earth's atmosphere. It forms a layer, of varying thickness, with its greatest global concentrations between 20 and 25 km altitude, ranging from 2 to 8 ppm [Gleason, 2008].

The natural ozone layer normally demonstrates latitudinal and seasonal variations. The column is normally thinner near the equator and thicker towards the poles while it is generally thicker during spring and thinner during autumn. During winter, the ozone column recovers near the poles due to stratospheric wind patterns known as Brewer – Dobson circulation. This circulation pattern moves ozone, created over the tropics at a high altitudes, pole ward and downward to the lower stratosphere. This slow circulation pattern takes 4-5 months for atmospheric molecules to drop in altitude by 4 km. The highest amounts of ozone normally occur in the Arctic occur in March-April where the greatest amounts of columnar ozone exists world-wide. Variables known to influence ozone loss as they relate to polar stratospheric cloud presence include "denitrification, solar exposure, initial chemical fields, descent rates, in-mixing, vortex inhomogeneities and vertical extent" [Harris et al., 2010].

Depletion of ozone over certain parts of the Earth exposes living organisms to harmful Solar UVA, UVB and UVC, the latter of which is most damaging and of highest energy, and is normally completely blocked by the ozone. Besides its negative effect on organisms,

ozone loss was shown to cause a stratospheric cooling and localized tropospheric and surface temperature warming of the Earth at the poles. These changes effectively alter the ocean-atmospheric cycles [Meehl et al., 2009].

The ozone layer was researched extensively after the initial identification of the ozone hole found in the Antarctic during the mid-1980s. Further ozone loss was detected in the 1990s over the Arctic polar region. Due to the dynamic and complex nature of Earth's atmosphere, modeling efforts have only accounted for about 40% of atmospheric ozone loss due to photolytic processes [Schiermeier, 2007]. More specifically, application of current understanding, common reaction kinetics and standard assumptions around atmospheric chlorine and bromine concentrations to the models, the recent accelerated rate of ozone loss was not predicted [Frieler et al., 2006]. The remaining ozone depletion must be accounted for by changes to modeling techniques, improvement in understanding loss rates and currently undefined or unaccounted for processes.

### **2.1.2 Chlorofluorocarbons and Their Effect on the Ozone Layer**

From past research, the loss of polar ozone was mainly attributed to chemical dispersion of chlorofluorocarbons (CFCs), hydrochlorofluorocarbons (HCFCs), hydrobromofluorocarbons, hydrofluorocarbons, hydrocarbons, perfluorocarbons and halons and the resultant reactions due to photolysis (U.S. Environmental Protection Agency, 2012). From the photolysis of these chemicals, free radical catalysts such as nitric oxide (NO), hydroxyl (OH) and atomic chlorine and bromine result and react with ozone to break it down [Welch, 2011].

Since the 1930s, these chemical compounds have been released into the air due to daily anthropogenic activities, mainly over mid-latitude regions. Industrial and personal use of refrigerants, aerosols, fumigants, solvents and industrial processes were the main sources for the chemicals. The Montreal Protocol was developed to phase out the use of particular HCFCs that were determined to cause the most extensive damage to the ozone layer of the Earth [Welch, 2011]. Their longevity, with lifetimes ranging from 50 to over

100 years in length, makes these chemicals a major threat to the atmospheric ozone layer. “The total halogen level in the lower atmosphere was measured to peak in 1994 and the equivalent effective stratospheric chlorine over the Antarctica was estimated to peak around 2000 ppt with a given delay of  $6 \pm 3$  years” [Lu, 2010a].

The process of breakdown of CFCs normally occurs in a photolytic reaction such as in the following consideration of  $\text{CF}_2\text{Cl}_2$ .



where  $h\nu$  is defined as solar light.

These free Cl and F atoms are able to bond with other molecules in the atmosphere to form inorganic compounds such as HCl and  $\text{ClONO}_2$  [Lu, 2010a]. Although these reactions are predicted to occur at 40 km height in the tropical stratosphere, ozone breakdown typically transpires over the Arctic in the northern hemispheric during springtime at about 18-20 km altitude. For this breakdown to occur, these inorganic species are transported pole-ward and to lower altitudes by circulatory patterns of winds following atmospheric pressure gradients, known as Hadley and Ferrell cells, following a similar transport route to that of ozone [Lu, 2010a, Atmospheric Circulation, 2001]. Over time, this isentropic transport causes significant accumulations of aerosols in the polar atmosphere. These accumulations have interfered with aircraft pilots’ vision for over 20 years and this issue was supported by ground-based station measurements. The maximum mass concentrations of these aerosols, relating to anthropogenic sources, are known to occur in late winter and early spring [NOAA, 2008]. An example of CFC-11 concentrations over several world-wide stations, including Alert, Nunavut from the period of 1977 to 1998 is shown in Figure 2.1.

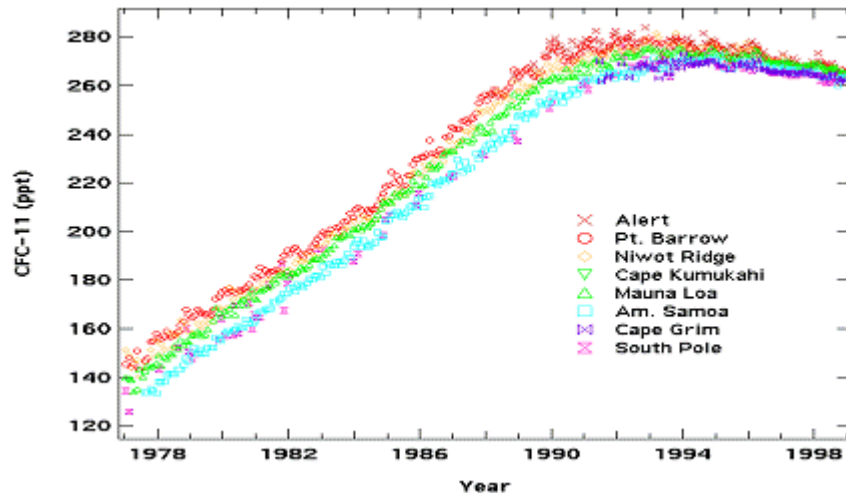


**Figure 2.1: Recorded CFC (single type) concentration over several stations; Alert, Nunavut being of interest for Arctic studies [Barry, 2000].**

### 2.1.3 Polar Ice Clouds

Several unique conditions come together in the Arctic atmosphere that effectively enhance chemical reactions and account for ozone loss. Changes in the solar radiation cycle, energy fluxes and albedo cause seasonal variations in Arctic temperatures. Cold temperatures in the Arctic atmosphere allow polar stratospheric ice clouds (PSCs) to form. These clouds contain a percentage of either water or nitric acid ice molecules and can be several kilometers in thickness [Tachikawa and Abe, 2007]. Reactions such as the following (Equation 2.2) take place in the presence of PSCs and are enhanced by their irregular shaped molecular surfaces:



This key step in ozone depletion is predicted to be amplified where these PSCs exist in the presence of greater ionization in the atmosphere. The ionization budget below 70 km altitude is primarily sourced by cosmic rays entering Earth's atmosphere [Muller, 2003 and Lu, 2010a].

#### **2.1.4 Cosmic Ray Theory**

Cosmic rays are charged particles, mainly consisting of protons and helium nuclei, which have kinetic energies of greater than 1 MeV. There are three classes of cosmic rays including galactic, anomalous and solar cosmic rays. Galactic cosmic rays (GCRs) are output from explosive events such as supernovae and are accelerated for travel through space at these event shock fronts. They mainly contain protons and other fully ionized atoms with an energy range from 1-20 GeV and a spectral peak at 2 GeV. They are the dominant source of stratospheric and tropospheric ionization on Earth. This ionization has the potential to reach to heights of 35 km, but due to forces within the Earth's atmosphere, the ionization reaches a maximum between 15 and 18 km over both land and oceans. At this height, ion-pair production rates are between 20 and 50  $\text{cm}^{-3}\text{s}^{-1}$  [Kirkby, 2007]. Anomalous cosmic rays begin as neutral particles that exist within the interstellar wind. They drift across the heliopause and become singly ionized atoms that are accelerated in this region or at the termination shock of the heliosphere (Figure 2.2). Solar cosmic rays are charged particles having 100s MeV energies that originate at the shock front of coronal mass ejections or other explosive events on our Sun. They may become accelerated further at interplanetary shock fronts.

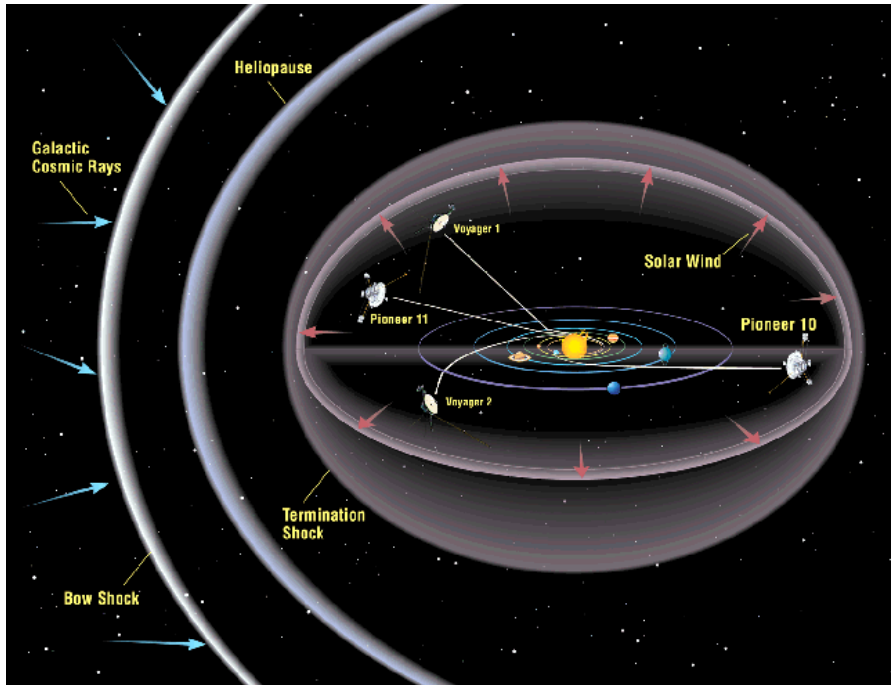


**Figure 2.2: Artist depiction of the Heliosphere showing inbound route of Galactic Cosmic Rays as they encounter the Bow Shock, Heliopause and Termination Shock before entering Earth's Solar System [NASA, 2001].**

Earth receives direct protection from cosmic rays at three different levels. These are the solar wind and heliospheric magnetic field, the geomagnetic field and Earth's atmosphere. The solar wind and heliospheric magnetic field are the first point of contact for GCRs as they enter our solar system. The solar wind and magnetic field create a wave front-like envelope around the planets in our solar system, shown as the Bow Shock in Figure 2.2. At this interface, many cosmic rays are deflected. The geomagnetic field of the Earth has varied influence from the equator to the poles. At the equator, cosmic ray energies must be greater than 17 GeV to pass through the magnetic field while at the poles this value is significantly lower at, effectively, 0.0 GeV. This is known as the geomagnetic cutoff rigidity. In addition to the geomagnetic field, Earth's atmosphere acts to reflect cosmic rays and break them down into secondary components.

Cyclical processes affect the dynamics of the solar-terrestrial system and must be considered to study and understand potential cosmic ray forcing of Earth's climate. The

Sun exhibits 11-year and 22-year sunspot and magnetic reversal cycles. The Sun has a rotational cycle that varies between 25-27 days while Earth goes through a daily rotation. Earth's magnetic field reverses polarity on a scale of 25,000 years. Recent information released from the Thermal Emission Imaging System (THEMIS) satellite mission found that when Earth's magnetic field aligns with that of the Sun, twenty times more particles enter our atmosphere [NASA website, THEMIS, 2008].

Cosmic rays produce the greatest effects on Earth's atmospheric components during times of low solar activity (Figure 2.3). According to the Ulysses satellite mission, a reduction of 20 percent in the average solar wind density and 13 percent in its temperature were recorded since 1990. Comparatively, the solar wind speed has only seen a drop of 3 percent over this time period. Although increasing atmosphere pressure on Earth can cause an exponential decrease in the cosmic ray intensity that is received, the average pressure in the atmosphere is reportedly the lowest now compared to values collected over 50 years of monitoring [Ulysses Mission Report, 2008].

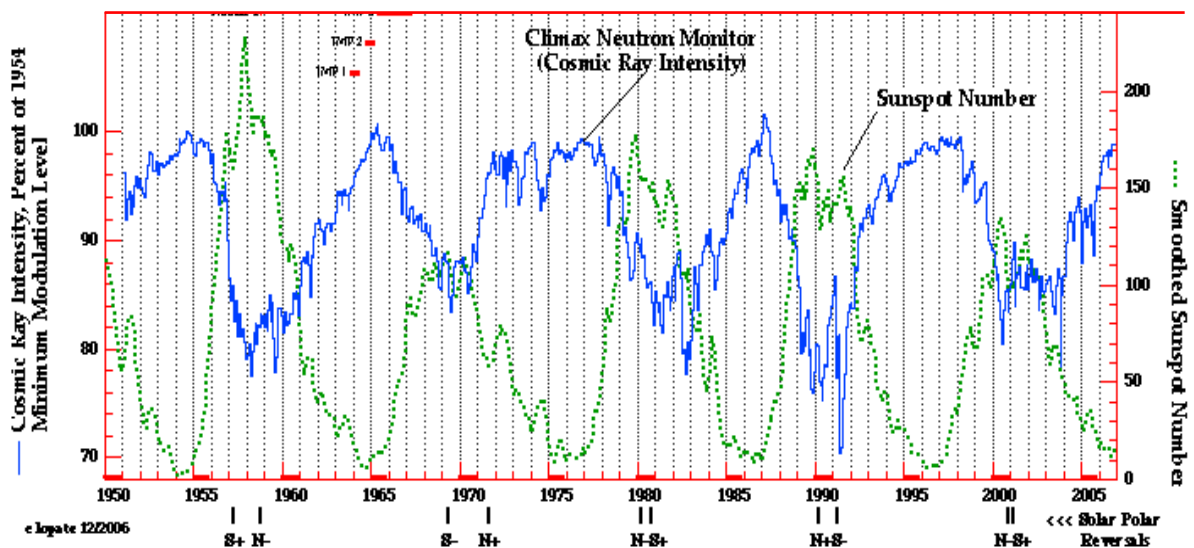


Figure 2.3: Cosmic Ray Intensity as a percentage of 1954 minimum modulation level plotted against Smoothed Sunspot Number to show the inverse relationship [from Ulysses website, University of New Hampshire].

During times of increased cosmic ray flux, atmospheric and cloud microphysical mechanisms exhibit changes. These include changes in the global electric circuit as well as the enhanced production and growth rate of aerosol particulate known as cloud condensation nuclei (CCN) and cloud ice nucleation along with other microphysical processes [Kirkby, 2007].

The Earth's global electric circuit is defined by the ionosphere, with a potential of about 250 kV that is maintained by an upward current of about 1000 A, and Earth's atmosphere which has a finite electrical conductivity. The finite electrical conductivity of the atmosphere below 70 km altitude is controlled by radioactivity from the surface of the Earth, current expulsion from electrified clouds, horizontal ionospheric potential distributions, solar energetic particles (SEPs) and GCRs entering Earth's atmosphere from space. Both SEPs and GCRs enhance the generation of ions [Tinsley et al., 2007]. The return current that controls the movement of ions is in the range of 1-6 pA/m<sup>2</sup> and it is this vertical current density ( $J_z$ ) and the ionospheric potential ( $V_i$ ) that determine the columnar resistance ( $R_C$ ) of the atmosphere as defined in the following relationship:

$$R_C = J_z / V_i \quad (2.3)$$

The current density is controlled by vertical ion and aerosol concentrations and the electrical resistance of the atmospheric column. It varies as a function of geographical location as determined by observational evidence and model generation [Tinsley et al., 2007].  $R_C$  values range between 130 and 300  $\Omega\text{m}^2$  from low to high latitudes due to the controlling force of the geomagnetic field and spatial variation of natural and anthropogenic tropospheric aerosol concentrations [Harrison, 2008]

Accumulation of charge occurs at cloud boundaries, and is defined generally, by a positive charge at the top and negative charge at the bottom of cloud layers (Figure 2.4). "This space charge can become attached to droplets and aerosol particles, and then entrained

within clouds where it may influence microphysical cloud interactions” [Kirkby, 2007]. Basics of cloud formation are not solely dependent on saturation point cooling of the air, but by the presence of aerosols. Aerosols are removed from the atmosphere by different methods, including being scavenged by clouds. Electroscavenging by clouds can occur by two different processes. The first includes collection of space charge by super-cooled (-15°C to 0°C) droplets of aerosol particles that enhance the rate of formation of ice in clouds by contact ice nucleation. This increased ice accumulation augments precipitation which can also impact storm dynamics and atmospheric circulation patterns.

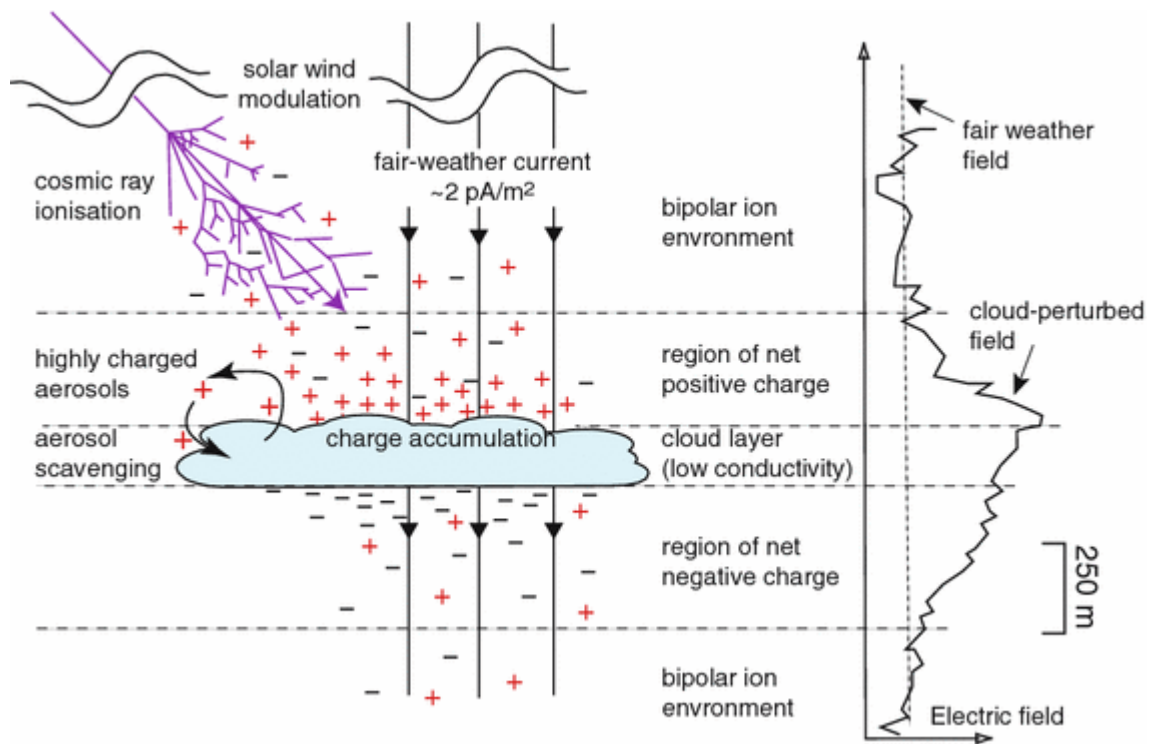


**Figure 2.4: Depiction of how unipolar space charge collects at the top and bottom of clouds due to the drift ions from cosmic rays [from Kirkby, 2007, with permission].**

Secondly, electroscavenging can occur by means of CCN. CCN are in the form of “sea salt, sulphates, mineral dust and aerosols produced from biomass burning” [Haigh et al., 2005]. As few as two molecules can define an aerosol cluster. As further condensation occurs, above a particular critical size, an aerosol cluster has a greater likelihood of growing larger rather than to shrink or evaporate. Highly charged droplets at the cloud boundary both

accelerate early growth and stabilize the cluster through Coulomb forces. In this manner, this process can reduce the critical size necessary for aerosol growth [Kirkby, 2007] (see Figure 2.5). Computations derived from Köhler theory, which describes changes in the saturation ratio with particle radius [Mason, 1971], demonstrate that charging a haze droplet by a factor of 1000 reduces the critical supersaturation by more than 0.5%, as illustrated in Figure 2.6 [Harrison and Ambaum, 2008].

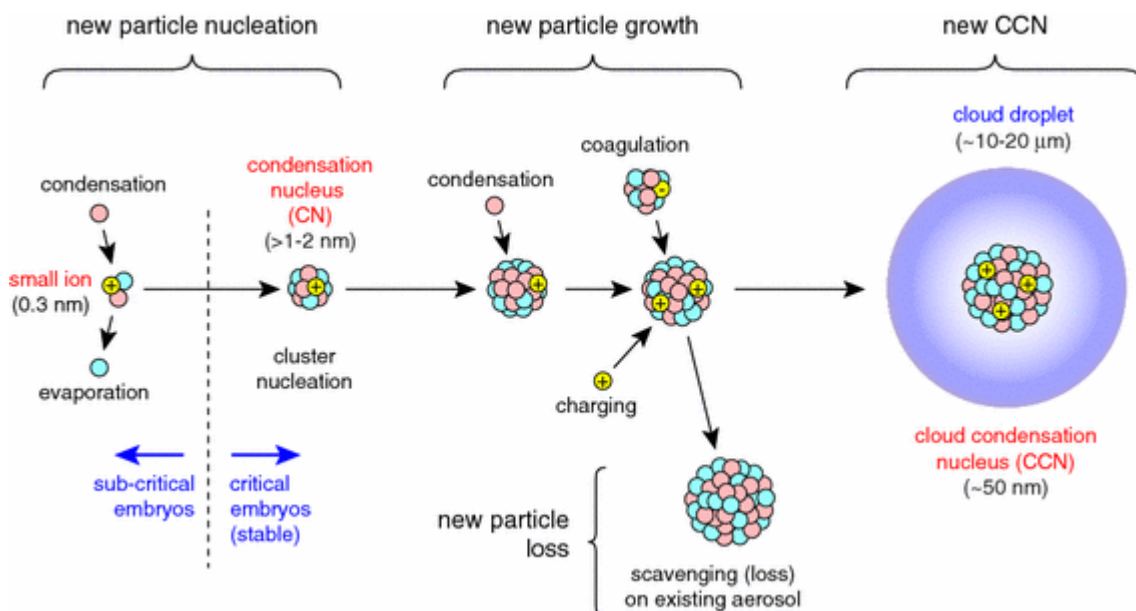


Figure 2.5: “Ion-induced nucleation of new particles from trace condensable vapours and water in the atmosphere” [from Kirkby, 2007, with permission].

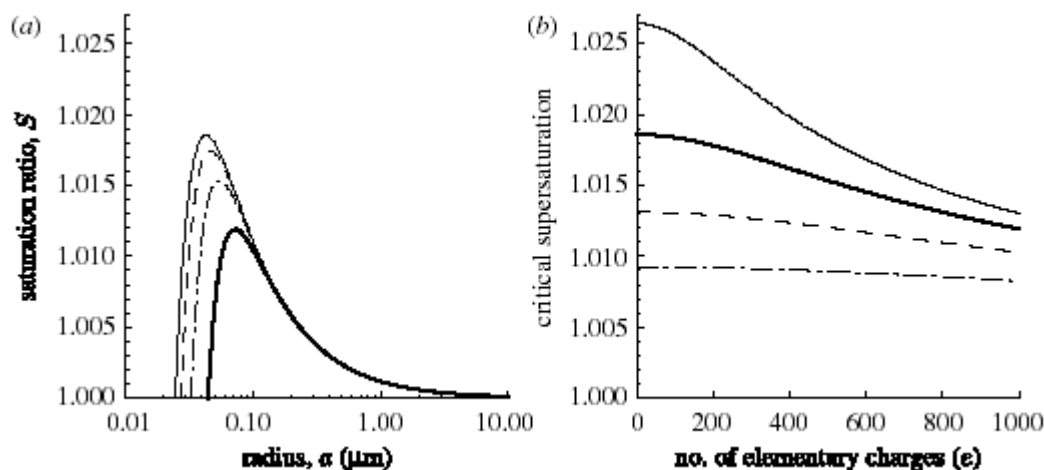


Figure 2.6: Saturation ratio and critical supersaturation plots [Harrison, and Ambaum, 2008, with permission].

From Figure 2.6 (a), the saturation ratio varies with the droplet radius for elementary charges carried by the droplet. The critical supersaturation occurs at the peak of each curve. Assumptions applied to this work include a surface tension value of  $7.5 \times 10^{-2}$  N/m, density at  $1 \times 10^3$  kg/m<sup>3</sup> and a dissolved salt amount of  $5 \times 10^{-21}$  kg. Elementary charges are varied in Figure 2.6 (a) with the thin solid line, dashed line, dot-dashed line and thick solid line equal to 0, 250, 500 and 1000, respectively. Figure 2.6 (b) displays the change in critical supersaturation as it responds to the droplet charge. Here, the amount of dissolved salt is varied, where the thin solid line, thick solid line, dashed line and dot-dashed line represent salt amounts of  $2.5 \times 10^{-21}$  kg,  $5 \times 10^{-21}$  kg,  $1 \times 10^{-20}$  kg and  $2.5 \times 10^{-20}$  kg respectively [Harrison, and Ambaum, 2008].

To further understand the current density that exists at layer cloud boundaries, please see the development of equations shown in Appendix A.

## **2.2 Previous Theoretical and Laboratory Work**

The strongest evidence for the involvement of electrons in chemical reactions occurring on the surfaces of polar stratospheric clouds comes from work over the past 11 years by Qing-Bin Lu, Leon Sanche, Hiroto Tachikawa, Nozomi Nakayama, Ilya Fabrikant, Markus Rex, Neil Harris, Henrik Svensmark and Martin Enghoff and their study groups. This work demonstrated that at 0 eV and slightly larger energies, the processes of vibrational excitation and dissociative electron attachment (DEA) allow electrons to induce or enhance chemical reactions, particularly in the presence of polar states [Fabrikant, 2007]. The electrons at these energies were theorized to mimic the presence of cosmic ray ionization in the atmosphere. The initial study that triggered both additional work and controversy was a laboratory-based experiment by Lu and Madey [1999]. The study results suggested an enhancement of up to two and four orders of magnitude of F<sup>-</sup> and Cl<sup>-</sup> yield, respectively, from electron-stimulated desorption in the presence of both polar molecules and a cooled rare gas or water film. This yield was compared to that of CF<sub>2</sub>Cl<sub>2</sub> co-adsorbed with other non-polar molecules such as CH<sub>4</sub>, where insignificant enhancements were found [Nakayama et al., 2004]. In Lu and Madey's [1999]

experiment, secondary electrons were injected into the water or ammonia layer and were reported to become “self-trapped”. These self-trapped electrons served a vital role in the presence of a  $\text{CF}_2\text{Cl}_2$  molecule on the surface by creating a vibrationally excited intermediate state that dissociated as follows:



where  $e_s$  is the self-trapped electron.

They found that the layer on which the reaction occurred allowed increased ion survival probability [Lu and Madey, 1999]. In later work, they proposed that the resultant  $\text{Cl}^-$  anions were converted to Cl atoms on the cloud surfaces. They asserted that these chemicals were then released in the springtime when the polar atmospheres began to warm, causing a series of atmospheric reactions with the existing stratospheric ozone ( $\text{O}_3$ ) molecules. These reactions were proposed to be responsible for the enhanced depletion of the ozone layer [Lu, 2010a].

Other studies, post-1999, worked to either confirm these data results, using similar or slightly different techniques, or enhance the understanding of the molecular bonds in similar states. The study conducted by Nakayama et al. [2004] used post-irradiation temperature-programmed desorption (TPD) to study “low-energy electron-induced radiolysis of  $\text{CF}_2\text{Cl}_2$ ” [Nakayama et al. 2004]. From this experiment, they identified  $\text{C}_2\text{F}_4$ ,  $\text{C}_2\text{F}_3\text{Cl}$ ,  $\text{C}_2\text{F}_4\text{Cl}_2$ ,  $\text{C}_2\text{F}_2\text{Cl}_2$ ,  $\text{C}_2\text{F}_3\text{Cl}_3$  and  $\text{C}_2\text{F}_2\text{Cl}_4$  as reaction products. They confirmed that C-F bond cleavage resulted, in addition to the already known C-Cl bond cleavage. This C-F bond cleavage was not found in the photolysis case for  $\text{CF}_2\text{Cl}_2$ . They discovered that these new molecular products could play a significant role in atmospheric processes, but stated that the molecules demonstrating the C-F bond cleavage needed to go through rigorous testing using ice surfaces to improve the understanding of their role.

A study by Frieler and Rex et al. [2006] proposed that assumptions around stratospheric bromine levels and speed of photolysis for ClOOCl were underestimated in previous work. The model developed in this work showed that adjustments in these areas better explained the observed January Arctic ozone loss and that bromine plays a more critical role in atmospheric ozone depletion.

Fabrikant [2007]) used a nonlocal complex potential theory model approach to develop a more accurate theory behind the experiments for molecules with non-spherical geometries. He found, through experiment, that the “calculations of DEA to CH<sub>3</sub>Cl and CF<sub>3</sub>Cl molecules on surfaces and in the bulk of Kr films demonstrate that the present theory reproduces the major features observed in experiments: strong enhancements of DEA at the surface and in the medium as compared to the gas phase and the shifting of the peak position towards lower energies” [Fabrikant, 2007].

Tachikawa and Abe [2007] applied the “full dimensional density functional theory molecular dynamics method” to examine the “electron capture of a halocarbon adsorbed on an ice surface” [Tachikawa and Abe, 2007]. Theoretical calculations were conducted that resulted in predictions of significantly elongated C-Cl bonds from the CF<sub>2</sub>Cl<sub>2</sub> molecule after electron capture on a water cluster containing the cyclic water trimer (H<sub>2</sub>O)<sub>3</sub>. This theory deviated from the experimental evidence where one Cl atom interacted with the water cluster while the other existed as a dangling atom until the electron capture. After the electron capture, the dangling Cl atom became the elongated C-Cl bond that was then dissociated from the CF<sub>2</sub>Cl<sub>2</sub><sup>-</sup> (H<sub>2</sub>O)<sub>3</sub> as a “fast” Cl<sup>-</sup> ion. The other C-Cl bond was actually silent during the reaction. In the presence of ice, the translational energy of the CF<sub>2</sub>Cl<sub>2</sub> molecule for this reaction was found to be distributed at the high energy region resulting in a fast Cl<sup>-</sup> ion compared to a resultant slow Cl<sup>-</sup> ion being produced in similar gas phase reactions.

In 2009, Svensmark et al. published a study that examined the effect of changes in cosmic rays on clouds. His team used measurements from the Special Sensor Microwave Imager for cloud water content, and the Moderate Resolution Imaging Spectroradiometer and the International Satellite Cloud Climatology Project for low cloud observations. They determined that approximately seven days after a Forbush cosmic ray minimum, caused by a solar coronal mass ejection, cloud water content and amount of low-lying clouds is reduced. The marked response in cloud water content was noted to be up to seven percent globally.

Although questions may arise around assumptions used in these and similar studies, formation of both a theoretical basis and supporting laboratory evidence resulted. This helped develop the concept of enhanced breakdown of CFCs in nature in the presence of both atmospheric ionization and PSCs. These results established a basis for further research, using measurements of atmospheric properties. To show a relationship between cosmic rays, polar stratospheric clouds (PSCs) and ozone in the Antarctic atmosphere, Lu [2009] produced the following time-series data comparisons (Figures 2.7 and 2.8). These represented percentage variations of cosmic ray intensity compared against both annual mean total ozone values and three-month average zonal mean total ozone, which corresponded to seasonal lows, from 1990 to 2008.

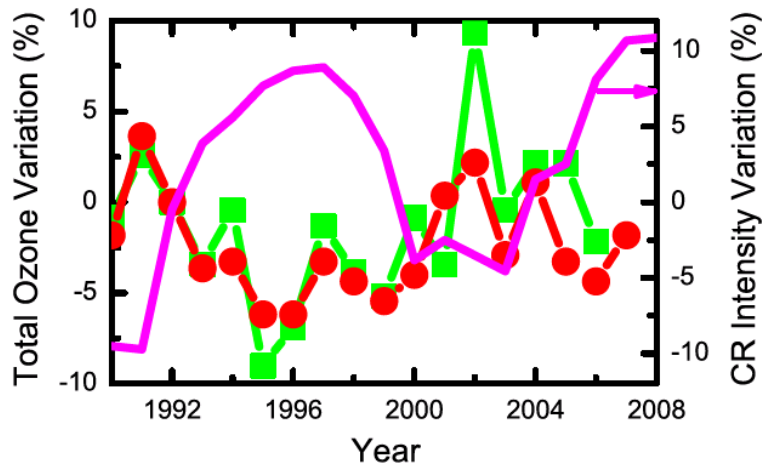


Figure 2.7: Percentage variations of cosmic ray intensity and annual Antarctic mean total ozone data from the two neutron monitor stations [from Lu, 2009, with permission].

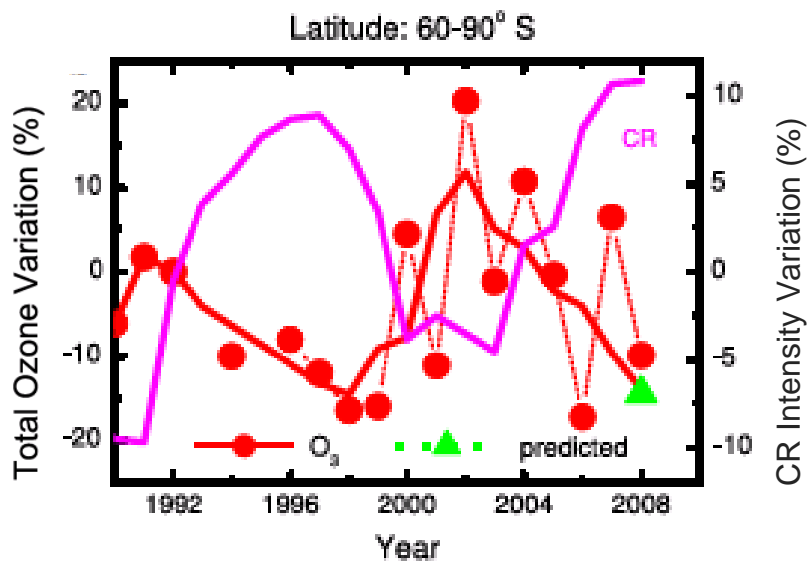


Figure 2.8: Percentage variations of observed Cosmic Ray intensity, averaged from three neutron monitor stations, and monthly average zonal mean total ozone in October in the Antarctic [from Lu, 2009, with permission].

In both of Figures 2.7 and 2.8, the cosmic ray intensity variation is shown in fuchsia. In Figure 2.7, the ozone data is shown in green while in Figure 2.8, it is red. The cosmic ray intensity data for Figures 2.7 and 2.8, was sourced from the Bartol Research Institute (BRI) and represented data averaged from the McMurdo, Thule and Newark neutron monitor

stations. The annual mean total ozone (Figure 2.7) was obtained from the Faraday/Vernadsky and Halley Antarctic ground-based monitoring stations. The ozone data in Figure 2.8 was obtained from NASA satellite missions Nimbus 7, METEOR-3, Earth Probe and OMI (AURA) and represents a latitude band from 60 to 90 degrees south over the period from 1990 to 2008. These observed ozone data are shown relative to the value for 1992, multiplied by a factor of 75 percent and are depicted as solid circles. To prepare the time-series data for comparison, Lu and teams applied a 3-point averaging smoother (red solid line in both figures) and the green triangle in Figure 2.8 represented a predicted zonal mean total O<sub>3</sub> value from their work [Lu, 2009]. Although the correlation coefficient between the datasets was not documented, visually, the cosmic ray data contrasted the ozone data where highs in the cosmic ray intensity were concurrent with lows in the ozone values. His cross plot of cosmic ray intensity versus total ozone variation did demonstrate that a linear dependency existed between the datasets [Lu, 2009].

Lu determined through this work that from 1990 to 2010, the total polar ozone demonstrated 11-year cyclic variations. These ozone variations were found to oscillate along with solar cycle and cosmic ray events [Lu, 2010a]. He also found that cooler temperatures observed in the lower stratosphere correlated very strongly to total ozone from the Halley station data in the Antarctic and that “neither the solar cycle effect nor the pure CR effect is responsible for the present observation of 11-year stratospheric cooling” [Lu, 2010a]. Lu suggested that this stratospheric cooling would cause enhanced PSC formation in the following year that would further affect ozone levels. Through modeling efforts, Lu’s [2009] study claimed that cosmic ray activity would continue to increase over the 11-year cycle and predicted extreme ozone depletion in 2009 as a result. He proposed that the recovery of the Antarctic ozone hole was going to be slow but steady to year 2065 with a dependency on equivalent effective stratospheric chlorine measurements. Lu stressed that the “direct CR-cloud (PSC) correlation remains a subject of significant controversy” [Lu, 2010a].

Harris and his team [2010] examined ozone loss as it relates to meteorological polar stratospheric cloud column measurements and volume of PSCs. They simulated ozone losses and PSCs between 14 and 24 km altitude in a laboratory setting utilizing the Alfred Wegener Institute photochemical box model. Their focus was the edge of the Arctic polar vortex at about 10 degrees from the North pole at 80° north latitude. The extent of the original activation took precedence over the factor of timing of the photolysis of nitric acid. The photolysis of inorganic chlorine as



was determined to be the rate-limiting step and allowed for the deduction that both the extensive nature and persistence of PSCs play a critical role in predicting ozone loss. Harris [2010] also noted that photolysis rates substantially rise as a function of decreased zenith angle from winter to spring and stated that "more chlorine is activated for a given PSC exposure at higher altitudes".

The clear relationship found between the volume of polar stratospheric clouds and seasonal ozone loss gathered from ozonesonde data as shown in the following figure (Figure 2.9).

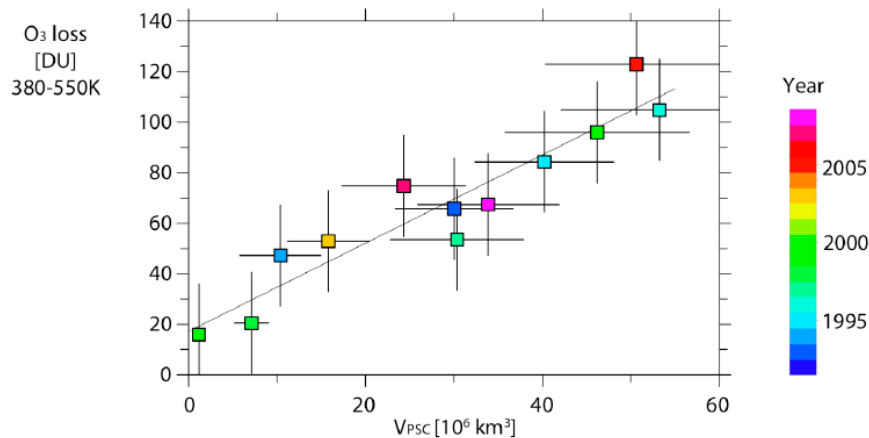


**Figure 2.9: Integrated ozone loss as a function of polar stratospheric cloud volume [from Harris et al., 2010, with permission].**

Data from the "winters of 2000/01, 2001/02, 2003/04, 2005/06 and 2008/09 were not included in Figure 2.9 due to major warmings and/or lack of ozonesonde data" [Harris et al., 2010].

Enghoff et al. [2011] demonstrated the "first unambiguous observation of the ion-effect on aerosol nucleation using a particle beam under conditions that resemble the Earth's atmosphere" [Enghoff et al., 2011]. This confident statement was warranted on the basis of a study pioneering the use of a new facility, the Conseil Européen pour la Recherche Nucléaire (CERN) Proton Synchrotron. This facility allowed the experimenters to mimic the constituents of the atmosphere while administering their tests using a low-intensity ionization source (580 MeV electrons), under stable and controlled conditions. This low-intensity ionization was in the range of the predicted cosmic ray effect in Earth's atmosphere. In this experiment, humidified air, sulfur dioxide and ozone were in perpetual motion. Sulfuric acid was introduced to the chamber using UV lamps both at the beginning of and at different intervals throughout the experiment. Only the strength of ionization was altered to determine any effect this would have on aerosol formation. The aerosol concentrations were detected by a condensation particle counter and the

results showed a positive increase in these concentrations with introduction of heightened ion density (see Figure 2.7).

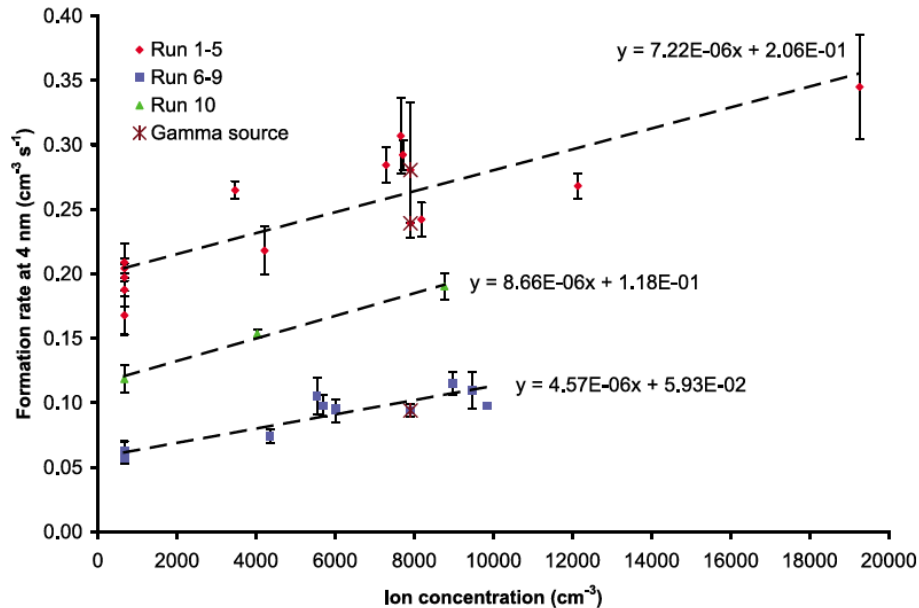


**Figure 2.10: Plot of ion concentration in the atmospheric pressure reaction chamber versus the formation rate of aerosols at 4 nm, as measured by the condensation particle counter at CERN. Error bars represent the statistical measurement uncertainties [Enghoff et al., 2011, with permission].**

A study by Snow-Kropla et al. [2011] examined the relationships between cosmic ray counts and cloud and aerosol properties. They used a global chemical transport model with aerosol microphysics to determine if CCN concentrations were influenced by cosmic ray flux or intensity. They incorporated the parameters of “primary emissions, Secondary Organic Aerosol condensation and charge-enhanced condensational growth” [Snow-Kropla et al., 2011] in their work to examine any dependencies. They found that reduced primary emissions led to improved response of CCN to cosmic ray activity. In contrast, the Secondary Organic Aerosols and charge enhanced condensation caused only local dependencies. Overall, the difference between the tests representing the highest and lowest cosmic ray flux cycles was globally only 0.2 percent for CCN larger than 80 nm and up to 1 percent difference in production of particle sizes greater than 10 nm. The column-integrated aerosol Angström exponent that they tested did not show responses to

alterations in cosmic ray intensity and they were not able to reproduce the numeric findings made by Henrik Svensmark in a 2009 report. They concluded that the effect of cosmic rays on CCN and the Angström exponent are lessened due to the nature of the cloud microphysical system and that the tested input parameters were inconclusive in establishing a clear dependence.

### CHAPTER 3: DATABASES

The data used in this research were extracted from a variety of sources. This chapter will describe each data source including available background information used in development of the final data product.

The region used for this thesis, which served as the basis for data retrievals, included an area centered on the Thule, Greenland neutron monitor station with coordinates of 76.5396N latitude and 68.7759W longitude. Satellite data included extents outward from this location to 150 km in each direction detailed in Figure 3.1.

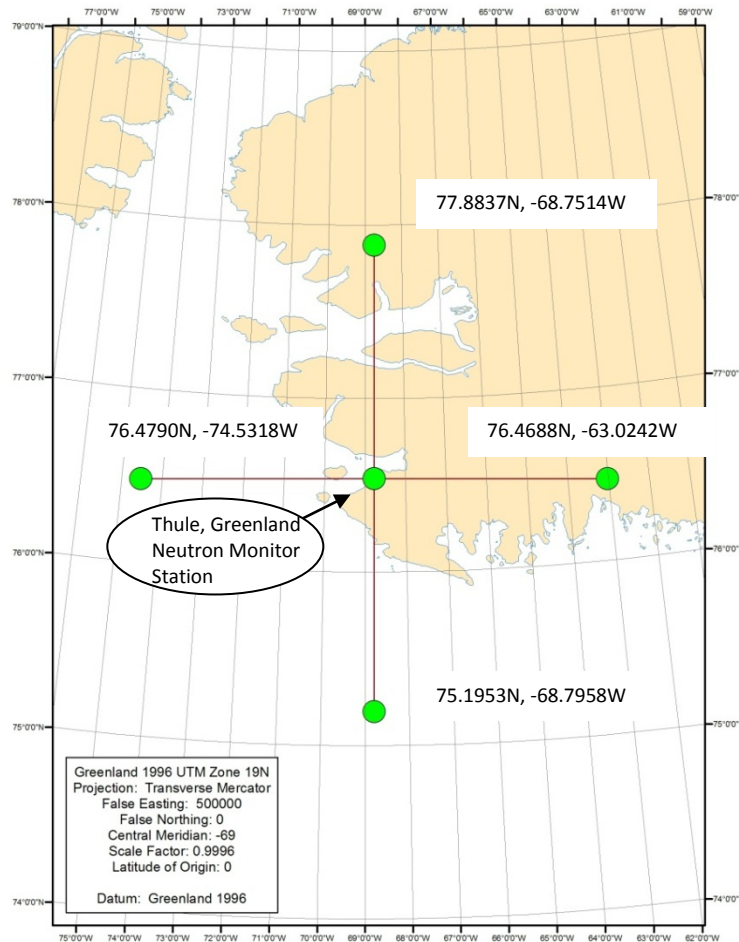


**Figure 3.1: Satellite retrieval co-ordinate space, centered on the Thule, Greenland station.**

Deviations from this region included 27 OMI data points that extended past 150 km up to 162.4 km and additional SBUV ozone data retrievals that included an area 200 km from the Thule, Greenland station, depicted in Figure 3.1.

Both satellite and ground-based data sources were used for this study (Figure 3.2). Ozone and cloud data were obtained from polar-orbiting satellite missions. The cosmic ray data was sourced from the Thule, Greenland Neutron monitor station and served as ground-based atmospheric ionization data.

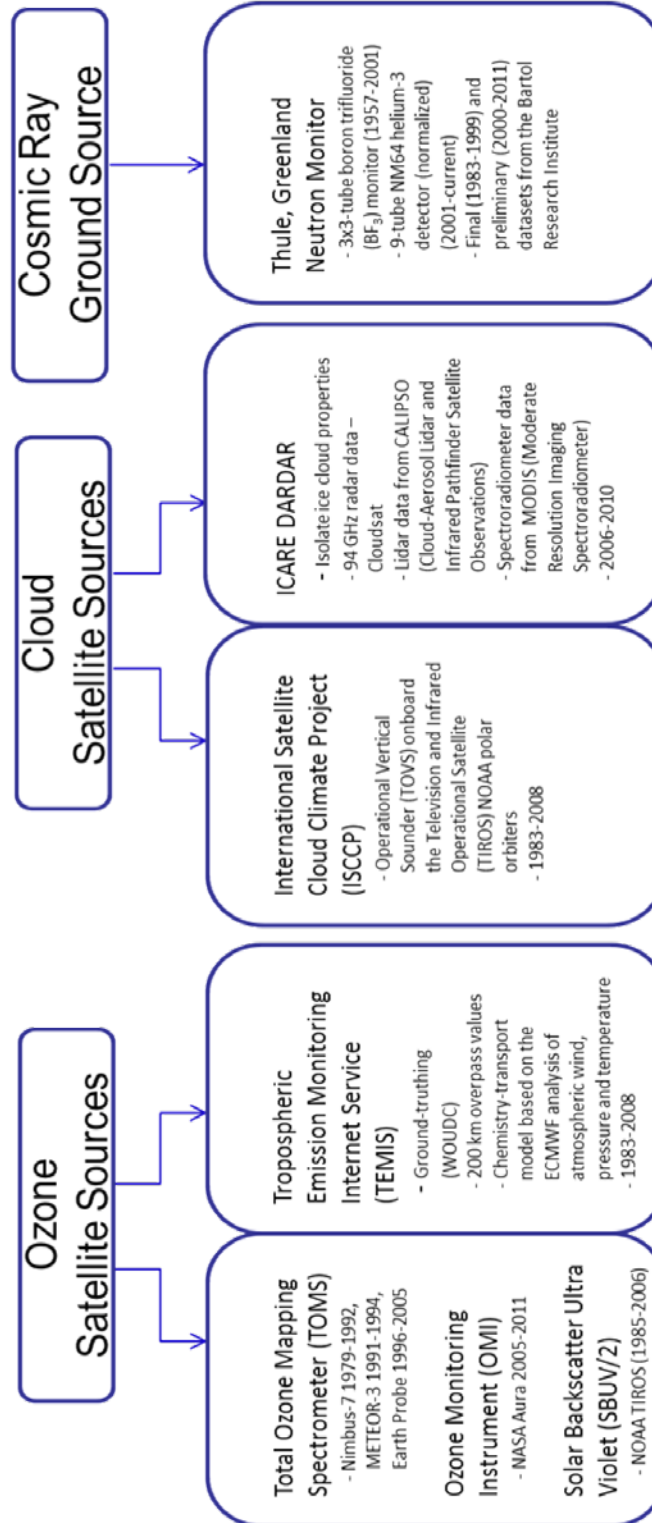


Figure 3.2: Summary of ozone, cloud and cosmic ray data sources.

### **3.1 Ozone Data Descriptions**

The first set of ozone data chosen for this study included the direct detection of total column ozone from several NASA missions from 1983 to 2011. These will be referred to as the satellite ozone data in this paper. The second source of ozone used in this study included a collaboration of ozone measurements from all available Earth-orbiting satellites over a 30-year period, with the final product available from TEMIS (1979-2008).

#### **3.1.1 Satellite Ozone Data**

The remote sensing Backscatter Ultraviolet (BUV) Technique and instrumentation are used to obtain readings of atmospheric ozone. Radiance is defined and quantified when measurements of inbound solar irradiance are compared to atmospheric backscatter. Incident solar radiation that penetrates the atmosphere of the earth goes through stages of absorption and scattering once it comes in contact with atmospheric molecules. The absorption of short wavelength radiation in the upper atmosphere occurs in the presence of ozone while Rayleigh scattering is attributed to collisions with cloud molecules, aerosols, and the Earth's surface [Corprew, 1997].

Due to its nature, atmospheric ozone influences the amount of absorption and attenuation of radiance in both the incoming and outgoing directions. Backscatter radiance is monitored by satellite and these collected values are analyzed in terms of specific wavelengths that are both strongly and weakly absorbed by ozone molecules in the atmosphere. Differences between the strong and weak pairs of irradiance (solar-incident radiation) and radiance (Earth radiation) profiles provide an estimate of ozone incidence in the atmosphere at particular satellite viewing angles.

Several considerations take place in order to compute the amount of atmospheric ozone. These include the incident angle of solar flux, satellite viewing angle, existence of atmospheric clouds and aerosols, tropospheric pressures, and reflective nature of the Earth [Corprew, 1997].

Processing of the satellite retrievals relies on definition of these contributing variables and treatment of the data. Solar backscatter radiation retrieved by satellite instrumentation is defined by (the following series of equations is from the Corprew [1997], based on the Total Ozone Mapping Spectrometer (TOMS) satellite data description):

$$I(i) = I_a(i) + I_g(i) \quad (3.1)$$

where  $I(i)$  indicates the backscatter radiance at a particular wavelength,  $i$ ,  $I_a(i)$  is the atmospheric component of radiance at wavelength,  $i$ , and  $I_g(i)$  describes the various contributions of surface reflectance at this same wavelength.

The influence from the Earth's surface is set as:

$$I_g(i) = \frac{R * T(i)}{(1 - R * S(i))} \quad (3.2)$$

where  $R$  is the Lambertian reflectivity of the lower boundary,  $T(i)$  describes the signal retrieved from both the direct plus the diffuse radiation reaching the surface and diffusely reflecting back to the satellite, and  $S(i)$  is the portion of radiation that goes through multiple reflections between the Earth and atmosphere before being transmitted away from the Earth to be detected by the satellite, where

$$\frac{1}{(1 - R * S)} \quad (3.3)$$

accounts for these types of reflections. In these equations, certain dependencies exist and they are outlined in Table 3.1.

**Table 3.1: Description of dependencies for radiance satellite retrievals in determining atmospheric ozone profiles. [Corprew, 1997]**

Variable	Dependencies:
<b>Backscatter Radiance <math>I(i)</math></b>	<b>Total ozone amount</b>
<b>Surface Reflectance Contributions <math>Ig(i)</math></b>	<b>Effective scene pressure</b>
	<b>Solar zenith angle</b>
	<b>Satellite viewing angle</b>
<b>Atmospheric Radiance Component <math>Ia(i)</math></b>	<b>All variables in equations 3.1 through 3.3, except <math>R</math></b>
<b>Direct and Scattered Surface Retrievals <math>T(i)</math></b>	
<b>Backscatter Radiance <math>I(i)</math></b>	<b>Shape of ozone profile (partial dependence)</b>
<b>Atmospheric Radiance Component <math>Ia(i)</math></b>	

The Total Ozone Mapping Spectrometer (TOMS) instrument collections from the Nimbus 7 (1979-1992), METEOR-3 (1991-1994) and Earth Probe (1996-2005) satellite missions along with data from the Ozone Monitoring Instrument (OMI) on board the NASA Aura (July 2004-2007) satellite were obtained from NASA [McPeters, 2011].

The Nimbus 7 satellite mission used BUUV profiling instruments that scanned at a series of nadir angles through a 200 km square field of view. The METEOR-3 TOMS used a nadir angle scanner over a 60 square km instantaneous field of view (IFOV). Both of these missions retrieved global coverage data signals of wavelengths in the range of 312 to 340 nm and produced results in the form of total column ozone measurements. These values of total ozone were computed using radiance ratios, known as Pair values, as previously described.

Following wavelength drift and instrument optics and sensitivity corrections to the retrievals, an N-value is computed onboard the satellite as:

$$N(i) = -100 \log \left[ \frac{I(i)}{F(i)} \right] \quad (3.4)$$

where “the ratio  $I/F$  is the backscatter radiance  $I(i)$  normalized by the direct solar radiation,  $F(i)$ , incident at the level of the sensor” [Corprew, 1997].

To determine total column ozone response, long wavelength and short wavelength retrievals are paired as these ratios of  $I/F$ . For TOMS, these computations are:

$$A - Pair = N(313nm) - N(331 nm) \quad (3.5)$$

$$B' - Pair = N(318nm) - N(340 nm) \quad (3.6)$$

$$C - Pair = N(331nm) - N(340 nm) \quad (3.7)$$

“For large ozone amounts at low sun angles, the  $A - Pair$  becomes less sensitive to changes in total ozone since 313 nm senses higher in the atmosphere” and is “more sensitive to [the] ozone profile shape” [Corprew, 1997].

Computations use TOMS longest wavelength retrievals of 360 nm and 380 nm to evaluate the surface reflectivity as:

$$R = \frac{(I-Ia)}{(T-S*(I-Ia))} \quad (3.8)$$

where  $Ia$ ,  $S$  and  $T$  are taken from known table values, based on satellite positioning and incoming solar radiance angles.

Scene pressure ( $Ps$ ) is determined as:

$$P_s = (1 - w) * P_c + w * P_t \quad (3.9)$$

where  $w$  is a weighting function that accounts for the presence of surface snow or ice in the scene and the conditions of surface reflectivity at 1000 mb,  $P_c$  is the cloud top pressure and  $P_t$  is the terrain pressure (both in units of mb).

Linear interpolations are computed for both ozone Pair values and scene pressures by using values from two adjacent latitudes. Linear interpolation is then calculated for pressures between the values of 400 and 1000 mb. The final ozone value in DUs for each IFOV is defined as the weighted average of the total ozone as computed from the three pairs of ratios. An example of monthly images of total ozone values, in DU, available from the BUV and TOMS satellite instrumentation, is provided in Figure 3.3.

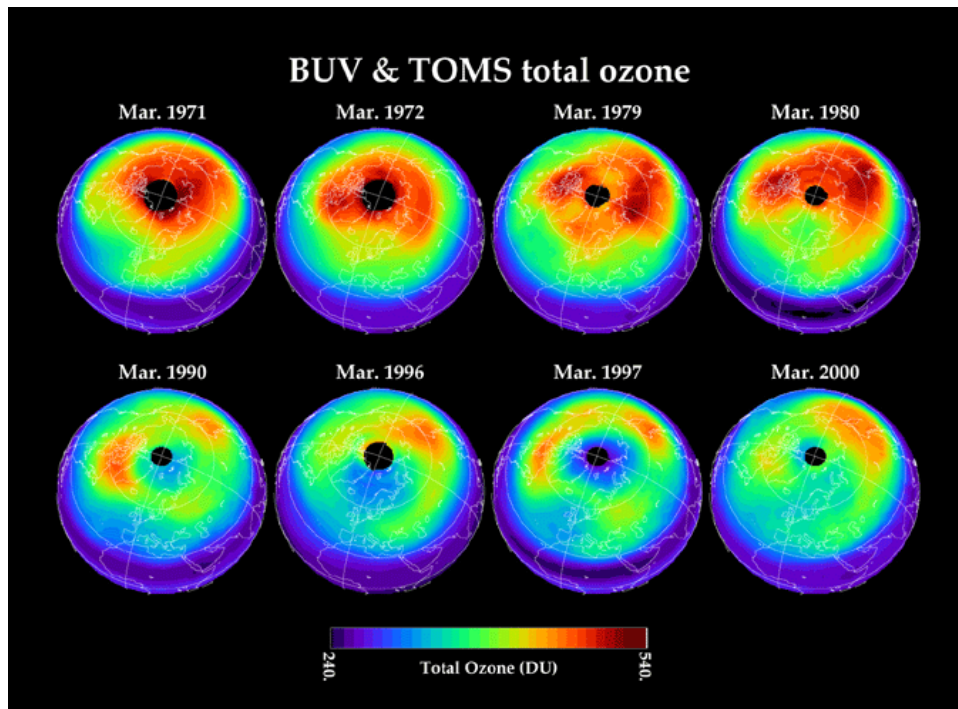


**Figure 3.3:** Depiction of time-lapse changes in total ozone over the Arctic showing BUV and TOMS satellite readings from March 1971 to March 2000 [from Newman, 2000].

The Ozone Monitoring Instrument (OMI) was developed by the Netherlands Agency for Aerospace Programmes (NIVR) working in conjunction with the Finnish Meteorological Institute (FMI). This instrument contains calibration systems and detects signal wavelengths over the visible range of 349-504 nm and the ultraviolet (UV) range of 264-380 nm, where the UV channel is split (UV-1 264-311nm and UV2 307-383 nm). It has a wide-field reflective telecentric telescope that inputs data to two separate imaging spectrometers with charge-coupled device (CCD) detectors having 0.4 second exposure times. The CCD detectors utilize 22.5 x 22.5 micron pixels, each continuously spaced so that air-borne molecule and aerosol detection is optimized [OMI, 2008]. OMI has a ground spatial resolution of 13 by 25 km. Different optical paths separate the incoming solar radiation (irradiance) from the Earth radiation (radiance) and allow for calculation of the atmospheric constituents of ozone, NO<sub>2</sub>, SO<sub>2</sub> and other aerosols by using incoming irradiance-radiance ratios similar to the BUUV technique [Douglass, NASA GSFC]. An example of springtime OMI instrument retrievals of total ozone is shown in Figure 3.4. This image illustrates dramatic changes in Arctic ozone, with the lowest modern recorded values being in March 2011. These low values are linked with cooler stratospheric temperatures and the persistence of high levels of chlorine.

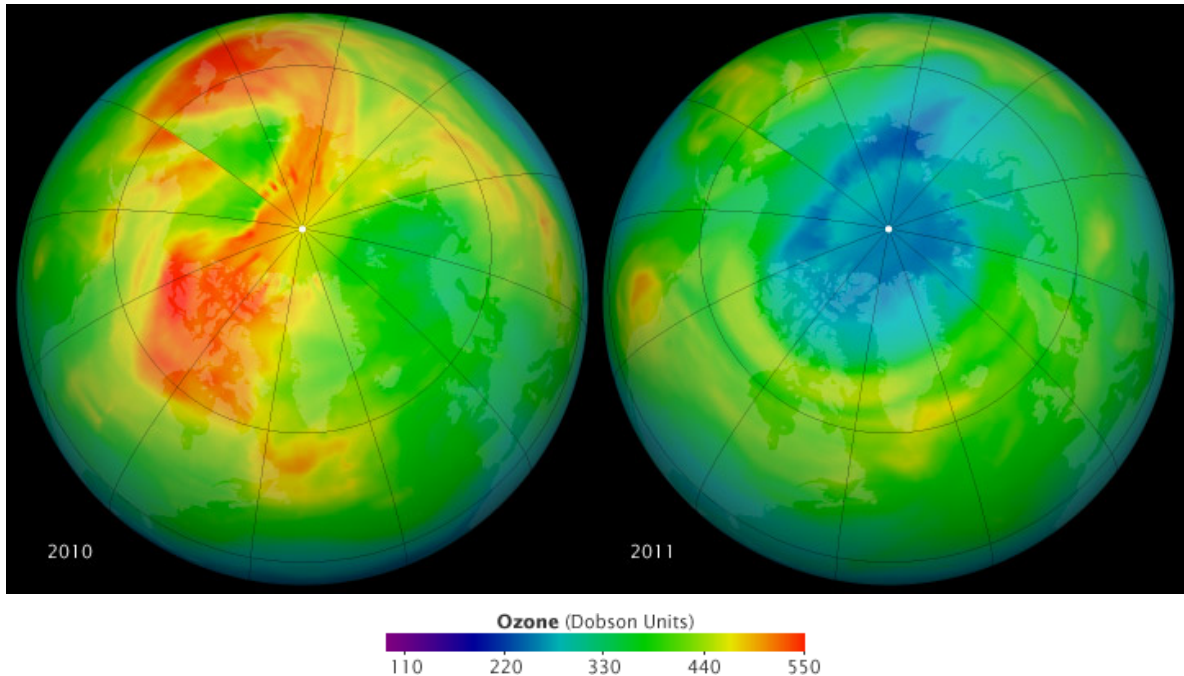


**Figure 3.4: Depiction of year-to-year changes in daily average total ozone (DU), over the Arctic, from OMI satellite retrievals on March 19, 2010 and 2011 [from Remer, 2011].**

#### **3.1.1.1 Documented Errors in Ozone Satellite Data Retrievals**

The main disadvantage of using the BUV technique is that the effects of increased multiple scattering and reduced sensitivity to the shape of the profile lead to poor vertical resolution in the region below the ozone peak (about 25 km).

From a technical standpoint, degradation of optical paths could occur over time due to incoming protons damaging the CCD detector pixels, producing dark currents and Random Telegraph Signal (RTS) responses. In-flight calibration identifies the RTSs as bad pixels and background signals are updated daily to reduce the effect of dark currents and reduce any long-term bias in the irradiance-radiance ratio. Signal-to-noise ratio is controlled by co-adding 5 sequential CCD exposures. The use of two different channels in the UV spectrum allows for the identification and elimination of redundant stray light entering the detector [OMI, 2008].

### 3.1.2 TEMIS Ozone Data

The Tropospheric Emission Monitoring Internet Service (TEMIS) provided an additional source of ozone data. It included results from a significant project that was founded for the purpose of creating a complete database of global ozone measurements from all available Earth-orbiting satellites over a 30-year period. The TEMIS project attempted to account for discrepancies between monitoring instruments and measurements, that were found to be difficulties in similar projects, by applying corrections for solar zenith angle, viewing angle, time (trend), and effective ozone temperature. Inputs included measurements from the monitoring instruments of TOMS, SBUV, Global Ozone Monitoring Experiment (GOME), SCanning Imaging Absorption SpectroMeter for Atmospheric CHartographY (SCIAMACHY), OMI and GOME-2, totaling 14 satellite datasets (see Table 3.2).

**Table 3.2. Input satellite retrieval datasets used in the Multi-Sensor Reanalysis of Total Ozone Project [from Van der A et al., 2010].**

Name	Instrument	Satellite	From	To	Dist.	#WSI	Overpasses
TOMS2a	TOMS	Nimbus-7	1 Nov 1978	6 May 1993	0.75°	137	182 464
TOMS2b	TOMS	Earth probe	25 Jul 1996	31 Dec 2002	0.75°	146	129 839
SBUV07	SBUV	Nimbus-7	31 Oct 1978	21 Jun 1990	2.00°	112	24 345
SBUV9a	SBUV/2	NOAA-9	2 Feb 1985	31 Dec 1989	2.00°	099	11 705
SBUV9d	SBUV/2	NOAA-9	1 Jan 1992	19 Feb 1998	2.00°	135	22 706
SBUV11	SBUV/2	NOAA-11	1 Dec 1988	31 Mar 1995	2.00°	166	38 874
			15 Jul 1997	27 Mar 2001			
SBUV16	SBUV/2	NOAA-16	3 Oct 2000	31 Dec 2003	2.00°	131	16 384
GDP	GOME-1	ERS-2	27 Jun 1995	31 Dec 2008	1.80°	156	108 758
TOGOMI	GOME-1	ERS-2	1 Apr 1996	31 Dec 2008	1.80°	155	107 276
SGP	SCIAMACHY	Envisat	2 Aug 2002	31 Dec 2008	0.90°	139	50 017
TOSOMI	SCIAMACHY	Envisat	2 Aug 2002	31 Dec 2008	0.90°	139	47 532
OMDOAO3	OMI	Aura	1 Oct 2004	31 Dec 2008	0.90°	123	84 089
OMTO3	OMI	Aura	17 Aug 2004	31 Dec 2008	0.90°	125	83 405
GOME2	GOME-2	Metop-A	4 Jan 2007	31 Dec 2008	0.45°	105	28 538

World Ozone and Ultraviolet Data Center (WOUDC) ground-based daily measurement averages were used during the TEMIS project to make corrections on all input datasets and for “ground-truthing” purposes. Overpass values, within 200 km, were compared to global ground-based station values to remove trends and to correct for systematic biases.

The total assimilation portion of the project used all ground-based station data, derived from the WOUDC database, as the theoretical “true” data for satellite comparison and

modeling purposes. Effective ozone temperatures were generated from the European Centre for Medium-Range Weather Forecasts (ECMWF) temperature profiles and the Fortuin and Kelder [1998] ozone climatology database which detailed seasonal dependent values [Van der A et al., 2010]. The correction applied to the Dobson total ozone data, which accounted for effective ozone temperature and attempted to reduce the effects of drift and offset, was as follows:

$$X_{corr} = X_{dobson}(1 - 0.0013 * (T_{eff} + 46.3)) \quad (3.10)$$

where  $X_{corr}$  is the corrected ozone value in DU,  $X_{dobson}$  is the original total ozone value from the ground-based dataset in DU, and  $T_{eff}$  is the effective ozone temperature, in degree Celsius, that is “defined as the integral over altitude of the ozone profile-weighted temperature” [Van der A et al., 2010].

A Tracer transport Model 3 ozone Data Assimilation Model (TM3DAM) software was used to generate the TEMIS product. It incorporated a chemistry-transport model based on the ECMWF analysis of atmospheric wind, pressure and temperature. Sixty layer definitions were used to describe the upper troposphere and stratosphere with a 2 by 3 degree latitudinal and longitudinal horizontal resolution. With additional detail provided by ten ozone tracers per grid cell, the output resolution was 1 by 1.5 degrees. Kalman filtering was used in the model “In this approach the forecast error covariance matrix is written as a product of a time independent correlation matrix and a time dependent diagonal variance”. [Van der A et al., 2010]. Using this technique, observed minus forecast evaluations were performed, and RMS values were computed.

### **3.1.2.1 Documented Sources of Error in TEMIS Data Assimilation Technique**

Improbable ozone values (outside of the range 50 to 700 DU) and those greater than three times the observational or model uncertainty, were removed from the TEMIS database. Three main sources of errors were identified during the development of the TEMIS product. The first was defined as instrument or measurement error. This type of error

corresponded to each of the model inputs such as Solar Zenith Angle and Viewing Zenith Angle measurement error, observation error and noise. The other error sources were a result of the modeling process and expressed as representation error, generated while comparing the satellite to ground-based data, and forecast error [Van der A et al., 2010].

Corrections to satellite datasets were considered in the cases of non-linear dependence of values on the solar zenith angle (SZA), viewing zenith angle (VZA) and effective ozone temperature ( $T_{\text{eff}}$ ) along with unrealistic trends in the data. These corrections were applied from the pixel level to the full satellite dataset. A summary of applied corrections are provided in Table 3.3. Seasonal and latitude dependence, were handled with the use of ozone predictors in the model [Van der A et al., 2010].

**Table 3.3: Assimilation process corrections applied to satellite datasets used in the Multi-Sensor Reanalysis of Total Ozone project [from Van der A et al., 2010].**

Name	RMS3 (DU)	Trend (y/n)	VZA (y/n)	SZA (y/n)	$T_{\text{eff}}$ (DU/C°)	RMS4 (DU)
TOMS2a	10.16	no	no	no	-0.462	9.98
TOMS2b	9.84	partial	pixel	no	-0.447	9.33
SBUV07	11.12	no	no	no	-0.153	11.09
SBUV9a	11.87	no	no	no	-0.376	11.81
SBUV9d	10.66	no	no	no	-0.196	10.63
SBUV11	10.65	no	no	no	-0.258	10.60
SBUV16	10.43	no	no	no	-0.467	10.22
GDP	9.60	no	pixel	yes	no	9.39
TOGOMI	8.95	no	pixel	no	no	8.84
SGP	9.99	yes	yes	no	no	9.80
TOSOMI	9.80	yes	yes	yes	no	8.98
OMDOAO3	9.41	yes	no	nonlin	+0.300	9.01
OMTO3	7.60	no	no	no	-0.282	7.45
GOME2	8.30	yes	pixel	yes	no	7.71

From these results, the OMT03 dataset was expressed as the one that correlated most closely to the ground-based data.

After these corrections, final assimilation model errors were expressed as RMS errors which were on the order of 2 percent. “For high solar zenith angles the RMS value increases, because these measurements are usually associated with the highly variable

ozone concentrations in and around the polar vortex. In addition, the model bias is higher closer to the region of the polar night, where no satellite observations of ozone are performed” (Van der A et al., 2010). Differences between the ground- and satellite-based data for the Multi-Sensor Reanalysis (MSR) full modeling time frame are shown in Figure 3.5.

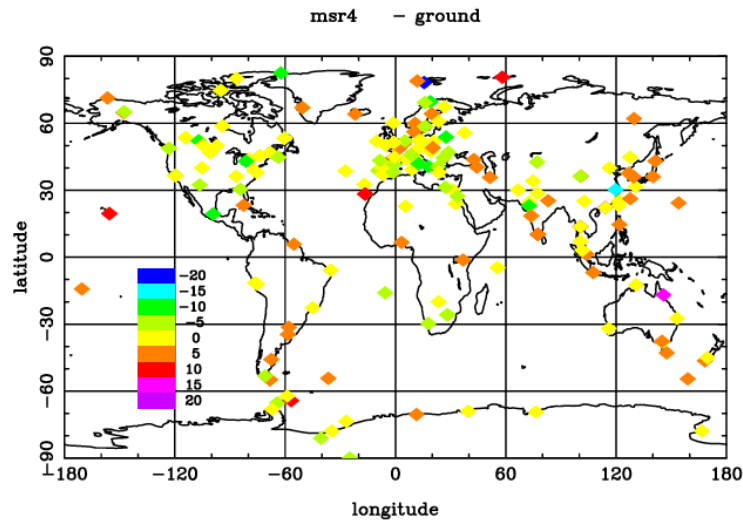


**Figure 3.5:** “Fitted offset (MSR-ground) between the MSR level 4 assimilation data and all selected ground measurements for the period 1978-2008” [from Van der A et al., 2010, with permission].

The total ozone difference or offset associated with the Thule, Greenland station is on the order of -10 DU.

### 3.2 ISCCP and DARDAR Cloud Data Descriptions

Several satellite sources, with many being used for meteorological studies and monitoring purposes, have existed for the detection of clouds and atmospheric conditions in the Arctic atmosphere. Many of these are known as polar orbiters since they encircle the globe and their orbits cross at the north and south poles. Each of these polar orbiting satellites have specific project timelines with various types of equipment on-board. Improvements in detection equipment were added for successive satellite missions. These efforts have contributed to the significant database that is now available for atmospheric and cloud studies, but challenges exist in merging this data into a contiguous database.

### **3.2.1 ISCCP Cloud Data**

In 1983, the International Satellite Cloud Climatology Project (ISCCP) was launched. ISCCP is part of the World Climate Research Program (WCRP) and offered a unique look at global weather systems and the determination of cloud properties from several completed satellite missions. The data collection included a global database of normalized infrared (IR) and visible (VIS) radiance data. The first available data was from July 1, 1983 and the project continued until June 30, 2008. The ISCCP project included several research centers where data products were optimized and set against models to develop an understanding of cloud properties from cloud droplet sizes through to differentiation of cloud layers and three dimensional models of cloud distribution [Kusterer, 2010]. A flowchart showing the ISCCP Cloud Analysis Procedure is shown in Figure 3.6. Key considerations were calibration and navigation of the instruments along with data gathering and manipulation techniques developed for the project. The visual and infrared radiance data was a contribution from all available weather satellites with approximate 30 km spatial resolutions at 3 hour time intervals.

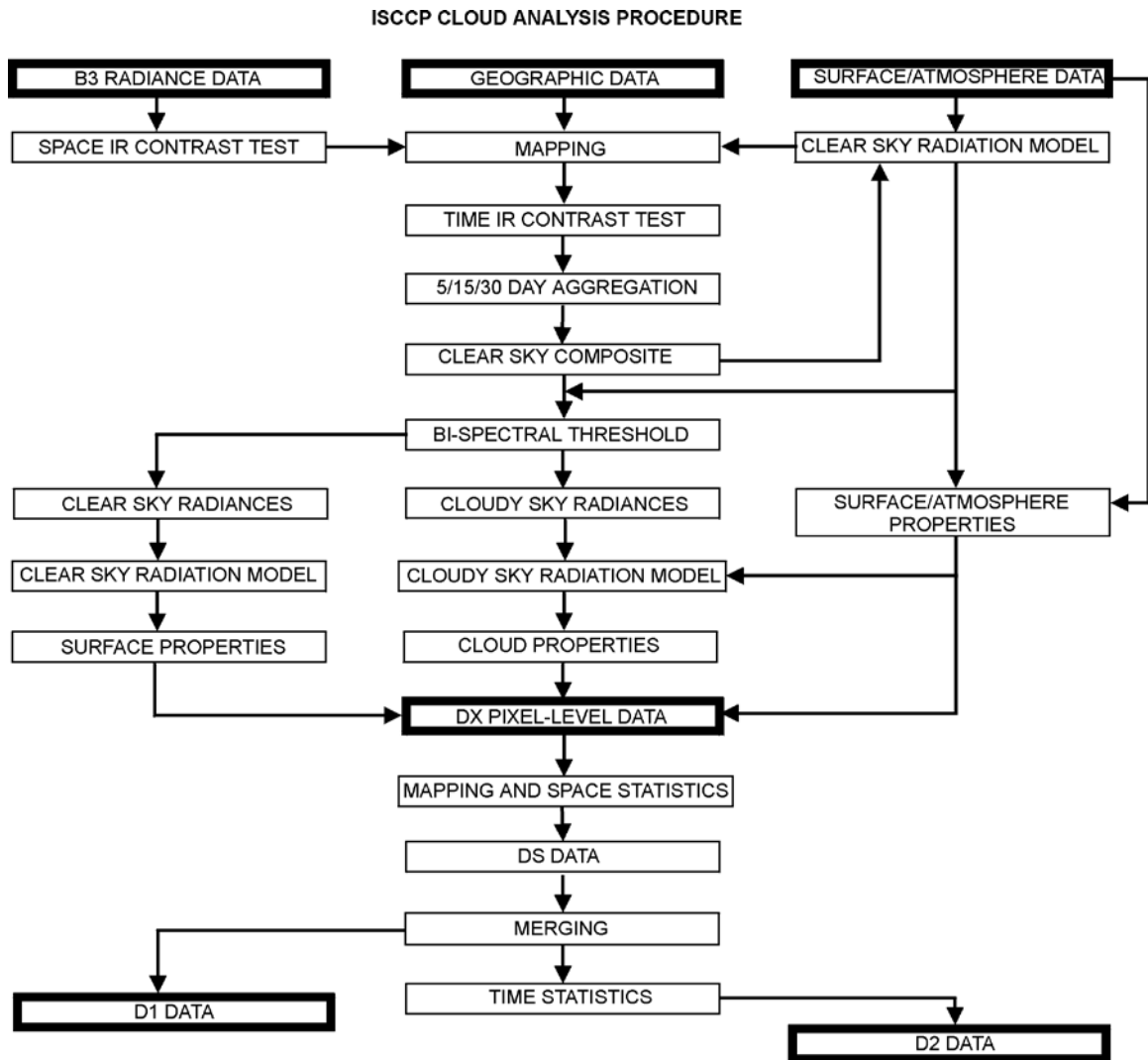


**Figure 3.6: ISCCP Cloud Analysis Procedure illustrating how data retrievals are handled in the process to output D1 and D2 data types [from Rossow et al., 1996, with permission].**

The ISCCP datasets include data capture from the Operational Vertical Sounder (TOVS) onboard the Television and Infrared Operational Satellite (TIROS). Additional satellite and surface data from the U.S. NAVY operational analysis were used by ISCCP to compare values and optimize the final datasets. Daily measurements of atmospheric temperature and humidity profiles, ozone column measurements and information of snow and ice coverage are reported through these data archives. Other atmospheric and surface variables, such as merged snow and ice data were added to the ISCCP project to analyze

distinctive properties of clouds where available. Some of the analysis of the original data suggested a link between GCRs and cloud cover.

Rossow et al. [2002] used statistical methods to evaluate cloud variability on a mesoscale. They reduced the impact of albedo and emissivity biases by treating clouds as homogeneous in the horizontal direction, based on a limited study scale. The ISCCP project was developed to determine if relationships exist between “cloud water content, radiation, and atmospheric dynamics at the smallest scales, stimulated by the advent of prognostic cloud water schemes in global atmospheric circulation models (GCMs)” [Rossow et al., 2002]. The ISCCP methodology used statistical quantities to represent the radiative effects of clouds at the expense of accuracy in their model. The following section, defining the series of equations and explanations describing the statistical computations used in the ISCCP analysis, is extracted from Rossow et al. [2002] of which the variability statistics were originally developed by Cairns et al. [2000].

Three normalized values for a randomly-varying cloud composition with relatively weak variability were computed as:

$$\sigma'_{ext} = (1 - \epsilon_p)\sigma_{ext} \quad (3.11)$$

where  $\sigma_{ext}$  is the extinction cross section and  $\epsilon_p$  represents a correction factor for an inhomogeneous cloud particle density distribution.

$$\varpi'_0 = \varpi_0 \left[ 1 - \frac{\epsilon_p(1-\varpi_0)}{1-\epsilon_p} \right] \quad (3.12)$$

where  $\varpi_0$  describes the single scatter albedo and

$$\varpi'_0 g' = \varpi_0 g \left[ 1 - \frac{\epsilon_p(1-\varpi_0 g)}{1-\epsilon_p} \right] \quad (3.13)$$

where  $g$  represents an asymmetry parameter.

For these equations,  $\epsilon_p$  and  $\alpha$  were computed as

$$\epsilon_p = \frac{1}{2}(\alpha - \sqrt{\alpha - 4V}) \quad \text{and} \quad \alpha = \frac{1 + \sigma_{ext} l_c}{\sigma_{ext} l_c} \quad (3.14)$$

where “ $V$  is the relative density of the particle density distribution and  $l_c$  is the effective correlation length of the variations” [Rossow et al., 2002].

From these equations, movement of results to a larger scale by understanding variability of cloud constituents on changes in radiation, involved the computation of an effective cloud tau defined by:

$$\tau' = (1 - \epsilon_p)\tau \quad (3.15)$$

$$\text{where} \quad \tau = \int \sigma_{ext}(\zeta z) d\zeta = Y_z = \cos \theta \int \sigma_{ext}(\zeta s) d\zeta = \cos \theta Y_s \quad (3.16)$$

and where “ $Y$  is the optical path (the line integral of extinction) and  $z$  and  $s$  are unit vectors in the vertical and in any arbitrary direction, respectively” [Rossow et al., 2002].

This relationship with respect to the cloud medium is illustrated in Figure 3.7.

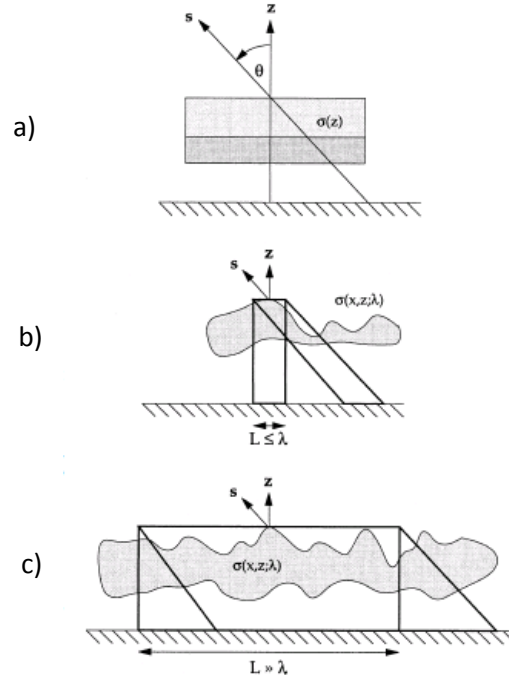


**Figure 3.7: “Schematic illustrating different assumptions about variations of optical media used to model radiative transfer through cloudy atmospheres: (a) horizontally homogeneous layers with properties that vary only in the vertical, (b) horizontally and vertically inhomogeneous layer, (c) horizontally and vertically inhomogeneous layer that is statistically homogeneous in the horizontal direction” [from Rossow et al., 2002, with permission].**

This last computation (in equation 3.16) was only suitable in consideration of changes in the extinction variable traveling vertically. To handle changes in optical thickness ( $\tau$ ) in the horizontal direction due to spatial variations in the optical path, absolute horizontal homogeneity was changed to statistical homogeneity computed from satellite observations using an averaging technique as follows:

$$\tau_L = \frac{\int \sigma_{ext}(Lx, \zeta z, \lambda) d\zeta dL dL}{\int dL dL} \approx \frac{\cos \theta \int \sigma_{ext}(Lx, \zeta s, \lambda) d\zeta dL dL}{\int dL dL} \quad (3.17)$$

where  $L$  is the evaluation over an extensive area and is much greater than  $\lambda$ .

In this scenario,  $\tau'$ , from equation 3.15, describes the mean cloud tau (optical thickness) and  $\epsilon_p$  (equation 3.14) provides a direct quantification of the degree to which the particle

density distribution variability limits the effective optical thickness of a cloudy versus homogeneous case. In addition, cloud edge detection precision may be as poor as 100-300 m while using satellite radiation measurements. Thus, cloud cover measurements should consider regions greater than this scale [Rossow et al., 2002, Rossow, 2011].

To develop a reasonable parameter definition for  $\epsilon_p$  to use in the case of extensive-scale satellite input in the ISCCP project, initial definitions of the normalized version of the optical thickness distribution were defined by the following first moments:

$$\text{Linear mean} = \bar{\tau} = \sum p(\tau_i)\tau_i \quad (3.18)$$

$$\text{Radiative mean} = \hat{\tau} = R^{-1}\{\sum p(\tau_i)R(\tau_i)\} = R^{-1}\{\overline{R(\tau_i)}\} \quad (3.19)$$

where  $R$  is the radiative transfer operator that determines the optical thickness radiative flux, and the

$$\text{Logarithmic mean} = \tilde{\tau} = \exp\{\sum p(\tau_i)\ln\tau_i\} = \exp\{\overline{\ln\tau_i}\} \quad (3.20)$$

From these parameter definitions, the inhomogeneous remote sensed cloud field can be given by

$$\epsilon = 1 - \frac{\hat{\tau}}{\bar{\tau}} \quad (3.21)$$

and the corrected mean cloud tau becomes

$$\hat{\tau}' = (1 - \epsilon)\bar{\tau} \quad (3.22)$$

In the case of infrared signals,  $\epsilon$  can be redefined as  $\epsilon_{IR}$  as follows:

$$\epsilon_{IR} = 1 - \frac{\hat{\tau}_{IR}}{\bar{\tau}_{IR}} \quad (3.23)$$

Emissivity is then defined as:

$$E = 1 - \sum[p(\tau_i)\exp(-b\tau_i)] = 1 - \overline{\exp(-b\tau_i)} = 1 - \exp(-\hat{\tau}_{IR}) \quad (3.24)$$

where  $b$  is a coefficient that uses cloud particle phase to relate visible to infrared optical thickness. Emissivity bias is then determined from:

$$E_{pp} - E = -\exp(-\bar{\tau}_{IR}) + \exp[-(1 - \epsilon_{IR})\bar{\tau}_{IR}] \quad (3.25)$$

where  $E_{pp}$  is the plane-parallel homogeneous emissivity.

An approximate empirical relationship that estimates the emissivity of homogeneous cloud cover, based on pixel-level cloud data from 16 regions and plotted in Figure 3.8 is described as:

$$\epsilon'_{IR} = 1 - x + \sqrt{\rho^2 - (x - \epsilon)^2} \quad (3.26)$$

$$\text{where } x = \frac{1}{2}(1 + \sqrt{2\rho^2 - 1}) \text{ and} \quad (3.27)$$

$$\rho = 1 + \frac{3.65}{\tau} \quad (3.28)$$

where  $\rho$  describes the radius of a circle passing through points (0,0) and (1,1) and that fits the curvature of the relationship [Rossow et al., 2002]. This curvature and previous emissivity relationships are shown in Figures 3.8 and 3.9.

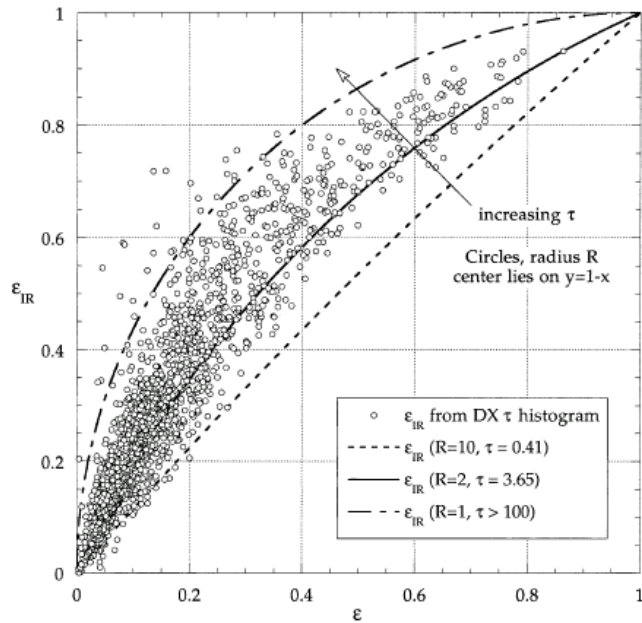


Figure 3.8: “Observed relationship of  $\epsilon_{IR}$  and  $\epsilon$  for all special study areas” [from Rossow et al., 2002, with permission].

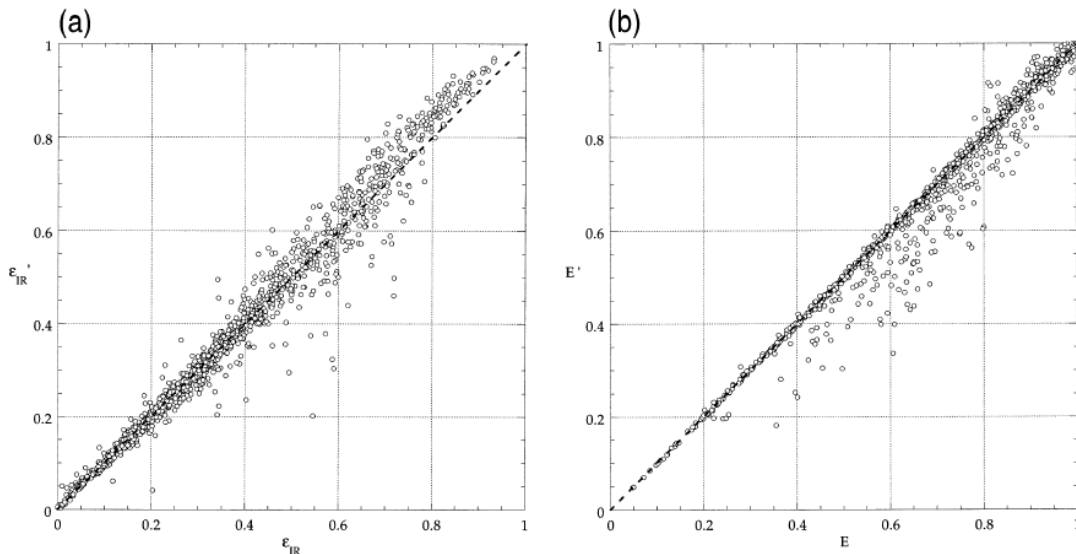
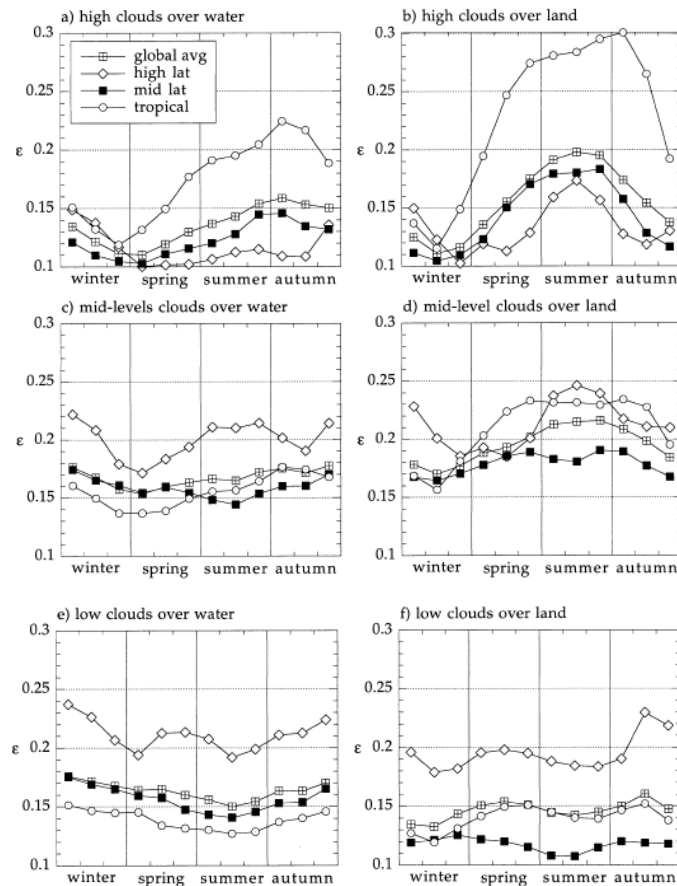


Figure 3.9: “(a) Estimated values,  $\epsilon'_{IR}$ , vs the true values,  $\epsilon_{IR}$  and (b) Estimated values of emissivity,  $E'$ , vs. the true values,  $E$ ” [from Rossow et al., 2002, with permission].

The curves for the plot in Figure 3.8 “are for circles with different radii that are functions of optical thickness that all pass through the points (0, 0) and (1, 1)” [Rossow et al., 2002].

In Figure 3.9 (a), “the estimated values are calculated from an empirical relation with  $\bar{\tau}$  and  $\epsilon$ ” while in (b), these estimates are based on an “empirical relation with  $\epsilon_{IR}$ ” [Rossow et al., 2002].

This work allowed for extension of cloud definitions to incorporate variability within clouds and express this in terms of various cloud parameters as outlined in Appendix B. In Figure 3.10, scenarios demonstrate seasonal differences in the inhomogeneous cloud field between observations over land and water from the work done at the ISCCP. The high latitude, high clouds show a peak in early autumn and lows over the winter months while mid-level clouds display highs during summer months.



**Figure 3.10: “Seasonal variations of  $\epsilon$  for high-, mid-, and low-level clouds averaged over the whole globe and over three latitude zones (tropical =  $\pm 15^\circ$ , mid-latitudes =  $\pm 30-60^\circ$ , high latitudes =  $\pm 60-90^\circ$ )” [from Rossow et al., 2002, with permission].**

Polar ice clouds are identified through the ISCCP dataset by an applied ice cloud microphysics model. They are defined as having cloud top temperatures ( $T_c$ ) below 260 K. The ice crystals within these clouds are considered to be of polycrystal type with sizes ranging between 20 and 50  $\mu\text{m}$ , based on a -2 power law distribution with an effective radius of 30 and 0.1 variance. This definition is implied from a “near-global survey of ice cloud particle size” conducted by Han [1999] [Rossow and Schiffer, 1999]. See Table 3.4 for further details of the ISCCP mean cloud top pressure, tau range, and liquid / ice cloud definitions for various cloud types.

**Table 3.4: Definitions of liquid and ice clouds for each cloud type based on ranges of mean cloud top temperature and tau. [from Rossow et al., 1996].**

NAME	PC RANGE (mb)	TAU RANGE	TYPE CODE
LOW			
Cumulus	> 680	$\leq 3.55$	1 (liquid), 4 (ice)
Stratocumulus	> 680	3.55 - 22.63	2 (liquid), 5 (ice)
Stratus	> 680	> 22.63	3 (liquid), 6 (ice)
MIDDLE			
Alto cumulus	440 - 680	$\leq 3.55$	7 (liquid), 10 (ice)
Altostratus	440 - 680	3.55 - 22.63	8 (liquid), 11 (ice)
Nimbostratus	440 - 680	> 22.64	9 (liquid), 12 (ice)
HIGH			
Cirrus	$\leq 440$	$\leq 3.5$	13 (ice)
Cirrostratus	$\leq 440$	3.5 - 22.63	14 (ice)
Deep Convective	$\leq 440$	> 22.63	15 (ice)

Determination of the model limit of 260 K to define ice clouds versus liquid clouds was based on water path analysis performed by Lin and Rossow [1996]. This analysis investigated the “rates at which water mass enters and leaves the particular air volume and the rate at which water mass is changed from one form to another within the volume of air” [ISCCP Webmaster, 2005]. These rates are effected by atmospheric motions of water vapour and air that can either contribute to increased (accumulation situations where particle sizes increase, as in CCN development) or decreased (in the case of upwards air movement effecting fall rates) sedimentation rates. Upward motions cause a cooling effect and contribute to phase changes of cloud particles from liquid to ice. “In polar regions and at very high altitudes, an air parcel may also cool by radiative heat loss” [ISCCP Webmaster, 2005]. Additional growth of cloud particles occurs when atmospheric

water vapour becomes supersaturated. For example, when examining cirrus clouds, increased size of ice crystals has an effect of raising the sedimentation rate while lowering the condensation rate of the cloud, until equilibrium is established. Overall cloud development is dependent on the “rate of air parcel cooling, temperature, the phase of the particle (liquid or ice), the size of the particles, and the number of growing particles per unit volume” [ISCCP Webmaster, 2005]. See Figure 3.11 which illustrates these changes.

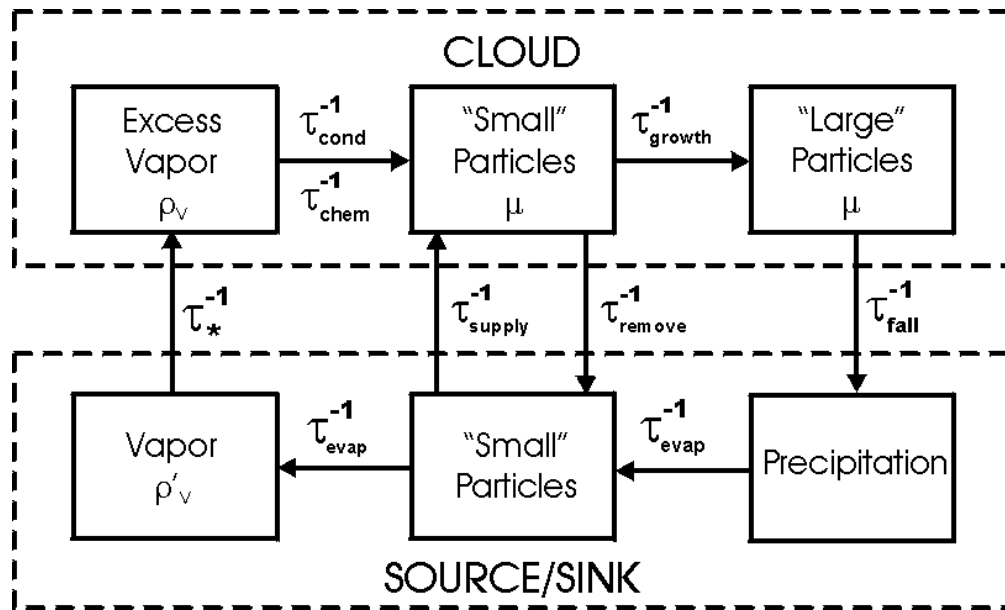


**Figure 3.11: “Conditions for cloud changes based on atmospheric vapour inputs and cooling effects” [from ISCCP Webmaster, 2005].**

The further study of water path analysis by Rossow [1999] demonstrated that the “ratio of liquid water path (from microwave) to the total water path (from visible reflectance) falls below 50%” at a temperature of 260 K on average [Rossow and Schiffer, 1999].

### 3.2.1.1 Documented Errors in ISCCP Measurements

Several challenges in estimating cloud cover from satellite sources were identified in the ISCCP documentation. Pixels are identified as cloudy if the data collected from the infrared or visible radiance detectors differs from the clear sky value. Over ice-free ocean

regions, this value is quite accurate, but over land surfaces covered in snow or ice or in dark conditions (night time or over the winter months), detection is more difficult or impossible. These detection issues are due to lack of contrast between the cloud and surface and the inhomogeneous nature of clouds. They contribute to systematic error in the results. In general, the ISCCP total cloud amounts are underestimated by up to 10 percent annually from actual values. This estimate is based on comparisons of ISCCP data to “over 670,000 individual cloud surface observations and surface-based cloud climatology” and exhibits a greater discrepancy over winter compared to summer months [Rossow and Schiffer, 1999]. Corrections were computed by applying the difference between the VIS/IR to IR daytime results to these underestimated values. Additionally, comparisons to the Stratospheric Aerosol and Gas Experiments (1995) and the High-Resolution Infrared Sounder (1996, 1997) detailed that stratospheric cloud estimates are lower than actual cloud amounts by 5 to 10 percent. This was reported to occur in the cases of very thin stratospheric clouds over the ocean where cloud density or  $\tau \leq 0.1$  or over land regions that exhibited a  $\tau$  value  $\leq 0.3$  [Rossow and Schiffer, 1999]. Polar regions demonstrate even further challenges in cloud detection due to decreased temperatures of formation of clouds, causing differences between clouds surface temperatures that are negligible or may even be reversed (cloud temperature > surface temperature). This can happen in the case of atmospheric inversions. Fewer cloud surface observations exist in polar areas due to accessibility issues and environmental conditions and, therefore, were unavailable for the ISCCP comparison studies. It is estimated that polar sky cloud amounts vary from actuals by being about 10 percent underestimated in summer months [Rossow and Schiffer, 1999]. Other variables affecting cloud cover fraction accuracy can be found in Table 3.5 and corrections applied to produce improved detection limits of certain parameters are detailed in Table 3.6.

**Table 3.5. Cloud cover fraction accuracy showing contributing variables and their effects on the ISCCP data [from Rossow and Schiffer, 1999].**

<b>Contributing Variables:</b>	<b>Effects:</b>
<p><b>Size distribution of cloud elements</b></p> <p><b>Spatial resolution of satellite sensor</b></p>	<p><b>Cloud cover fraction overestimated if sensor resolution is larger than the most frequent cloud element size (inferior for off-nadir views )</b></p>
<p><b>Detection sensitivity of the analysis dependent on cloud properties</b></p> <p><b>Space-time sampling characteristics of the dataset</b></p>	<p><b>Finite detection threshold exists for broken or scattered clouds that are optically thin</b></p>
<p><b>Size of the area and time scale for which cloud properties remain constant</b></p> <p><b>Size of the area in which cloud fraction is calculated</b></p>	<p><b>Satellite and surface resolutions differ by an order of magnitude, surface observations being of higher resolution; RMS differences between satellite and surface sampling of scattered clouds are close to 25% although the mean values are similar and, for all cloud types, this value reduces to 15%</b></p>

**Table 3.6: Threshold corrections applied to the ISCCP datasets resulting in improved detection limits of cloud top height and cloud optical thickness for total cloud cover [from Rossow and Schiffer, 1999].**

<b>Contributions:</b>	<b>Effects:</b>
<b>IR threshold reduced to 4K over land from original value of 6K</b>	<b>Improved overall bias in total cloud amount and enhanced detection of cirrus clouds over land</b>
<b>Conversion of VIS radiance threshold to a reflectance threshold (overall decrease)</b>	<b>Reduced small low bias over high-latitude oceans</b>
<b>Reduction in VIS and IR thresholds and addition of 3.7mm wavelength radiance tests over ice/snow surfaces</b>	<b>Improvement in low bias over polar regions, mostly effecting summertime values</b>

The accuracy of the modeling work done during the ISCCP is limited by the use of cloud temperature to derive cloud phase parameters. This may contribute to the addition of super cooled liquid clouds in the ice cloud determinations.

### **3.2.2 DARDAR Cloud Data**

In addition to the ISCCP dataset utilized in this study, a more accurate portrayal of ice clouds and their properties was derived from the work by Julien Delanoë and the team at Lille University in France. The range of available data from this project was from June 2006 to December 2010. This work successfully combined the 94 GHz radar data from CloudSat, lidar data from CALIPSO (Cloud-Aerosol Lidar and Infrared Pathfinder Satellite Observations) and spectroradiometer data from MODIS (Moderate Resolution Imaging Spectroradiometer) satellite missions to isolate ice cloud properties from clouds. Each of these satellite data repositories contributed to the discrimination of cloud and aerosol microphysical properties for the project and they are detailed in Table 3.7.

**Table 3.7: Satellite missions and their contributions towards data retrievals of cloud properties [from Delanoë and Hogan, 2010].**

Satellite Mission:	Contributions:
<b>CloudSat</b>	<b>Cloud liquid and ice water content</b>  <b>Effective radius and related quantities</b>
<b>CALIPSO</b>	<b>Ice cloud optical depth</b>  <b>Visible extinction</b>  <b>Ice water path</b>  <b>Ice particle size</b>
<b>MODIS</b>	<b>Effective radius</b>  <b>Optical depth</b>

Due to deficiencies in each of these datasets, such as attenuation considerations of using lidar data and inability of radar to detect thin clouds and limited penetration of infrared radiances into deep ice cloud formations, a significant effort went into the planning stage to take advantage of strengths in each. A flowchart of the ICARE modeling technique is shown in Figure 3.12.

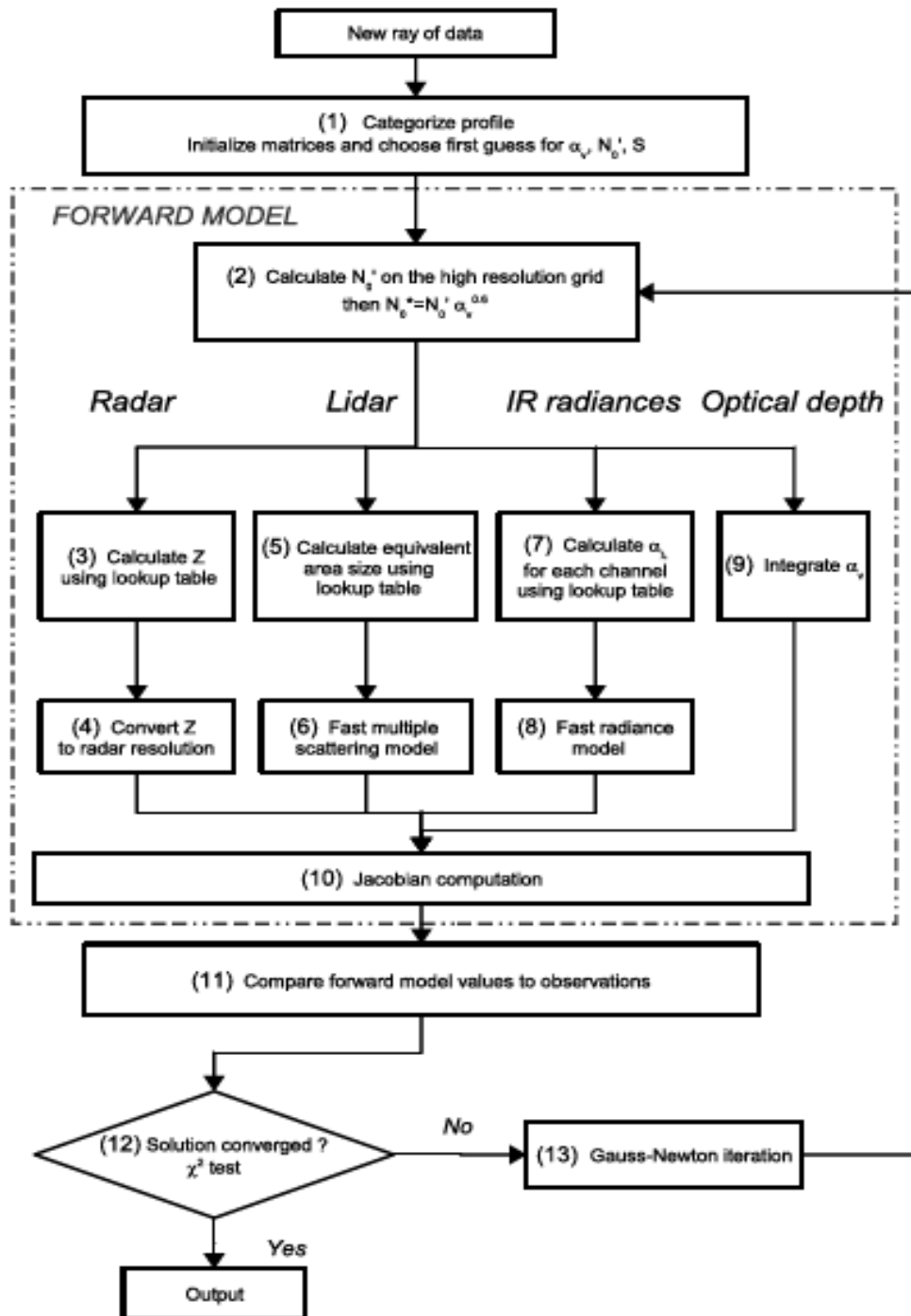


Figure 3.12.: Flowchart detailing the retrieval scheme used in the ICARE modeling technique producing the DARDAR data products [from Delanoë and Hogan, 2008].

A variational method was used to overcome these deficiencies and focus on ice cloud properties. In this method, the visible extinction coefficient,  $\alpha_v$ , was described by the state vector,  $x$ , and related to lidar readings and optical cloud depth in the geometric

optics limit as follows (the subsequent set of equations and explanations is taken from Delanoë and Hogan, [2010]):

$$x = \begin{pmatrix} \ln \alpha_{v,1} \\ \ln \alpha_{v,n} \\ a_{\ln S} \\ b_{\ln S} \\ \ln N_{b,1} \\ \ln N_{b,m} \end{pmatrix} \quad (3.29)$$

where  $S$  is the extinction-to-backscatter ratio assumed to remain constant with height except where actual measurements of  $\alpha_v$  were retrieved. “The visible extinction coefficient,  $\alpha_v$ , is directly linked to the lidar measurements and the optical depth of the cloud, and [in using equation 3.29] is represented by a value at each of the gates that ice is detected” [Delanoë and Hogan, 2010].

In Delanoë and Hogan’s [2010] model,  $\ln(S)$  was treated as a factor that changes with altitude since this element was shown to vary linearly with temperature. This mimics nature where temperature is known to vary linearly with height. This relationship is described as:

$$\ln(S) = a_{\ln S}(z - z_{mid}) + b_{\ln S} \quad (3.30)$$

where  $z$  is the altitude and  $z_{mid}$  is the height of the middle of the cloud,  $a_{\ln S}$  and  $b_{\ln S}$  were given as the slope and cloud middle value of  $\ln(S)$ , as sampled by lidar, respectively. [Delanoë and Hogan, 2010]

Forward modeling was done using a shape-particle size distribution described by:

$$N(D) = N_0^* F\left(\frac{D}{D_m}\right) \quad (3.31)$$

where  $F$  is the unified size distribution shape and  $N_0^*$  was the “normalized number concentration parameter” determined by:

$$N_0^* = \frac{4^4 M_3^5}{6 M_4^4} \quad (3.32)$$

where  $M_n$  is the  $n^{\text{th}}$  moment of the ice particle size distribution. The normalized particle size was given as  $D_m$ , or the mean of the distribution as:

$$D_m = \frac{M_3}{M_2} \quad (3.33)$$

In the forward model, contributions of mid-latitude ice cloud mass-size and area-size relationships were extracted from aircraft measurements as described by Brown and Francis [1995] and Francis et al. [1998]. Additional components in the model included the use of geometric optics to generate values of  $\alpha_v$ , Mie theory to develop the radar reflectivity factor,  $Z$ , where particles were considered “homogeneous ice-air spheres of diameter  $D$  and mass  $m$ ”, and calculation of ice water content (iwc) where particle mass was integrated across the size distribution (Appendix C) [Delanoë and Hogan, 2010]. Effective radius,  $r_e$ , was computed using the formula:

$$r_e = \frac{3 \text{ iwc}}{2 \alpha_v \rho_i} \quad (3.34)$$

where  $\rho_i$  is the density of solid ice.

Lidar-attenuated backscatter was incorporated into the model. This was done by utilizing the “multiple-scattering model”, developed by Hogan et al. [2006], which required equivalent-area radius inputs. Look-up tables for scattering and absorption properties and estimates of atmospheric variables such as temperature, pressure, humidity and ozone profiles, CO<sub>2</sub> concentrations, skin temperature, emissivity and computed state vector values ( $\alpha_p$  and  $N'$ ) were needed to compute a “two stream source function technique” for the model [Delanoë and Hogan, 2010]. The  $N'$  relationship, as a function of measured temperature, was determined from linearly varying values as:

$$\ln N' = 22.5 - 0.089T \quad (3.35)$$

where  $T$  is temperature in degrees Celsius.

Additional considerations derived from the ECMWF analysis for the ice cloud forward model included thermodynamic aspects of the atmosphere, surface dynamics of the Earth (i.e. skin temperature, emissivity) and instrument parameters (i.e. field-of-view for lidar) [Delanoë and Hogan, 2010].

### **3.2.2.1 Documented Errors for the DARDAR ICARE Modeling Technique**

Errors for this procedure were summarized in Table 3.8:

**Table 3.8: Error sources from Forward Modeling work in combining CloudSat-CALIPSO and MODIS retrievals [from Delanoë and Hogan, 2010].**

Error Sources from Forward Modeling:	Contributions:
Radar (Z)	$\Delta Z_{micro} = 1 \text{ dB} = \text{random error in microphysical assumptions}$
CloudSat Instrumental Error	<p>Systematic error based on calibration bias (changes of 1dB calibration results in 10% error added to iwc)</p> <p>Random error based on a single standard deviation defined by</p> $\Delta Z_{dB} = \frac{4.343}{\sqrt{M}} \left( 1 + \frac{1}{SNR} \right)$ <p>Background noise (in dBZ) as</p> $N_{dBZ} = -131.4 + 20 \log_{10}(r)$ <p>with the linear signal-to-noise ratio given by:</p> $SNR = 10^{0.1(Z_{dBZ} - N_{dBZ})}$
Lidar (S)	Complicated by assumption of constant nature with height. Corrected through use of lidar backscatter profiles.
CALIPSO Instrument Error	<p>The measured backscatter random error due to noise is defined by</p> $\Delta\beta = \left\{ NSF^2\beta + \left( \frac{r^2}{C} \right)^2 \left[ (\Delta V_b)^2 + (\Delta \bar{V}_b)^2 \right] \right\}^{\frac{1}{2}}$ <p>where NSF is the Noise Scale Factor, <math>r</math> is the distance of each lidar gate from the satellite in meters, <math>C</math> is the lidar calibration constant, <math>\Delta V_b</math> is the standard deviation of the background signal-power, <math>\Delta \bar{V}_b</math> is the standard error of the mean background signal</p>
Infrared Radiance Errors:	Dependent on cloud thickness, surface temperature and error in meteorological parameters (i.e.

	<p>temperature profile)</p> $\Delta I_{\lambda}^2 = \Delta T_c^2 \epsilon_c^2 [dB(T_c)/dT_c]^2 + \Delta T_s^2 (1 - \epsilon_c)^2 [dB(T_s)/dT_s]^2 / \pi^2$ <p>where <math>\Delta I</math> is the error variance of the radiance, <math>\Delta T_s</math> is the skin temperature error, <math>\Delta T_c</math> is the cloud temperature error, <math>T_c</math> is the cloud top temperature, <math>T_s</math> is the skin temperature and <math>\epsilon_c</math> is the cloud emissivity.</p>
Infrared Measurements	0.5% based on radiance measurements for each MODIS wavelength
Radar-Lidar Colocation	0.1 to 0.7 dB based on overlapping versus separation by 1 km for recorded signals

The result of this work produced a product that demonstrated accurate particle size determination within the cloud formation with height [Delanoë and Hogan, 2010] and had continuous cloud predictions using both the radar and lidar schemes.

### 3.3 Cosmic Ray Data

Cosmic ray data is continuously gathered at various locations around the world. The data source for this research was a single neutron monitor station located at Thule, Greenland. It was chosen due to its unique polar measurement capabilities, location and long duration of collected data (1957-2011).

#### 3.3.1 Cosmic Ray Detection Equipment and Data Sources

Neutron monitors count incoming secondary nucleons, neutrons that are not slowed by ionization loss and are a result of collisions of primary cosmic rays with atmospheric particles (Figure 3.13). These collisions initially take place in the atmosphere at an altitude of about 30 km and the secondary particles travel towards the Earth in a cascading effect.

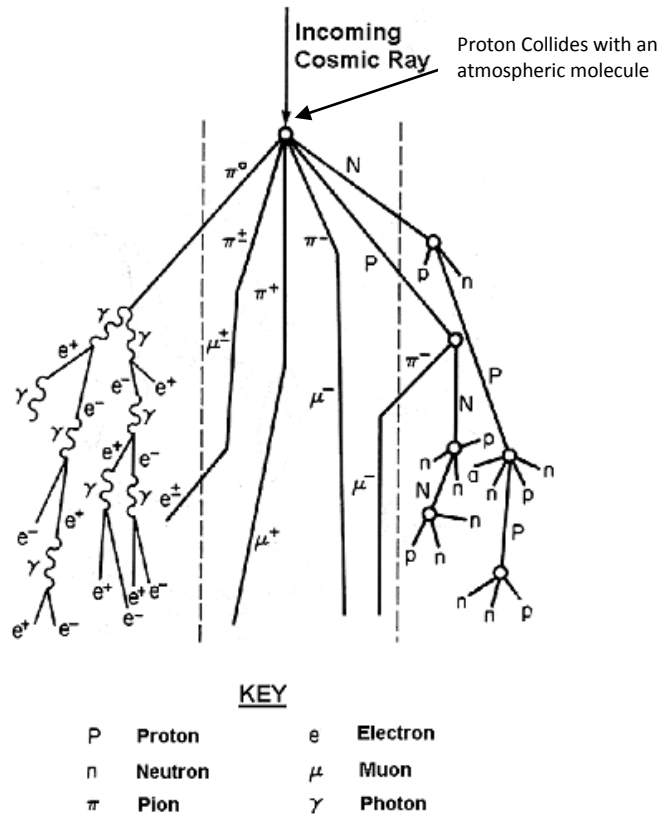


**Figure 3.13: An atmospheric proton-molecule collision. In showers of GCRs, this type of collision can produce billions of particles known as secondary cosmic rays, resulting in an atmospheric cascade [Spaceship Earth, 2000].**

An example of a set of reactions resulting from this process is as follows:



The primary cosmic ray particle must have a rigidity that exceeds the geomagnetic cutoff rigidity at that location in order to enter the Earth's atmosphere. At the poles, the cutoff rigidity is effectively 0 GeV while at the equator this value is up to 17 GeV. Given this, an energy greater than 1.0 GeV is required of the primary particle in order for it to penetrate the Earth's atmosphere and its secondary neutrons to be detected at a sea-level ground-based station [Moraal et al., 2000]. See Figure 3.14 for a depiction of particle incident energies required for detection of cosmic rays at sea level.

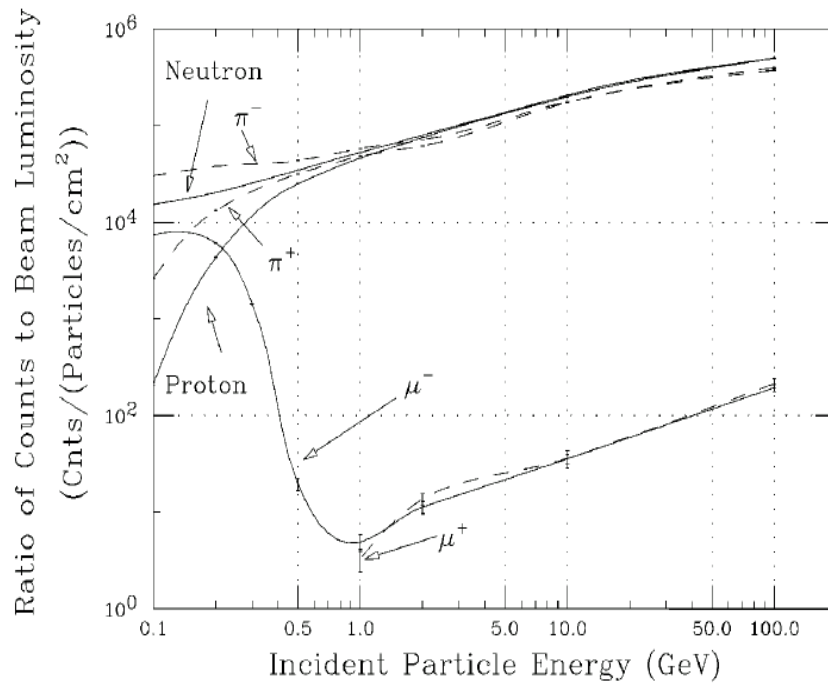


**Figure 3.14: “Standard (BP-28 proportional tubes) NM-64 calculated detection efficiency for secondary particles arriving in the vertical direction” [from Clem and Dorman, 2000, with permission].**

Computation of the contributions from various particles detected at sea level are shown in Figure 3.15. In this figure, the dominant contribution was found to be from secondary neutrons.

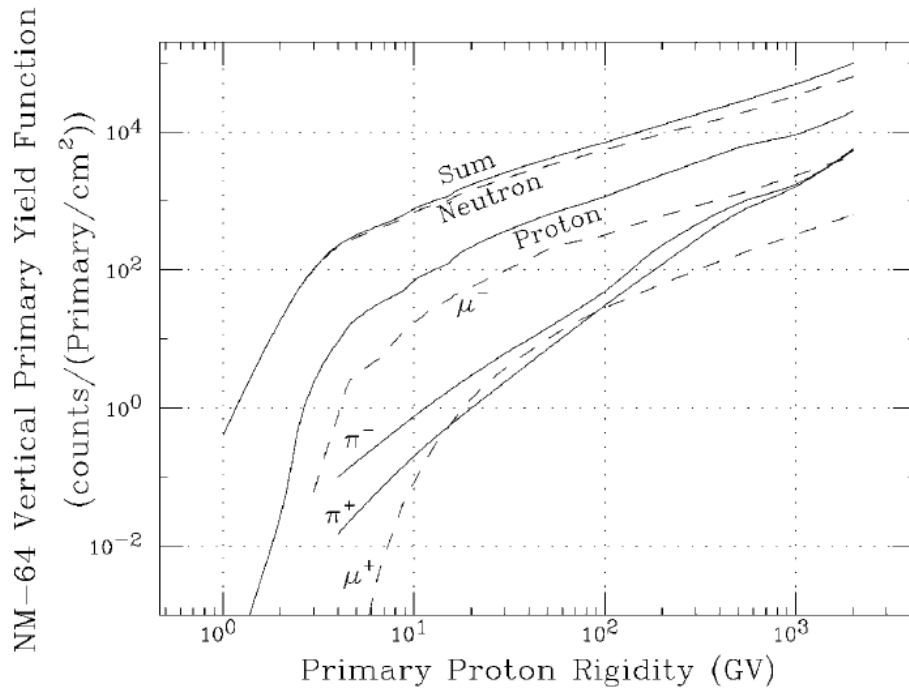


**Figure 3.15: “Calculated yield function spectra of NM-64 counts at sea level from vertical incident primary protons is shown (top line). The individual contributions made by secondary components to the vertical proton yield function are separated into different curves.” [from Clem and Dorman, 2000, with permission].**

Ground-based stations serve to measure the small intensity variations, mostly anisotropic, from these high-energy cosmic rays. Neutron monitors are sensitive to data in the range of 1-20 GeV, which is considered the low-energy portion of the spectrum. Exceptions to normal measurements create anomalies or spikes in the readings and are occasionally reported as having a distinctive solar source. These anomalies or “ground level enhancements” are of limited duration, occur about 10 to 15 times per decade and are sourced from our sun during energetic solar events. They can be corrected in individual station datasets due to the large number of monitoring stations around the world, currently about 50 active ones, detecting such influences [NOAA Website].

Parameterization of the counting rate,  $N$ , was developed from near or at sea-level stations to hold the following relationship [the following series of equations is sourced from Moraal et al., 2000]:

$$N(P_R > P_{gc}) = N_0 \left[ 1 - \exp(-\alpha * P_{gc}^{-k}) \right] \quad (3.37)$$

where  $P_R$  is the primary cosmic ray rigidity,  $P_{gc}$  is the geomagnetic cutoff rigidity,  $N_0$  is the normalization value, and  $\alpha = 10$  and  $k = 0.95$  at sea level during a solar minimum.

$N_0$  effectively describes the measurements from a 3NM64 neutron monitor as being 125,000 counts per hour at the poles. Counting rates may vary by 5% when comparing results from different solar minimums [Moraal et al., 2000].

Adding a pressure component, as it relates to measurements in the atmosphere, results in adjustments to this equation and estimates within 5% of actuals:

$$N(P_R > P_{gc}) = N_0 \left[ 1 - \exp(-\alpha * P_{gc}^{-k}) \right] \exp[\beta(p_s - p)] \quad (3.38)$$

where  $\alpha = 10$  and  $k = 1.4 - 0.0006 p$ ,  $p$  is atmospheric pressure in mmHg,  $\beta = 1\% \text{ mm}^{-1} \text{Hg}$  and  $p_s = 760 \text{ mmHg}$ .

A formula incorporating the differential rigidity spectrum allows binning of the “counting rate in terms of rigidity” [Moraal et al., 2000] where its maximum value is at

$P_R = \left[ \alpha * k / (k + 1) \right]^{1/k}$  is as follows:

$$-dN/dP = N_0 * \alpha * k * P_R^{-k-1} \exp(-\alpha * P_R^{-k}) \exp[\beta(p_s - p)] \quad (3.39)$$

This differential spectrum is associated with the upper atmosphere primary particle intensity spectrum  $j(P_R)$  in the following manner:

$$-dN/dP = \sum_{species} S(P_R, x) j(P_R) \quad (3.40)$$

As these equations are time independent and only accurate below 30,000 feet of altitude, they describe the “cosmic ray spectrum inside of the atmosphere” [Moraal et al., 2000].

Location and altitude of neutron monitor stations have a direct effect on sensitivity of equipment to the cosmic ray spectrum. Higher altitude stations allow greater detection of cosmic rays due to decreased atmospheric dispersion and attenuation. The calculated attenuation length for cosmic ray particles in the atmosphere is  $100 \text{ g cm}^{-2}$ . Cosmic ray detectors that are designed to accept incoming rays from various directions are noted to have a high “asymptotic cone of acceptance” and thus, result in a more accurate count rate due to particle dispersion. As altitudes decrease, anisotropy of particles occurs through “local scattering and bulk flow conditions” [Moraal et al., 2000]. Some detectors are created to be responsive to variations in anisotropy. Cosmic ray intensity can be defined in terms of spherical harmonics of the counting rate as:

$$\delta N = \delta N_{00} + (\delta N_{10} + \delta N_{11}) + (\delta N_{20} + \delta N_{21} + \delta N_{22}) \propto c_{00} a_{00} + [c_{10} a_{10} + c_{11} a_{11} \cos(\phi_{11} - \chi_{11})] + \text{second order harmonics, etc.} \quad (3.41)$$

where  $\delta N_{10}$  and  $\delta N_{11}$  are the North-South anisotropy and diurnal variations,  $c_{mn}$  are the coupling coefficients,  $a_m n \equiv \left( \frac{\delta j}{j} \right)_{mn}$  are the primary variation amplitudes,  $\phi_{11}$  and  $\chi_{11}$  are the effective asymptotic longitude of the station and phase of the diurnal variation, respectively [Moraal et al., 2000].

Locations near the north and south poles have less interference due to the geomagnetic field and atmospheric disturbances, where rigidities are lower and provide a more accurate count of cosmic rays. In these regions, atmospheric effects are dominant. These include air mass overburden variations, corrected for by considering barometric pressures in stable conditions as:

$$dN = -\beta N dp \quad (3.42)$$

where  $dN$  is the variation in the count rate  $N$ ,  $\beta$  describes the attenuation or barometric coefficient, and  $dp$  is the barometric pressure change [Clem and Dorman, 2000].

The original series of neutron monitors were built and calibrated in the 1950s. They were put in place at high altitude locations around the globe, during the International Geophysical Year, 1956-57. The Bartol Research Institute established its first monitoring station at Thule, Greenland in 1957. It originally began as three 3-tube boron trifluoride ( $\text{BF}_3$ ) monitors lacking lead and moderating polyethylene cylinders in their structures. Updated instruments for detection were added in 2001 with tubes that incorporated helium-3 to capture neutrons. These were found to have the identical efficiency and energy response compared to the  $\text{BF}_3$  design [Mishev et al., 2008]. This nine-tube NM64 detector configuration is currently still active. It is located at building 561 on Thule Air Force Base with coordinates 76.5 degrees North latitude and 68.7 degrees West longitude at an altitude of 26 meters. This newer data was renormalized to improve the congruence between the datasets. The Thule monitor has a 0.10 GeV natural cutoff rigidity, due to its northerly position. Although the station is near sea-level, the Thule location is noted as one of the optimum stations for North-South particle detection since it sees close to 80% of the anisotropy (restricted asymptotic cone of acceptance) with high directional sensitivity and an angular resolution of 15 degrees. It is only modestly subjected to isotropic and diurnal variations. From intercalibration work performed in 1963 using several European stations, counting rate accuracy at Thule was in the range of  $\pm 1\%$  [Mishev et al., 2008].

## CHAPTER 4: DATA AGGREGATION

Data collection, along with the data manipulation and treatment stages are described in this chapter. Following the data sourcing, several decisions were made to bring the data into workable time-series formats for further analysis. These decisions involved how to handle missing data, the best ways to combine data, and what averages were needed for each dataset for comparison purposes. The following chapter will discuss what choices were made and how the datasets were handled.

All data used in this analysis were processed in a spreadsheet format, mimicking a database, where datasets were reviewed and compared. To do this, the datasets were first set up in a time-series format with extracted daily values or computed daily averages. Additional monthly or yearly means were calculated from these values. Dates were portrayed in several different formats to incorporate the various datasets while the format of DD/MM/YYYY was used in all charts.

### 4.1 Ozone Data

In this study, TOMS (V-8) and OMI data were originally extracted from the archived overpass database available from NASA [McPeters, 2011]. This data gathering was done by referencing Thule, Greenland as the overpass location. Based on the OMI outputs, distance from the station location to the OMI cross track position reached a maximum of 162.4 km with a mean value of 24.2 km. Due to the effects of seasonal lack of sunlight over the Thule station, most of the data was recorded between the 54 and 293 days of the year. Data from day 186 of 1994 to day 207 of 1996 was missing from this dataset.

To fill in missing ozone values, a third set of data was requested from NASA and represented SBUV/2 instrument total ozone profiles over 21 layers in Dobson units per layer. This data was extracted based on a radius of 200 km from the Thule, Greenland station. As this data has just been publicly released, documentation on parameterization and corrections will follow later in 2012. It is currently stored at the NASA Goddard DISC

(Data Information Services Center). These three data sources were compiled as a single data collection for analysis purposes.

A fourth set of data was extracted from the TEMIS website. This multi-sensor total column ozone overpass data was obtained for the years 1983 to 2008. This data was treated as a second dataset for this analysis (TEMIS, 2011). Both datasets were used in data comparisons in this research since it was unclear which one was the most accurate for northerly latitudes over Greenland.

#### **4.1.2 Manipulation of Ozone Data**

##### **4.1.2.1 TOMS-OMI-SBUV Satellite Ozone Data**

Daily average data was available for TOMS instrument recordings for 1983 to 1994 (Nimbus-7 and Meteor-3 missions) and 1996-2005 (Earth Probe mission). OMI data from 2004 to 2007 and SBUV data from 1989 to 2006 contained several recordings per day and daily averages were calculated to maintain consistency between the various data sources. All daily averages were arranged by date in a master spreadsheet.

The SBUV data for the period from 1989 to 2006 was added to the spreadsheet and substituted for the dates where data was missing. In the cases where both N11 and N14 SBUV data were available, N11 data was used. Details of days where SBUV data was added to the main dataset are provided in Appendix D.

##### **4.1.2.2 TEMIS Satellite Ozone Data**

The TOMS V8, OMI and SBUV/2 data (1983 to 2011) comprised one compiled dataset of individual satellite readings while the TEMIS modeled data was a second, additional dataset to be compared and utilized for this study (1983 to 2008). The original date stamps were edited to fit within the master spreadsheet and data was expressed as a time series format with daily average values and aerial extent reduced to a maximum of 200 km from the Thule, Greenland station.

#### **4.1.3.1 TOMS, OMI and SBUV Data**

Overlapping TOMS data values between 1991 and 1994 from the Nimbus 7 (1979-1992), METEOR-3 (1991-1994) and Earth Probe (1996-2005) satellite missions were averaged over the following dates: August 20 to August 31, 1991, February 25 to April 2, 1992, May 25 to July 12, 1992, August 31 to October 17, 1992 and March 31 to May 6, 1993. METEOR-3 TOMS V8 data values only were utilized from May 7 to August 18, 1993 and February 22 to June 1, 1994. OMI data (2004-2011) was averaged with TOMS (1996\_2005) for the dates from October 1 to 13, 2004 (excluding October 6, 2004) and February 27 to October 14, 2005 (excluding October 3, 2005).

From the final daily average ozone values, monthly and yearly averages were computed. These averages were examined and, even though some winter months lacked data or partial data was found for others, a general trend was observed in the monthly values. The trend indicated a peak that occurred either in March or April which decreased towards an annual low, generally occurring in October. The difference between these values was calculated to represent the recorded decrease in atmospheric ozone for that year, expressed as a seasonal reduction or loss value. This combined dataset is referred to as the satellite ozone data in this report.

#### **4.1.3.2 TEMIS Multi-Sensor Data**

A similar procedure was used for the TEMIS multi-sensor data where monthly averages were computed along with seasonal ozone reduction. Since data was available throughout the year, and due to differences in sources, the peak values were found between the months of January to April while the lower limit existed between August and November. See Table 4.1 for this complete data summary. In this table, the months showing annual maximums and minimums with computed differences are provided to the right for each data source.

Differences existed between TOMS, OMI and SBUV observations (individual satellites) versus the TEMIS multi-sensor project; Instead of having to average overpass values, as

was done with the TOMS and OMI data, the multi-sensor reanalysis project used only one overpass ozone value per day for comparison to ground-based stations.

**Table 4.1: Summary of both Individual Satellite and TEMIS Multi-Sensor Time Series data annual seasonal ozone reduction from 1983 to 2011, for available data.**

<b>Year</b>	<b>Individual Satellites Annual Maximum</b>	<b>Individual Satellites Annual Minimum</b>	<b>Seasonal Ozone Reduction (DU)</b>	<b>Multi-Sensor Annual Maximum</b>	<b>Multi-Sensor Annual Minimum</b>	<b>Seasonal Ozone Reduction (DU)</b>
1983	March	October	190.20	March	October	184.97
1984	March	October	195.48	March	October	194.88
1985	March	October	169.35	March	September	192.65
1986	March	October	158.91	March	November	158.32
1987	March	October	182.32	February	October	240.43
1988	March	October	197.74	March	October	188.10
1989	March	October	223.93	March	August	217.22
1990	April	August	99.74	February	August	144.30
1991	March	October	149.07	March	September	162.08
1992	March	October	156.36	April	October	136.77
1993	April	September	134.87	April	September	111.05
1994	April	September	161.45	April	September	164.87
1995	March	August	136.00	February	November	97.35
1996	April	October	154.45	April	October	135.73
1997	April	October	133.76	April	October	123.09
1998	April	October	156.88	April	September	152.91
1999	March	October	164.78	March	September	164.87
2000	April	September	132.08	April	September	134.33
2001	March	September	150.40	February	September	189.45
2002	April	October	196.62	February	October	231.26
2003	March	October	178.75	March	September	153.41
2004	March	October	158.38	January	October	170.11
2005	April	September	165.61	April	September	162.07
2006	March	September	168.59	February	September	175.06
2007	April	September	143.67	April	September	151.97
2008	March	October	165.54	March	August	156.76
2009	March	October	175.02	N/A	N/A	
2010	March	August	203.05	N/A	N/A	
2011	April	August	176.32	N/A	N/A	

## 4.2 Cloud Data

ISCCP gridded data solutions, extending from north 60 to 90 degrees latitude, were available through an online archive, but were not suitable for this study. Alternatively, the ISCCP DX data source was used. This DX data allowed for specific regional end-point

coordinates to be specified to extract pixel-level data. In this process of data retrieval, files that contained all available satellite data that met the regional and date criteria were received from the data center at the ISCCP.

The data area used for analysis was chosen as a 300 km diameter square centered at the coordinates for the Thule neutron monitor station. These coordinate ranges were from 75.20 to 77.88 north latitude and -63.02 to -74.53 west longitude (see Figure 3.1). All available DX data from the date range 1983 to 2008 were extracted. The dates received were limited by the project duration, which concluded on June 30, 2008. These data included measurements and recordings from the National Oceanic and Atmospheric Administration (NOAA) polar-orbiting satellites. This data generally exhibited 3-hour sampling, with pixels being 25 km apart, to estimate cloud variables from NOAA satellites. Based on this date range, the data satellite sources were NOAA-7, 9, 11, 14, 16 and 18 [Rossow, 2011].

The DARDAR dataset was not easily attainable from the University of Lille in France. Since DARDAR products are mapped on CloudSat granules, geolocated granules with identified record indexes over Thule were extracted from the CloudSat website (CloudSat Data Processing Center, 2012) and sent to the ICARE personnel at the University of Lille to capture all available datasets for this study. The files were received in a binary hierarchical data format (HDF) and contained data from June 15, 2006 to December 28, 2010. Examples of a CloudSat flight path and data sample over northwest Greenland are shown in Figures 4.1 and 4.2, respectively.

ICARE Project at the University of Lille in France

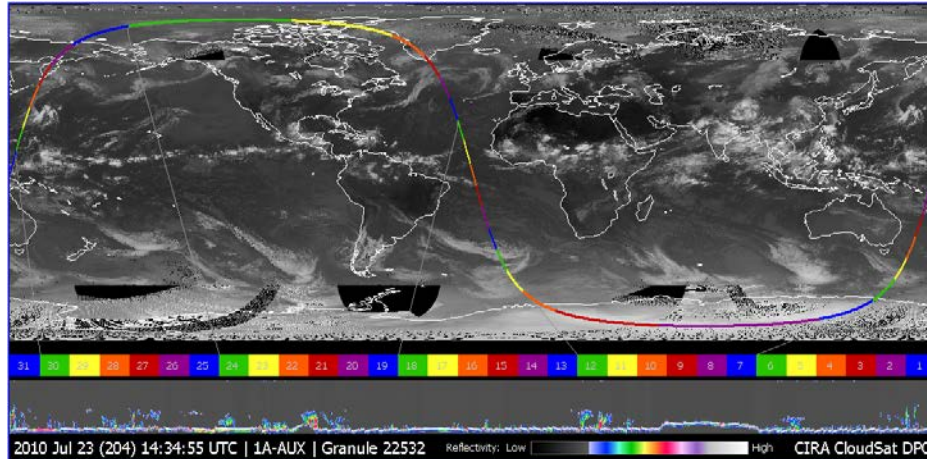


**Figure 4.1:** An example of CloudSat satellite retrieval coverage from the orbital path “quicklook” images for July 23, 2010, showing the flight path over Thule station in northwest Greenland [from ICARE, 2012].

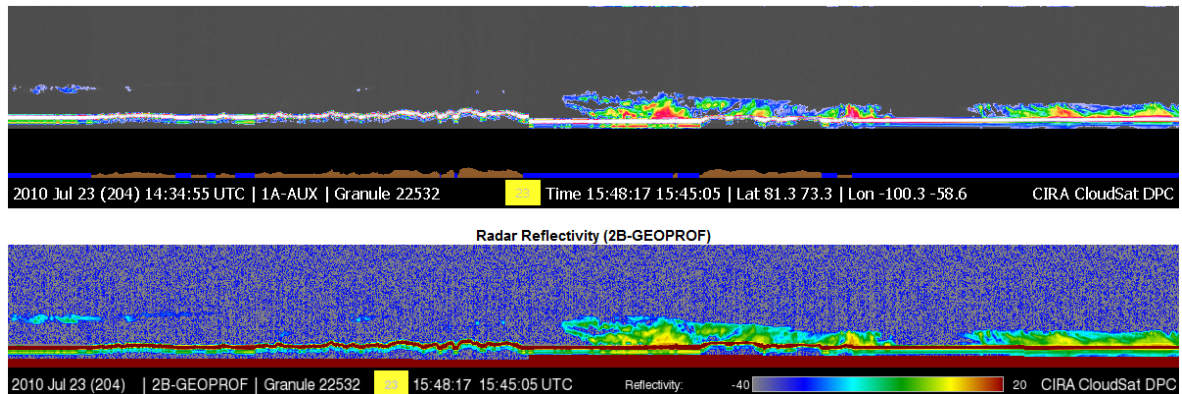


**Figure 4.2:** An example of a “quicklook” image showing radar reflectivity over the Greenland segment of cloud retrievals for July 23, 2010 [from ICARE, 2012].

## 4.2.1 Manipulation of Cloud Data

### 4.2.1.1 ISCCP Cloud Data

The data files received from the ISCCP data archives contain all available instances of encountered pixels within the areal extent of 150 km from the Thule, Greenland station from 1983 to 2008. The content and data ranges of the files were reviewed. Due to the considerable size and number of files received, processing was necessary to convert the files to a condensed, workable format.

The files collected from the ISCCP contained many cloud variables, such as latitude, longitude, ice cloud tau (optical thickness), day-night flags, ice cloud top temperatures and clear sky composite radiances. All available variables from the ISCCP dataset are outlined in Appendix B. The processing steps that were needed to convert the files from binary to ASCII format began with downloading and using an available Fortran read program from ISCCP. Editing of the program was done to specify restricted ranges of latitude and longitude and variables such as day-night flags (DAYNIT) and satellite types (SATTYP) to extract necessary ice cloud properties. The properties or variables considered at initial extraction included TMPTAB(VTAUIC) or VIS-retrieved ice cloud tau, TMPTAB(VTMPIC) or VIS-adjusted ice cloud top temperature and TMPTAB(VPRSIC) or VIS-adjusted ice cloud top pressure. Each of these were analyzed to define their usefulness for this study. Processing of all DX data files was automated using a script and output to a concatenated ASCII format for all available date ranges.

#### **4.2.1.2 ICARE DARDAR Cloud Data**

The large binary HDF format files received for the DARDAR dataset were reviewed and converted to ASCII format for further data analysis. An HDF Viewer program was used to gain familiarity with the datasets and view all variables in table format. To manipulate the data and reduce the large data files to a smaller, workable version, a combination of an available hdp program was utilized and awk scripts were created on a Linux platform. The hdp program allowed the HDF file content to be listed and dumped while the awk scripts permitted processing of the many, large data files. This process completed the binary to ASCII conversion and then the regional extent for the data was defined. All output files were pasted together to create a time-series format for all desirable variables. All available variables from the DARDAR project are shown in Appendix C. The variables that were extracted for this study are time, latitude, longitude, visible optical depth (vis\_optical\_depth) and visible optical depth error (vis\_optical\_depth\_err). Daily averages were computed for the dataset.

#### **4.2.2.1 ISCCP Cloud Data**

From the data manipulation stage, it was found that all day-night flags (DAYNIT) and satellite types (SATTYP) were consistent throughout the Thule, Greenland dataset. The ice cloud tau property, TMPTAB(VTAUIC), data was processed to output daily average values. In the resultant time-series version, average monthly ice cloud tau along with number of days per month and number of days per year of ice cloud existence were computed.

#### **4.2.2.2 ICARE DARDAR Cloud Data**

Daily average values of visible optical depth (vis\_optical\_depth) and visible optical depth error (vis\_optical\_depth\_err) from the DARDAR database were computed for the data files from June 15, 2006 to December 31, 2010. From this, average monthly ice cloud optical thickness and observed number of days per month and year of ice clouds were calculated.

The ISCCP and DARDAR data results for start and end dates for annual recordings along with the ratio of number of total recording days to those days where ice clouds were detected based on the existence of an ice cloud tau or thickness value are provided in Table 4.2. The maximum number of days with over 10 hours and 40 minutes of daylight over Thule, Greenland for each year is 201, based on recordings at Qaanaaq [Sunrise and Sunset in Qaanaaq, 2012].

**Table 4.2. Date ranges of available cloud data over Thule, Greenland; representing ISCCP data on left (columns 2 to 4) and DARDAR ICARE data on right (columns 5 to 7).**

Year	ISCCP start date for annual recordings	ISCCP end date for annual recordings	ISCCP ratio of recording days to number of days ice cloud tau recorded	DARDAR ICARE start date for annual recordings	DARDAR ICARE end date for annual recordings	ICARE ratio of recording days to number of days ice cloud optical thickness recorded
1983	July 1	October 2	*94 : 82	N/A	N/A	N/A
1984	March 13	September 19	191 : 175	N/A	N/A	N/A
1985	March 14	September 30	201 : 174	N/A	N/A	N/A
1986	March 13	September 18	154 : 17	N/A	N/A	N/A
1987	March 13	September 9	181 : 41	N/A	N/A	N/A
1988	April 1	September 17	170 : 88	N/A	N/A	N/A
1989	March 18	September 30	197 : 101	N/A	N/A	N/A
1990	March 30	September 17	172 : 77	N/A	N/A	N/A
1991	March 20	September 30	195 : 83	N/A	N/A	N/A
1992	March 28	September 30	187 : 80	N/A	N/A	N/A
1993	March 14	September 19	190 : 34	N/A	N/A	N/A
1994	March 21	September 6	170 : 56	N/A	N/A	N/A
1995	March 30	September 27	182 : 64	N/A	N/A	N/A
1996	March 14	September 14	185 : 67	N/A	N/A	N/A
1997	March 30	September 29	184 : 65	N/A	N/A	N/A
1998	April 6	September 28	176 : 36	N/A	N/A	N/A
1999	March 15	September 9	179 : 35	N/A	N/A	N/A
2000	March 17	September 30	198 : 33	N/A	N/A	N/A
2001	March 31	September 26	180 : 45	N/A	N/A	N/A
2002	April 18	September 28	164 : 48	N/A	N/A	N/A
2003	March 17	September 9	177 : 63	N/A	N/A	N/A
2004	March 20	September 9	174 : 43	N/A	N/A	N/A
2005	March 31	September 28	182 : 46	N/A	N/A	N/A
2006	March 15	September 30	200 : 54	June 15	December 31	*200 : 132
2007	March 14	September 30	201 : 201	January 1	December 31	365 : 280
2008	March 13	June 30	*110 : 110	January 1	December 31	365 : 264
2009	N/A	N/A	N/A	January 1	December 31	365 : 244
2010	N/A	N/A	N/A	January 1	December 31	365 : 224
2011	N/A	N/A	N/A	N/A	N/A	N/A

\*Partial year of data available

### **4.3 Cosmic Ray Data**

For this study, Thule, Greenland neutron monitor data was extracted from the Bartol Research Institute website [Bartol Research Institute, 2012]. This website provided a comprehensive dataset for all required cosmic ray data from January 1, 1983 to August 31, 2011. Fully examined and corrected final datasets were available from the years 1983 to 1999 with preliminary data being over the duration from 2000 to 2011. Thorough annual data reviews that checked detector status and stability, barometer accuracy, pressure data, etc. were performed on final datasets. Preliminary data was described by the Bartol Research Institute as being subjected to “basic quality tests” where all major defects were corrected [Bartol Research Institute, 2012]. Data were reportedly not corrected for solar ground level enhancements.

#### **4.3.1 Manipulation of Cosmic Ray Data**

Due to the nature of the original data files, which contained several stations of data, hourly data readings for Thule station were extracted for all downloadable data from January 1, 1983 to August 31, 2011. The corrected datasets were used in all cases. All values were checked and unrealistic values were removed. From the hourly data, daily average values and yearly means were computed.

#### **4.3.2 Treatment of Cosmic Ray Data**

Thirty-three average daily values were found to be missing from the 1983-2011 dataset and two unrealistic data values were removed. The majority of missing data was from 1997, with 10 days from January 21 to 30 and 6 days from August 8 to 13 having no records. Two bad data values from January 20, 2005 and September 29, 1989 were found and removed. These data values were very large with 100x magnitude from normal values and were suspected to be incorrectly entered into the database.

For these missing and bad data, the Inuvik, Northwest Territories station was considered for data replacement. This station exists at 68.35 degrees latitude and -133.72 degrees longitude at an altitude of 21 m with a cutoff rigidity of 0.17. It was the closest station to Thule, in terms of latitude, altitude, cutoff rigidity and years of data coverage (1964 to

2001). The Thule, Greenland monitor station is much closer to the magnetic pole and it observes more northerly, along the Earth's spin axis and more perpendicular to the plane of the ecliptic, compared to the Inuvik station which gathers data from a more equatorial direction [Bartol Research Institute, 2012]. See Figure 4.3 which shows relative station locations and range of neutron monitor instrument viewing directions.

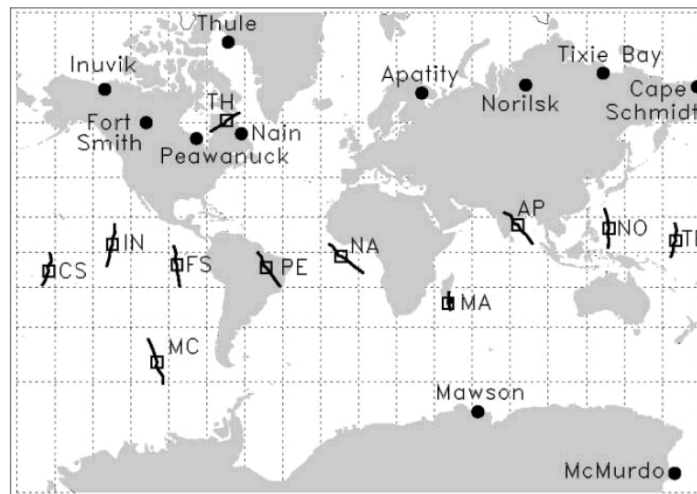


**Figure 4.3: Neutron monitor network. Nine of the high geographic latitude stations (filled circles) are able to view the “equatorial region after accounting for bending of particle trajectories in the geomagnetic field, while Thule and McMurdo (MC) generally view the northern and southern hemispheres, respectively” [Bieber et al., 2004].**

Existing equipment at the Thule station was updated in 2001, with addition of an 18NM64 neutron monitor, but all data was renormalization to pre-2001 values and posted at half the actual count rates. Although the Inuvik data values appear to have higher cosmic ray counts in the archives, due to this reporting difference, shown in Figure 4.3, actual count rates were much lower than those at Thule. See Figure 4.4 for functions and simulations derived from recorded data indicating how count rate varies with cutoff rigidities for neutron monitor stations around the world.

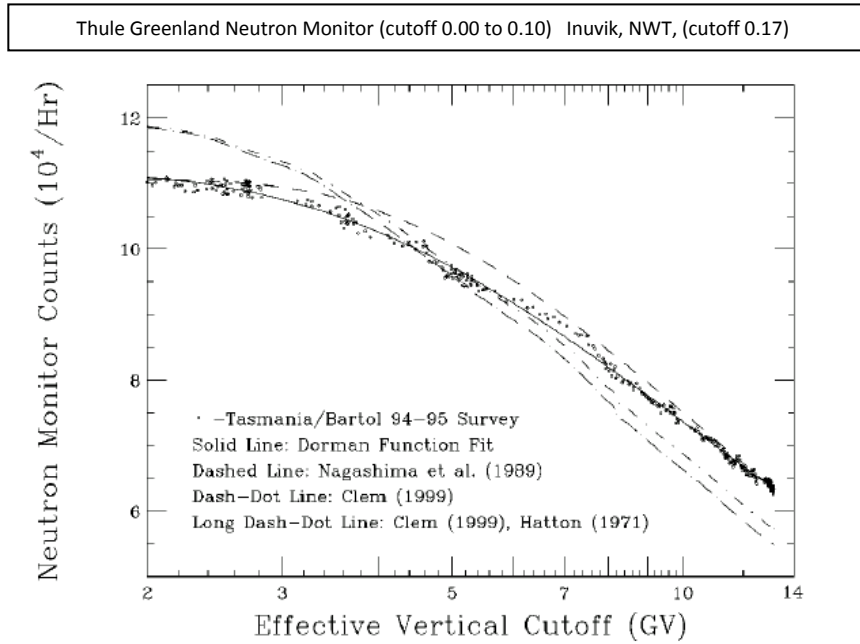


**Figure 4.4. “Count rate recorded during the Tasmania-Bartol 1994–1995 latitude survey compared with various derived count rates” [from Clem and Dorman, 2000, with permission].**

There is an indication that a north-south anisotropy exists between the databases that could not be corrected using only two stations. The Inuvik station is subjected to a more intense diurnal variation than at Thule. For these reasons, the Inuvik data was not used to replace missing or bad data in the Thule dataset.

Percentage variances for all previous datasets, were computed for monthly and annual mean data. This was done as follows:

$$\frac{(\text{Dataset Value} - \text{Dataset Mean})}{\text{Dataset Mean}} * 100 \tag{5.1}$$

This computation allowed for different datasets to be more easily compared in a chart and the variances within datasets to be viewed.

## CHAPTER 5: RESULTS AND DATA ANALYSIS

This chapter presents a number of charts and correlations that apply the previously-described cosmic ray, ice cloud optical thickness and total column ozone time series datasets. These comparisons will be done to prove if the compiled data can predict that cosmic rays are able to influence either cloud microphysics or persistence and their overall effect on total column ozone. All plots presented here include cosmic ray intensity data from the Thule, Greenland neutron monitor station and other satellite-based ice cloud and total column ozone data from a region no greater than 200 km from the Thule, Greenland station, as described in Chapter 4. All positions are with respect to the World Geodetic System 84 datum. Data comparisons to time-series data plots by Lu [2009] and Harris et al. [2010] will be shown using the regional Arctic databases. This work will help to gain a clearer understanding of how the datasets vary with time and identify any possible similarities or statistically significant relationships between them.

### 5.1 Cosmic Ray and Polar Ice Cloud Comparisons

It is important to initially compare atmospheric ionization due to incoming cosmic rays to both the optical thickness and persistence of ice clouds. Periods where both of these variables are high should represent the time frames over which chemical reactions would be enhanced on ice cloud particle surfaces. Any strong correlations would help predict if atmospheric ionization plays a role in CCN or polar ice cloud generation or persistence. Figure 5.1 shows the ISCCP Monthly Ice Cloud Tau mean values from July 1983 to June 2008.

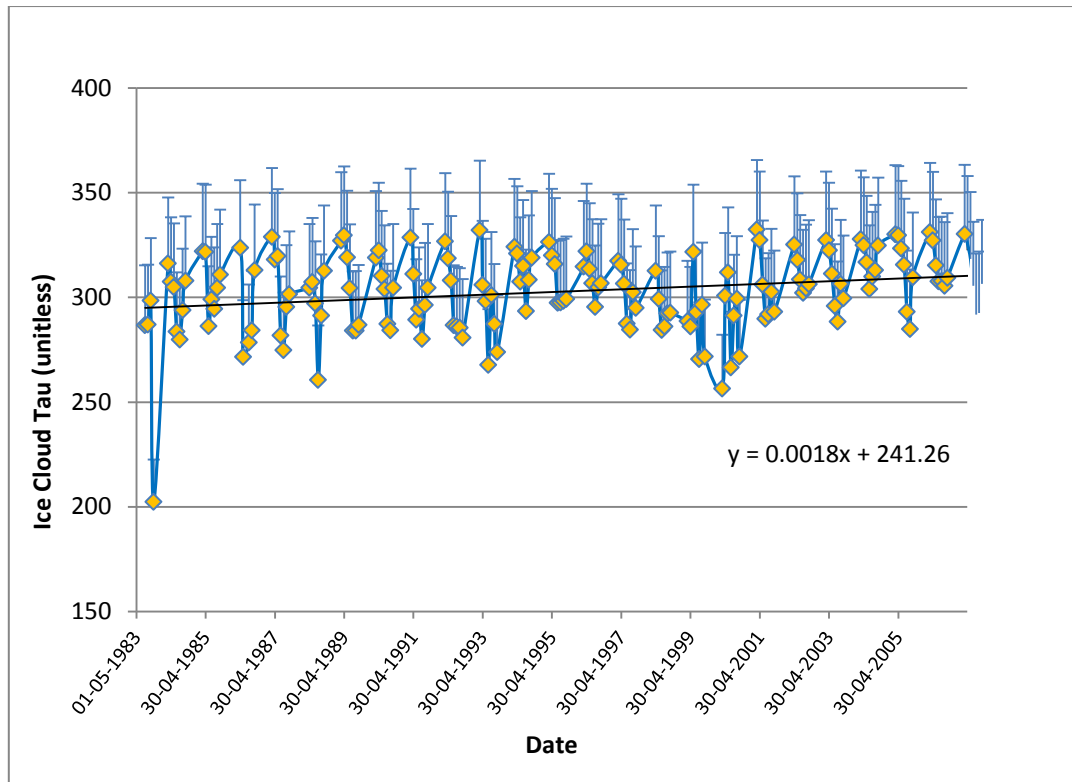


**Figure 5.1: Ice cloud tau monthly mean data from the ISCCP database from July 1983 to June 2008.**

Figure 5.1 shows a general increase in the monthly average ice cloud tau over the 23-year time period from July 1983 to September 2006, as indicated by the linear trend. The error bars represent a 10 percent underestimate of the project data compared to ground station measurements for the Arctic, based on Rossow [1999] and described in Section 3.2.1.1 “Documented Errors in ISCCP Measurements”. To compare this data to cosmic ray data, Figures 5.2 and 5.3 examine the original data and 5-point moving average curves applied to both datasets to determine any trends.

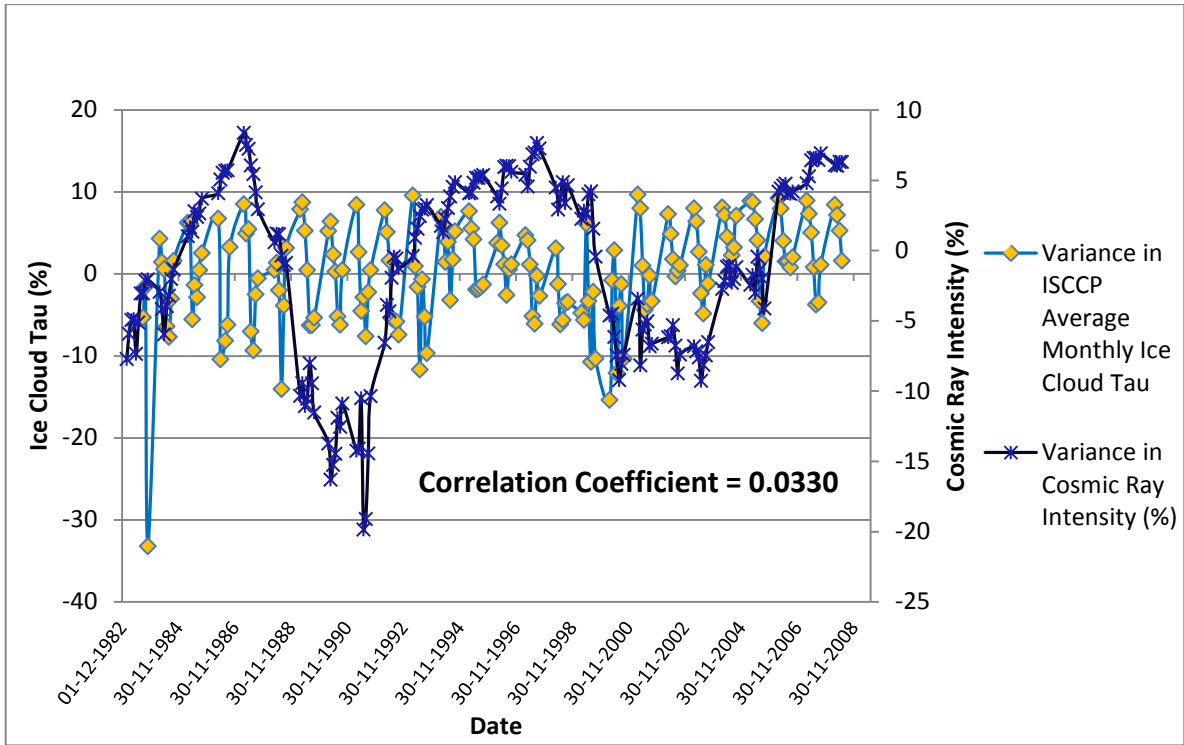


Figure 5.2: Percentage variance of cosmic ray intensity plotted against the ISCCP ice cloud tau monthly mean values from July 1983 to June 2008.

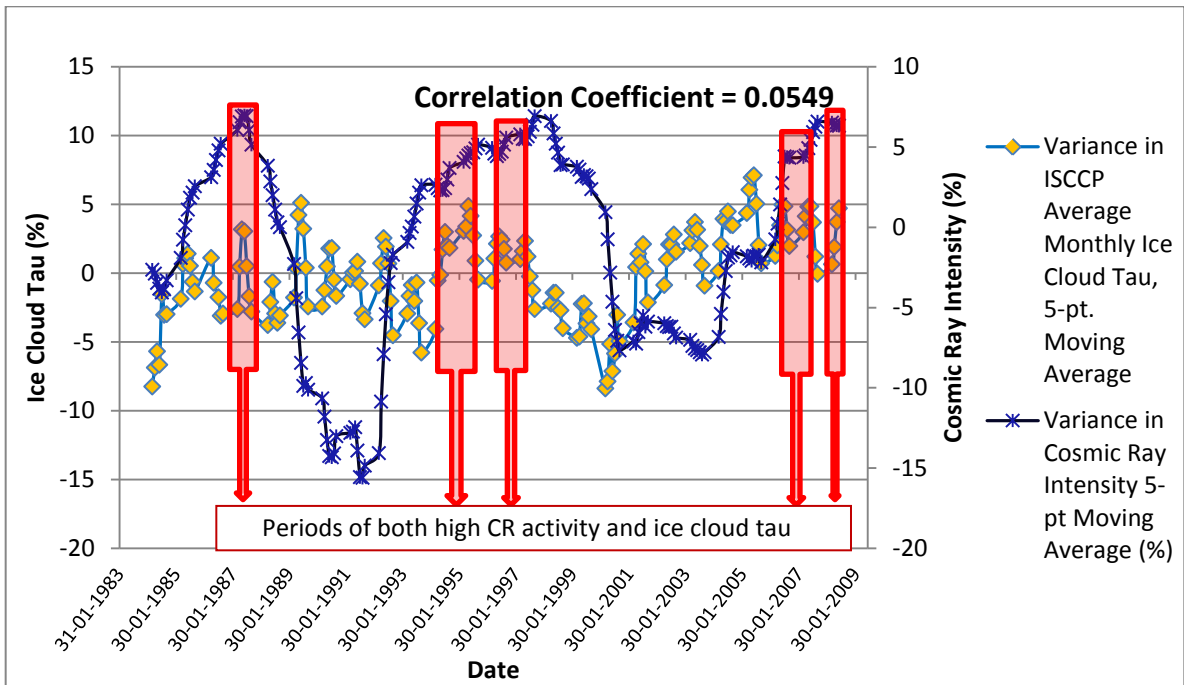
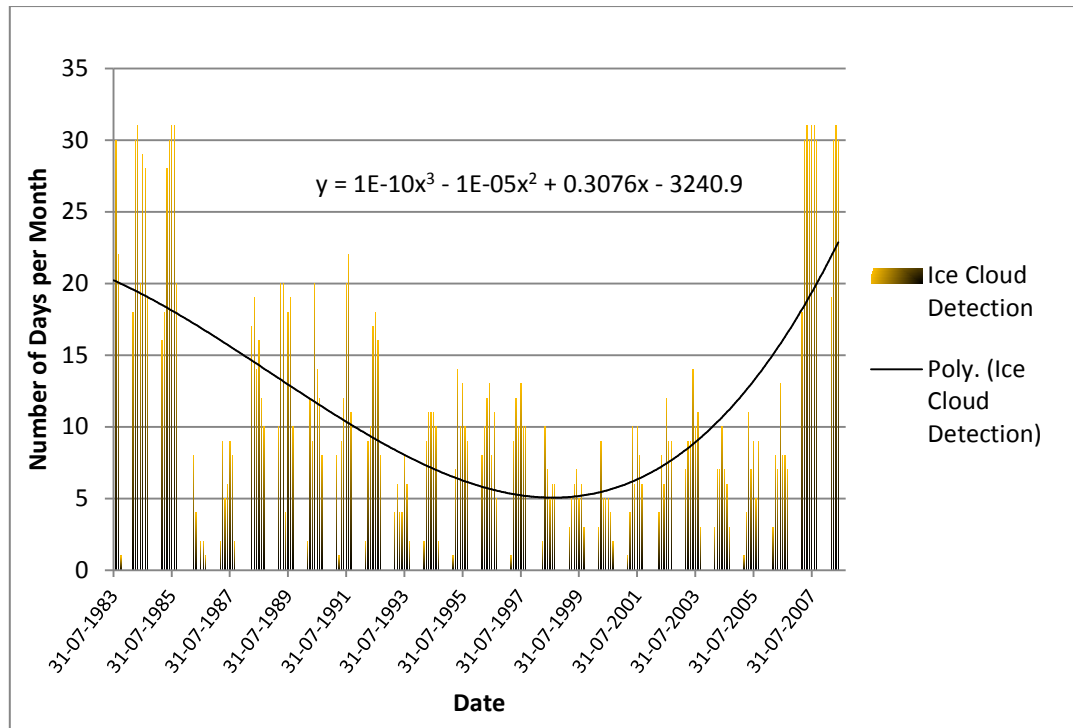


Figure 5.3. Five-point moving averages of percentage variances of both cosmic ray intensity and ISCCP ice cloud tau monthly mean values from July 1983 to June 2008.

Figures 5.2 and 5.3 appear to show similarities in the trends of both cosmic ray and ice cloud tau datasets, but the frequencies of the datasets are different and correlations between the datasets were quite low. The percentage variance calculations of cosmic ray and ISCCP ice cloud tau data only conform with a correlation coefficient of 0.03. The 5-point moving averages for these datasets were developed to extract any obvious trends in the data (Figure 5.3). These results produced a slightly higher correlation of 0.05, resulting in an improvement of approximately 2.2 percent. The lack of strength in these results is discouraging and correlations are not considered significant by statistical means.

Periods when both heightened cosmic ray intensity and ice cloud tau exist can be estimated from Figure 5.3. These occur in mid-1987, throughout the year in 1995, fall 1996 to spring 1997, winter to spring of 2007 and summer of 2008. These time frames will be analyzed against the total column ozone data.

To examine the cosmic ray-ice cloud relationship from another perspective, the number of days per month that ice clouds were detected was computed using the ISCCP data. In the study by Harris [2010], polar stratospheric cloud persistence was cited as playing a critical role in predicting ozone loss. This is displayed in Figure 5.4.



**Figure 5.4: The calculated number of days per month, from 1983 to 2008, that ice clouds were detected based on the ice cloud tau values from the ISCCP database.**

In Figure 5.4, a 3<sup>rd</sup>-order polynomial trend line and equation are displayed on the chart. This trend line was chosen from its visual match to the data compared to other basic trend fitting algorithms. Over the years studied, it suggests a possible cycling of the number of days per month ice clouds were detected over northern Greenland. The cycle indicates that there was an increase in cloud cover over the years of 1983 to 1985 and again from 2007 to 2008. The persistence of ice clouds for these years would produce an increase in local albedo. The microphysical ice surfaces within the clouds would cause incident solar radiation to be reflected back to the upper atmosphere and into space. During these years, a cooling of the Earth would result in the region where these ice clouds existed. Although this is a reasonable observation, longer time-frame datasets would be important to confirm any actual cycles in monthly and yearly ice cloud presence and persistence. Lack of data over the winter months complicates any conclusions drawn from these initial observations.

The persistence of polar ice clouds for the year of 2007 (in Figure 5.4) does correspond to a detected increase in cosmic ray activity during that same year (from Figure 5.2) but the cosmic ray peaks in 1987 and 1997 are not obviously related to the ice cloud persistence data. There is only a subtle rise in cosmic ray activity for 1983 that corresponds to the peak in number of days of ice cloud detection from the ISCCP data.

A comparison of these data against cosmic ray intensity as measured from the Thule, Greenland neutron monitor station is shown in Figure 5.5.

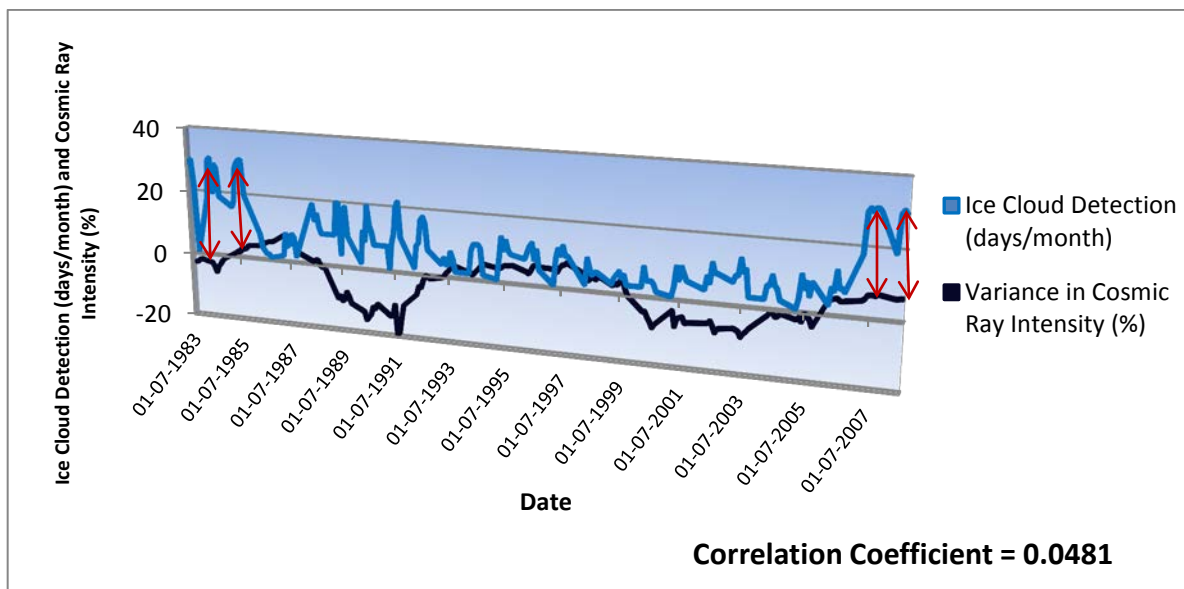


**Figure 5.5: Percentage variance of cosmic ray intensity and ISCCP Ice Cloud Detection in number of days per month. Peaks in ice cloud detection are indicated by red arrows.**

From Figure 5.5, the dates corresponding to observable peaks in ice cloud detection are indicated by red arrows in the plot. Any possible cause-effect relationship between atmospheric ionization and ice cloud cover, measured as days per month of ice cloud detection, is not supported by this data. The correlation value computed was only 0.04 between the datasets.

Compared to the ISCCP product, improved satellite detection of cloud properties from Cloudsat, CALIPSO, and MODIS observations allowed for more direct measurements in the

development of the DARDAR modeled cloud phase and microphysical parameters by ICARE. Due to this, although the dataset is of shorter duration (June 15, 2006 to December 28, 2010), and does not include computations based on stratospheric clouds, it was worth examining in more detail. These same comparisons (to Figures 5.2, 5.3 and 5.5) using the DARDAR data were proposed to result in less ambiguous conclusions. The DARDAR data was initially compared against the ISCCP ice cloud tau data to determine how similar the databases were (see Figure 5.6). For purposes of discussion, the ISCCP and DARDAR data will be referred to as ice cloud tau and ice cloud optical thickness, respectively, which are the original terminology used for these parameters in each of the projects. Both sets of parameters represent ice cloud tau, provide an indication of ice cloud optical density, and are unitless, although the values have very different ranges due to differences in the modeling approaches. Ice cloud tau and optical thickness are both derived from the extinction variable in the models (see the section on ISCCP and DARDAR Cloud Data Descriptions in Chapter 3).

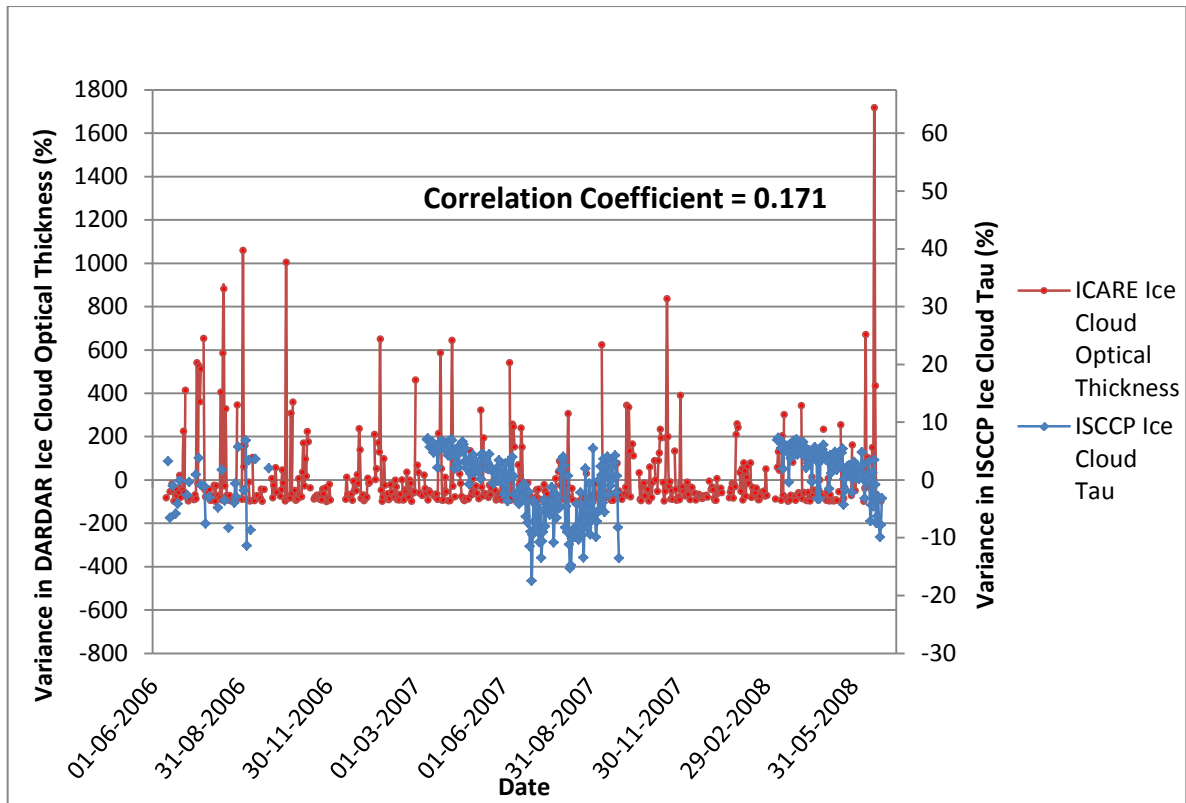


**Figure 5.6. Percentage variances of ice cloud tau and DARDAR ice cloud optical thickness over the period of dataset overlap between June 2006 and June 2008.**

The datasets shown in Figure 5.6, indicate a low correlation coefficient of 0.17 between them over the months (spring to fall) in which the data overlaps. This supports a disparity between the computation of ice cloud microphysical tau / optical thickness as provided by these two projects.

Similar to the plot created in Figure 5.1, the DARDAR data is shown in Figure 5.7.

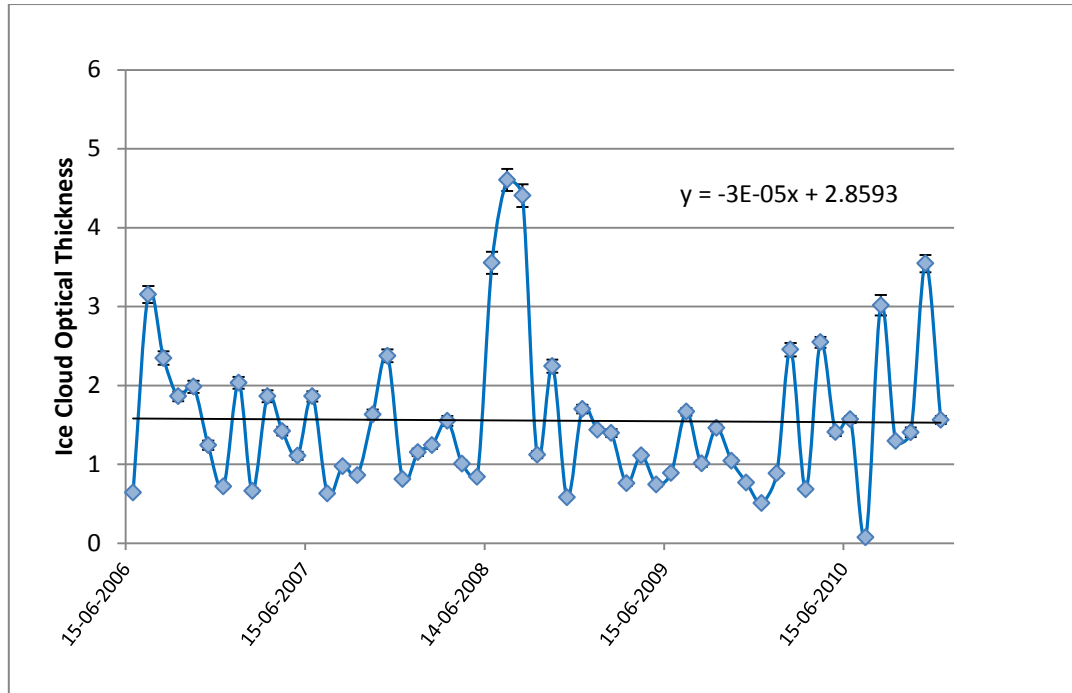


**Figure 5.7: Ice cloud optical thickness monthly mean from the ICARE DARDAR database from June 2006 to December 2010.**

In Figure 5.7, the error bars indicate the computed error in ice cloud optical thickness based on the model results from the input datasets. Within this plot, the change in ice cloud optical thickness, over the years of study and from the linear trend, are slightly decreasing and do not show the same trend as the ISCCP data depicted in Figure 5.1. An increasing trend can be observed from the Fall of 2009 through the year 2010, but additional data, past 2010, would be needed to confirm this assertion.

The following Figures 5.8 to 5.11 for the date range from 2006 to 2010 for the ICARE DARDAR cloud data, are similar to the plots from Figures 5.2 to 5.5 previously shown for the ISCCP dataset.

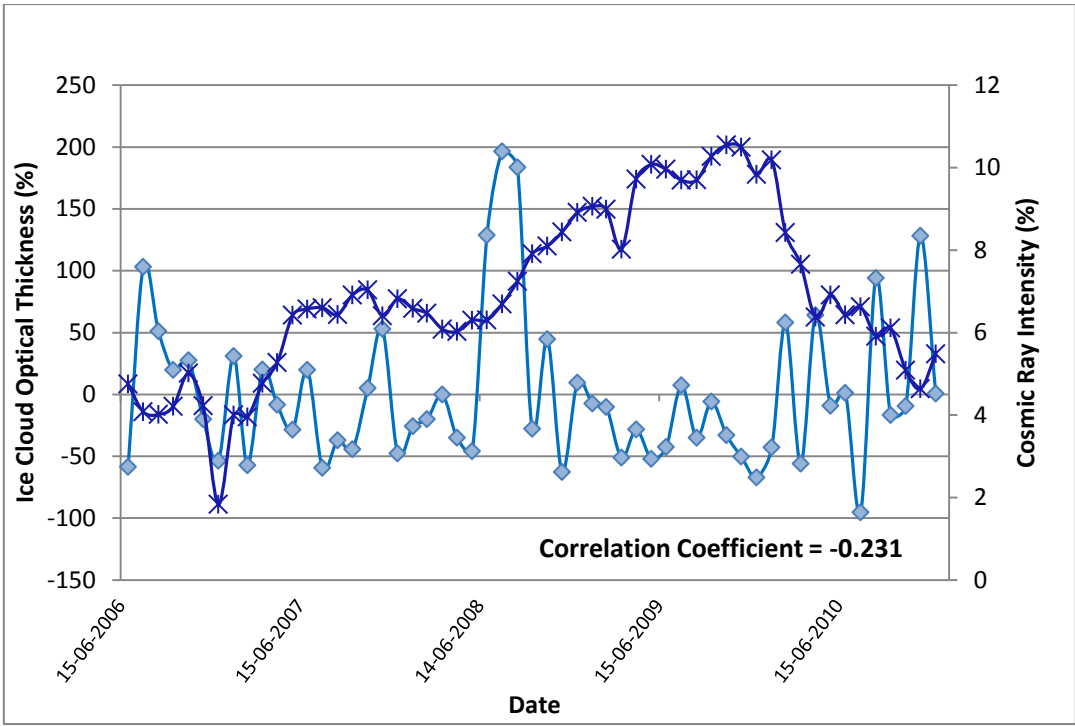


**Figure 5.8: Percentage variance monthly mean values of cosmic ray intensity and DARDAR ice cloud optical thickness from June 2006 to December 2010.**

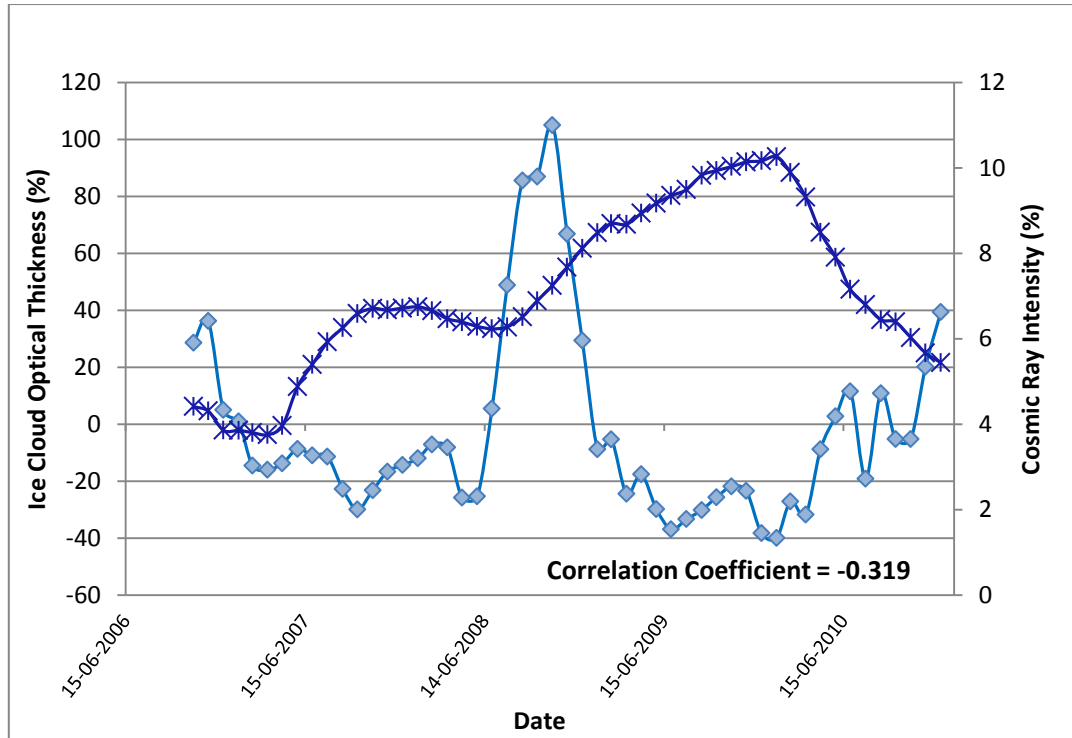


**Figure 5.9: Five-point moving averages of percentage variance of both cosmic ray intensity and the DARDAR ice cloud optical thickness monthly mean values from June 2006 to December 2010.**

The relationship in both Figures 5.8 and 5.9, displaying the original monthly mean and 5-point moving average correlation coefficients, are fairly strong negative ones. To determine if these results are significant, we can calculate a statistical two-tailed test. For this test, the critical value of  $t$  is computed as follows:

$$t = r \sqrt{\frac{n-2}{1-r^2}} \quad (6.1)$$

where  $t$  is the two-tailed result,  $r$  is the correlation coefficient for the datasets, and  $n$  is the number of samples being compared.

In Figure 5.8,  $n-2$  is represented by 53 values and in Figure 5.9, this number is 49. Given this, the critical values of  $t$  from equation 6.1 are -1.728 and -2.35, respectively.

Comparing these values to statistical tables, the t-test values are 2.01 and 2.68 for 50 degrees of freedom and 2.00 and 2.67 for 55 degrees of freedom at levels of confidence 0.05 and 0.01, respectively, for the two-tailed test results. The correlation in Figure 5.8 falls short of the two-tailed test statistical values. The 5-point moving average results are significant for the 0.05 level of confidence range. Although this result does not agree with the hypothesis that ice cloud optical thickness should increase as a result of increased atmospheric ionization, it represents a single case of a computed significant statistical inverse relationship between these two datasets.

Examining the original data from Figure 5.8 further, there is a unusual peak in the ice cloud optical thickness data from June to August 2008. This peak is a 29.9 percent increase from the peak identified for the monthly mean from November 2010. This increase is not easily explained, but the year does correspond to the visible peak in the ISCCP ice cloud tau data from Figure 5.3 and ice cloud persistence data from Figures 5.4 and 5.5.

It is additionally important to review the persistence of ice clouds as derived from ICARE, especially since the DARDAR dataset is continual over the winter months. Figure 5.10 illustrates the number of days per month that ice clouds were detected based on the ice cloud optical thickness variable.

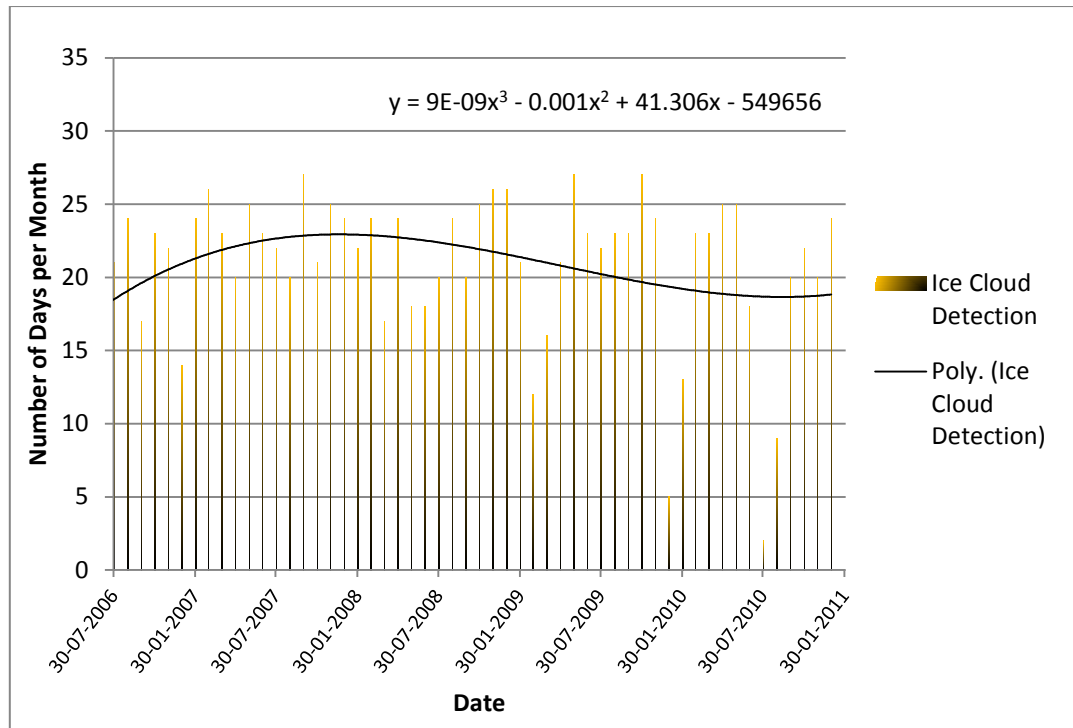


**Figure 5.10: Number of days per month (2006 to 2011) that ice clouds were detected based on the ice cloud optical thickness parameter from the ICARE DARDAR database.**

Similar to Figure 5.4, the 3<sup>rd</sup>-order polynomial trend line and equation were computed for this dataset and in are displayed on the chart in Figure 5.10. This trend line shows a general decrease in cloud cover persistence from 2008 to 2011. Additionally, there is a lack of repeatable or predictable behavior of cloud persistence during these years of detections over Thule, Greenland. For example, the months of December 2009 and July 2010 indicate the lowest number of detection days ( $\leq 5$ ) while February 2007, September 2007, May 2009 and October 2009 all have greater than 25 days of ice cloud detection over northern Greenland. These years of maximum number of days of ice clouds do show some correspondence to the peaks in the cosmic ray curves (see the red arrow markings in Figure 5.11).

Although the total curve comparison only results in a correlation coefficient of 0.07, the curve maximums indicated by red arrows in Figure 5.11, especially in the cases of September 2007, May 2009 and October 2009, do correspond to the start and end of the

heightened atmospheric ionization, related to cosmic ray activity. The lows and general variations in cloud persistence in this figure, cannot be explained by the changes in cosmic ray flux.

The low in ice cloud persistence for the month of July 2010 (Figure 5.10) occurs at the same time of decreasing cosmic ray activity as viewed in Figure 5.9 but does not correspond to a cosmic ray activity minimum. The low ice cloud persistence value recorded for December 2009 does not relate to any minimums in incident cosmic rays.

From Figure 5.10, there is an indication of a possible cycling of data over the years 2009 and 2010 where cloud persistence is lower in the winter and increases over the year. The values that do not correspond in these data comparisons could possibly be explained by dates of heightened solar activity over these periods, which has not been added to these data analyses. There is obviously more complexity in the data that is not accounted for in this analysis. To compare this data to cosmic ray intensity data from the Thule, Greenland neutron monitor, Figure 5.11 was created.

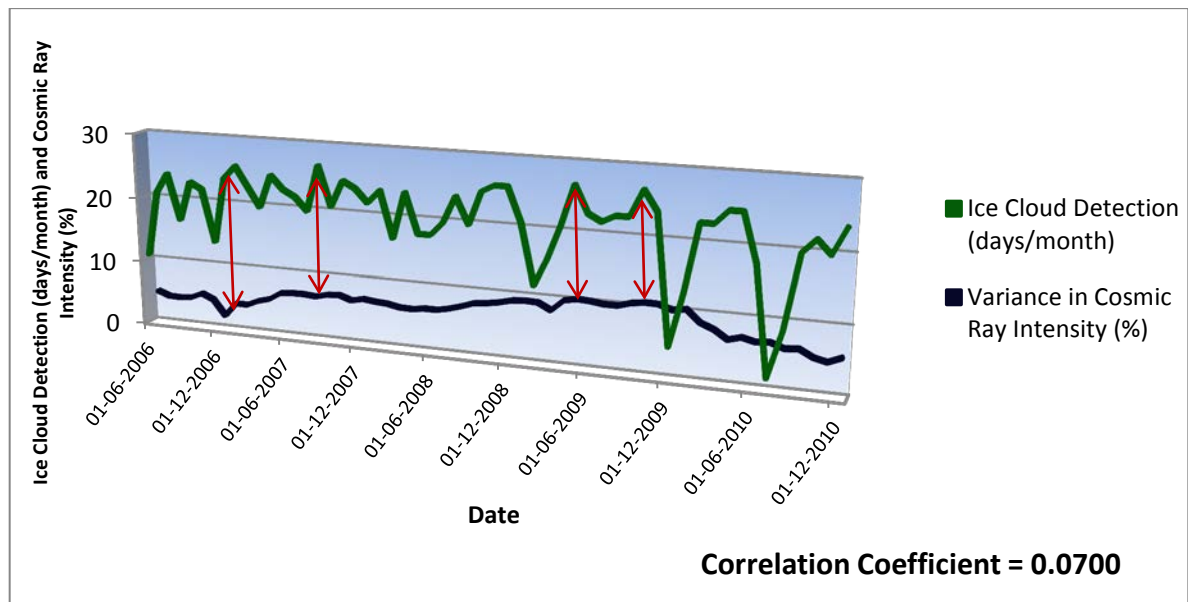


**Figure 5.11: Percentage variance of cosmic ray intensity plotted against ice cloud detection from the DARDAR ICARE project in number of days per month.**

The red arrows in this figure indicate the greatest peaks in the persistence of ice clouds and how they correspond to the annual cycles of atmospheric ionization due to cosmic ray activity.

Although it would be valuable to compare true ice cloud volumes, calculations of this parameter could not be determined from the data due to the nature of satellite sampling. There was lack of a spatial component as the satellites offered only single pixel sampling for the available daily observations over the area of interest.

## **5.2 Cosmic Ray and Total Column Ozone Comparisons**

The next relationships to be examined includes atmospheric ionization from cosmic ray response and total column ozone values. These relationships are predicted to show reduction in ozone following periods of increased cosmic ray activity. The first comparisons use the TOMS-OMI-SBUV collection of data from 1983 to 2011. See Figures 5.12 to 5.15 which provide the original total ozone annual mean and October monthly mean plots and the computed 3-point moving average results.

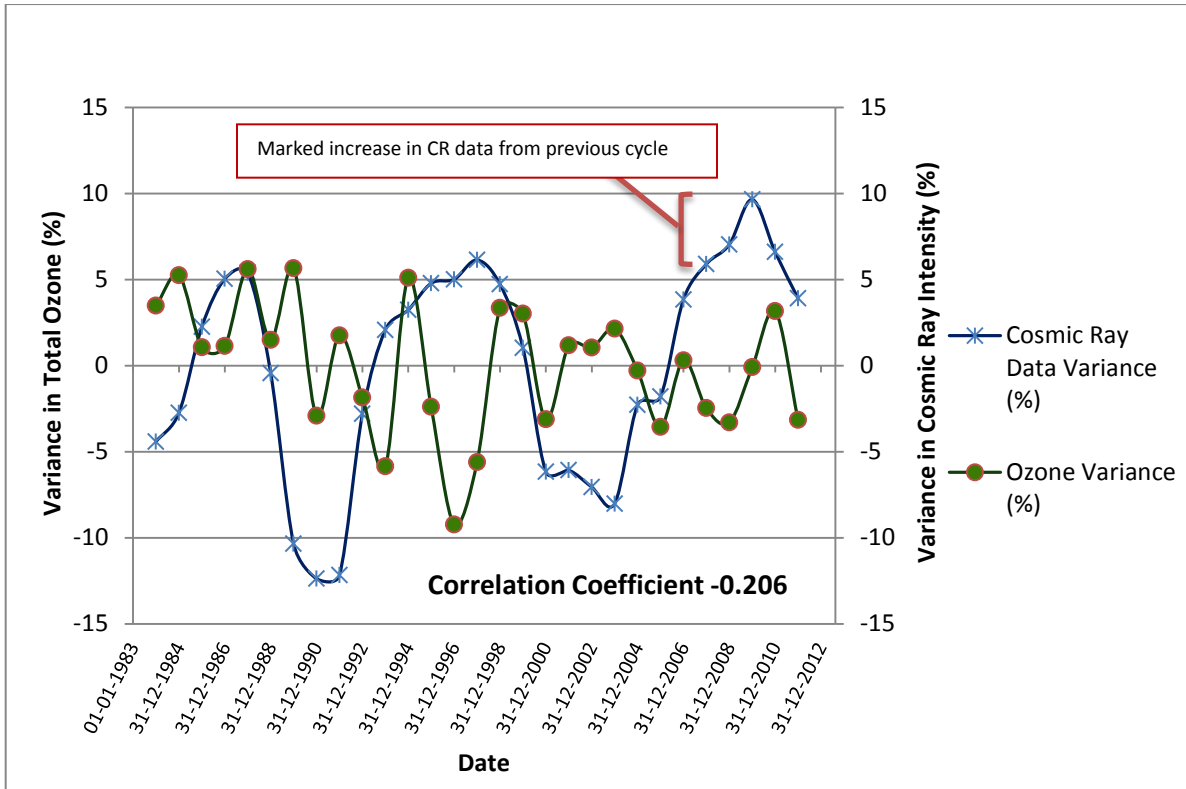


**Figure 5.12: Percentage variations of observed cosmic ray intensity and annual mean total ozone for the period of 1983 to 2011.**

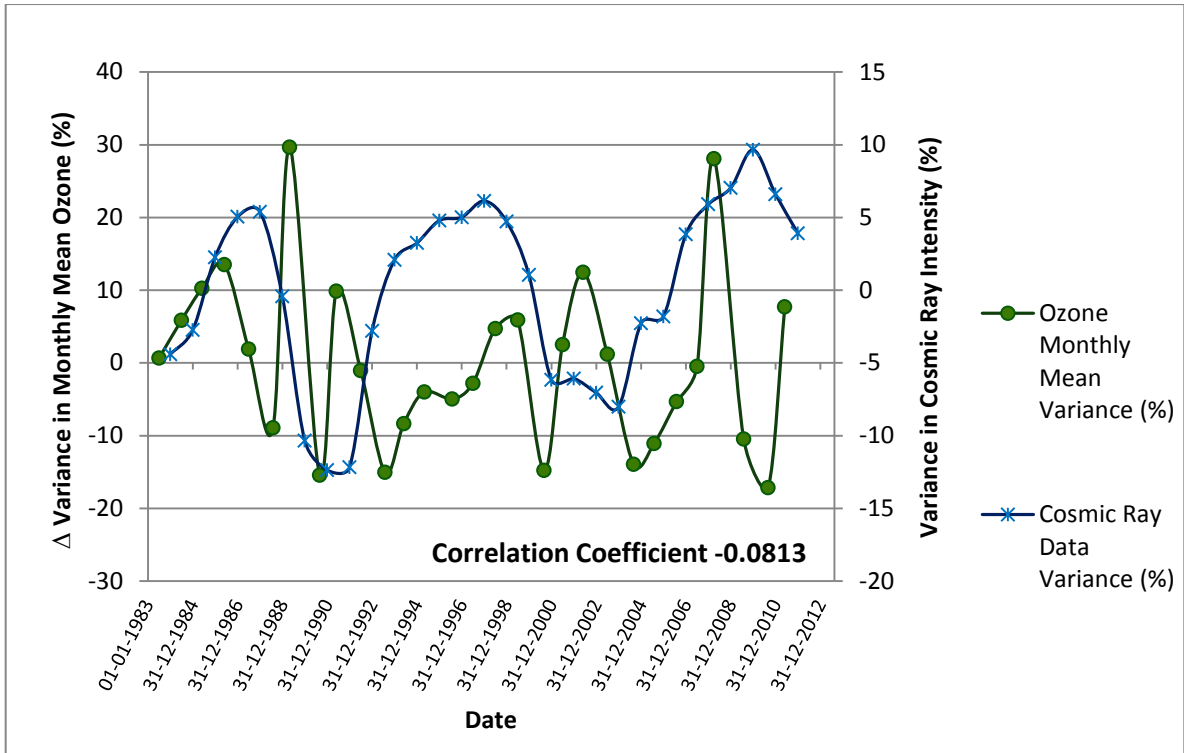


**Figure 5.13: Percentage variations of observed cosmic ray intensity and March to August month of maximum loss expressed as monthly mean total ozone for the period of 1983 to 2011.**

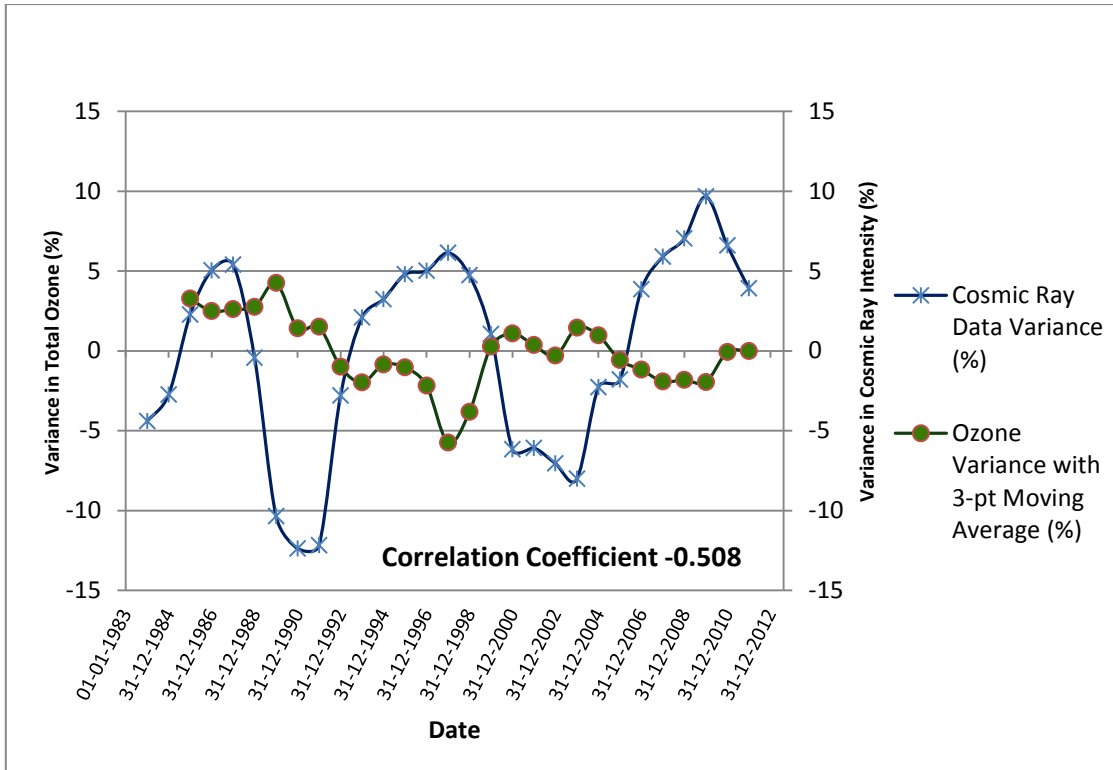


**Figure 5.14: Percentage variations of observed cosmic ray intensity and annual mean total ozone 3-point moving average for the period of 1983 to 2011.**

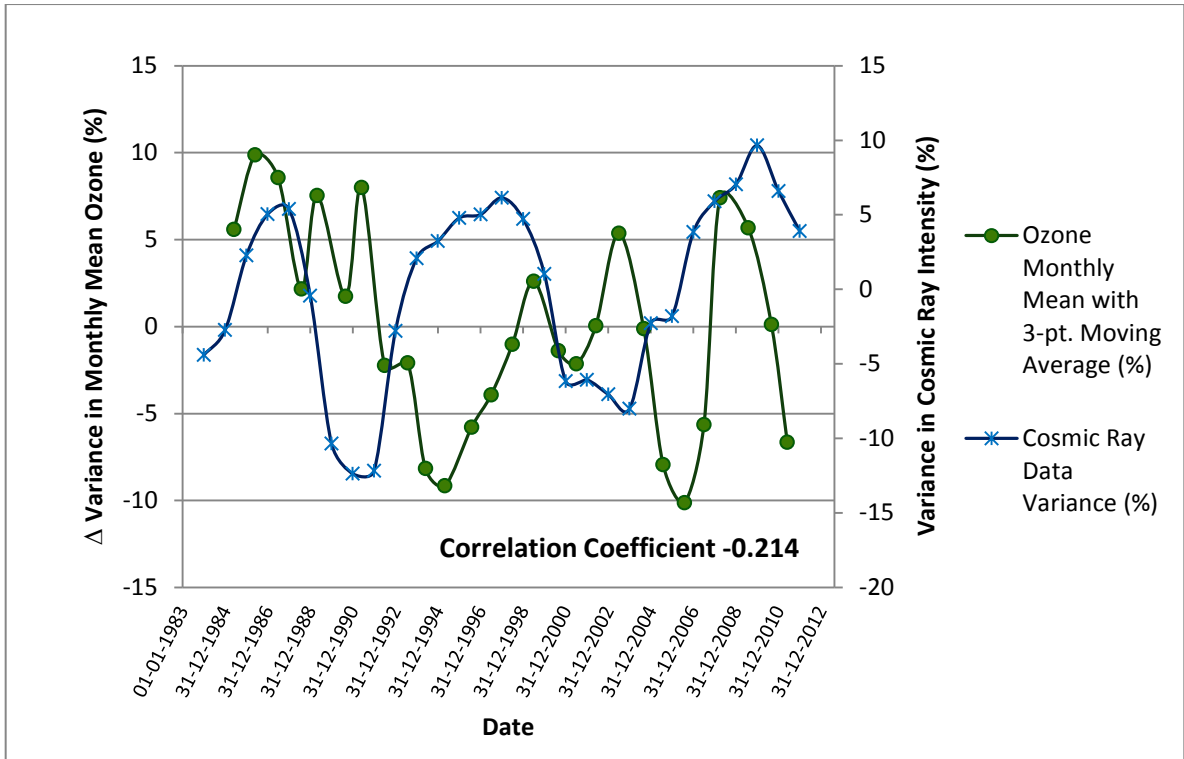


**Figure 5.15: Percentage variations of observed cosmic ray intensity and March to August month of maximum loss expressed as monthly mean total ozone 3-point moving average for the period of 1983 to 2011.**

Figures 5.12 and 5.14 compare to the work by Lu [2009] (copy of Figure 2.7 below) as they represent annual mean total ozone values.

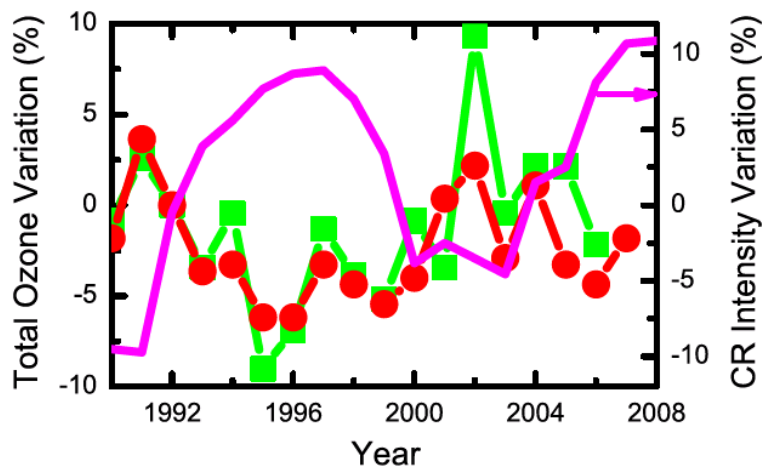


**Figure 2.7: Percentage variations of cosmic ray intensity and annual Antarctic mean total ozone data from the two neutron monitor stations [from Lu, 2009, with permission].**

Figures 5.13 and 5.15 were created to replicate the findings from Lu [2009] (copy of Figure 2.8 below) which examined the months of greatest ozone depletion observed from September through November per annum in the Antarctic. Here, we use the annual maximum loss months, existing for one of the months between March to August.

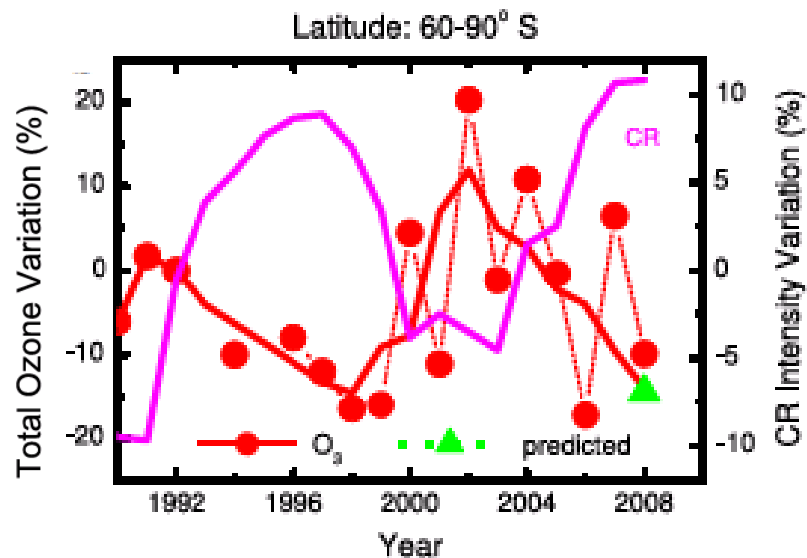


**Figure 2.8: Percentage variations of observed cosmic ray intensity, averaged from three neutron monitor stations, and monthly average zonal mean total ozone in October in the Antarctic [from Lu, 2009, with permission].**

Lu [2009] focused on the greatest periods of ozone loss during the months of September through November and he stated that these were the months that best represent the observed ozone hole in the Antarctic (Figure 2.8). These should be the months of March to May in the Arctic if the same type of response occurs in spring in this region, but instead, the months of greatest loss were found to range from March to August for the datasets analyzed. The greatest losses in the northern hemisphere data occur in either May or June over the entire dataset (see Figure 5.16). An exception is seen in 1994 where the ozone layer was considerably depleted in August. The months of greatest seasonal ozone depletion also relate to controlling temperatures in the stratosphere. This may be one significant source of difference between the Arctic versus the Antarctic.

The years of greatest month-to-month ozone loss for the TOMS-OMI-SBUV dataset were 1994, 1997, 2002 and 2007 (Figure 5.16). These are represented by greater than 15% decrease from the previous monthly loss values for the year. Other years with months of slightly smaller negative values include 1985, 1986, 1999 and 2003. The years with the largest gains or months of ozone recovery are 1984, 1987, 1990, 1997 and 2006.

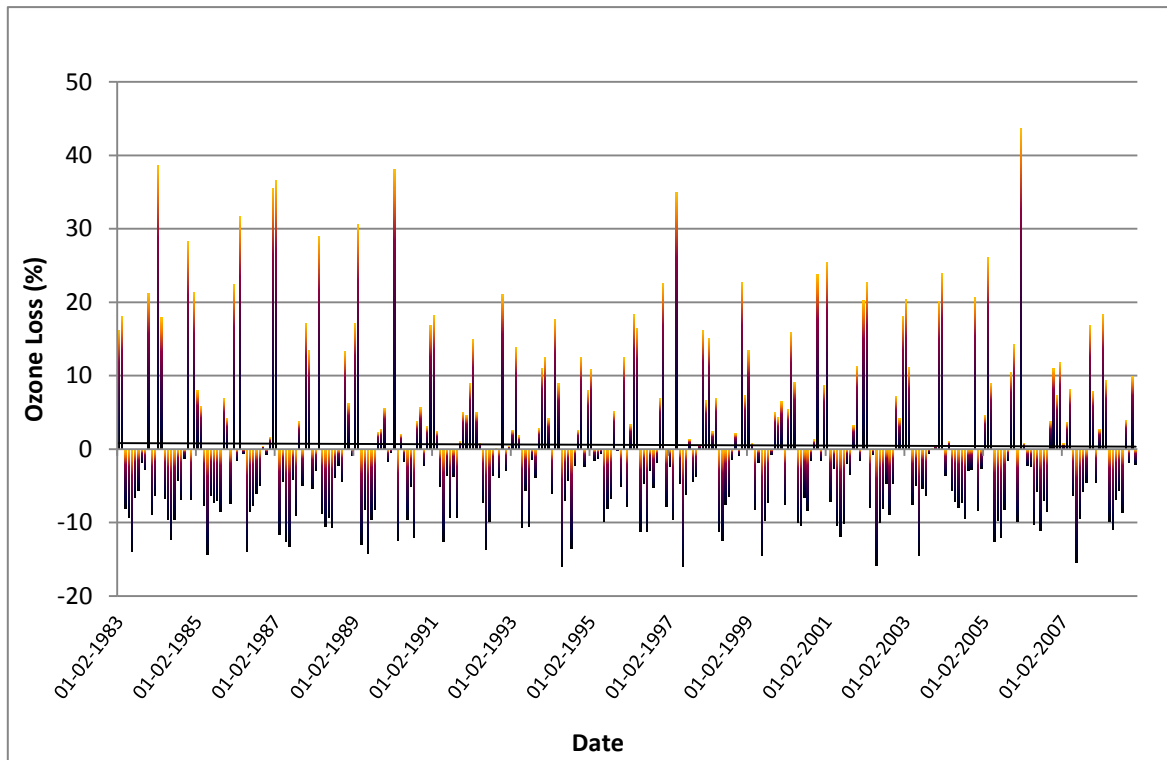


**Figure 5.16: Monthly ozone loss computed as a percent from the TEMIS multi-sensor dataset, representing the time frame from 1983 to 2008.**

Both visual similarities and differences can be observed between the charts from Figures 5.13 and 5.15 compared to the 2009 study by Lu [2009] (Figure 2.7). These figures capture the monthly mean values extracted from the TOMS-OMI-SBUV dataset for the month of greatest loss to maximize the number of years for comparison. Although the points are very spurious in Figure 5.13, especially over the yearly ranges from 1987 to 1991 and again from 2007 to 2011, the 3-point moving average plot in Figure 5.15 does help to resolve some trends. In Figure 5.15, the ozone reaches its first low point earlier in the heightened cosmic ray cycle. This occurs in 1994 rather than in 1998 for Lu [2009] from

Figure 2.8. Both averaged versions of the datasets peak within one year of each other (2002 versus 2003), but where Lu [2009] shows a general decreasing trend after this peak, the 3-point moving average case, from Figure 5.15, cycles more strongly. In Figure 5.15, there is a visually strong trend in the ozone data that is a reverse polarity from the cosmic ray data from the beginning of 1989 to 1999, but the overall correlation was only -0.21 for the entire data range.

Comparing the two annual mean ozone results in Figure 2.7 from Lu [2009] and Figure 5.14, they do show a visual polarity reversal to the cosmic ray intensity displayed in both images. The publication by Lu [2009] expressed this correlation in terms of a best-fit line, but did not reveal the correlation coefficients between the datasets. For the 3-point moving average result in Figure 5.14, a negative correlation of -0.51 was computed. The plot of cosmic ray intensity and spring to summer seasonal monthly mean total ozone, from Figure 5.13, reveals greater variance compared to the annual mean total ozone results in Figure 5.12, and resolves a correlation to the cosmic ray dataset of -0.081. These two results, as they compare to the cosmic ray data are very different. From this, it is important to determine if these results are statistically significant.

Testing the case where the correlation coefficient is -0.51 and the number of samples is 27, gives a t value of -2.95. Comparing this value to the statistical tables, the two-tailed result for 25 degrees of freedom is 2.06 (-2.06) and 2.79 (-2.79) at 0.05 and 0.01 Level of Confidence, respectively. Since -2.95 is less than -2.79, we can reject the null hypothesis and determine that -0.51 is a significant correlation for the annual total ozone and cosmic ray intensity datasets in the case where the 3-point moving average was obtained. The correlation coefficient of -0.081 is too low to be a statistically significant result.

Considering this significant negative correlation result of -0.51, it is important to discuss any cause-effect relationship between the datasets of cosmic ray intensity and ozone data. In general, a correlation of greater than  $\pm 0.70$  may lead to a decision that a causal

nature between properties can be inferred. In nature, this value may be considered lower than 0.7 due to complexity of other interfering factors or measurement error. There may be different interpretations of this value, but from this data alone, a true causal nature cannot be implied. If another dataset comparison could be added to this correlation, to help solve the puzzle, it is possible that a causal nature of the theory would be closer to being supported. Stronger correlations may exist if the datasets were broken into smaller time frames or considered different data frequencies. This study resolved to focus on the datasets with the greatest duration to reveal any long-term data trends and attempted to not over-process the original data.

The main differences between the data analysis in this study compared to Lu [2009] are factors of differing locals, regional extent for data retrievals, sources of data and length of time series scales. In this study, the Arctic data focused on neutron monitor ground-based counts from the Thule, Greenland station, at 76.5396N latitude and 68.7759W longitude, while Lu [2009] averaged neutron monitor values from the McMurdo, Thule and Newark stations to obtain his resultant cosmic ray intensity curves. For the atmospheric total ozone data, a maximum distance of any satellite data retrieval from the Thule station was 200 km while Lu used a latitude band from 60 and 90 degrees south for the monthly mean data series and data from two individual Antarctic stations for the annual mean data. In Lu's ozone October monthly mean plot (Figure 2.8), TOMS and OMI data was used, while in this study, additional SBUV data was added to fill total ozone data gaps between 1994 and 1996. Lu [2009] did not reveal how data overlap or missing data values were handled between the datasets. For the annual mean total ozone plot in Figure 2.7, Antarctic ground-based ozone data from the Faraday/Vernadsky and Halley stations were used while satellite observations from TOMS-OMI-SBUV were shown in Figure 5.14. This study extended the 1990 to 2008 data range from Lu [2009] to incorporate a new range from 1983 to 2011. Given these differences, the charted results, especially in the 3-point moving average total annual ozone case (Figure 5.14) compared to Lu's annual mean ozone plot in Figure 2.7, are surprisingly similar from 1991 to 2008. Although the original

time series of ozone data, from Figure 5.12, showed much greater relative variability, the averaged curve (Figure 5.14) is significantly smoother. Comparing the moving-average results, the main differences between these charts are stronger peaks (1995 and 2002) and greater variation between successive points. The main increase in the curve from 1999 to 2003 from Figure 2.7 lags similar movement in Figure 5.14 which exhibits this change over a shorter date range from 1997 to 2001.

It is critical to examine the relationship between cosmic ray intensity and how ozone may respond in terms of seasonal depletion of ozone, from spring to fall. This relationship is shown in Figure 5.17 where annual minimums (fall) are subtracted from annual maximums (spring). The computed total ozone values, from which the percentage variances were established, are from the TOMS-OMI-SBUV satellite-based measurements shown on the left side of Table 4.1. The highlighted values, indicated by red boxes in the plot, illustrate the years of the largest ozone column loss with original values of -43.269 (1989) and -44.231 DU (2002).

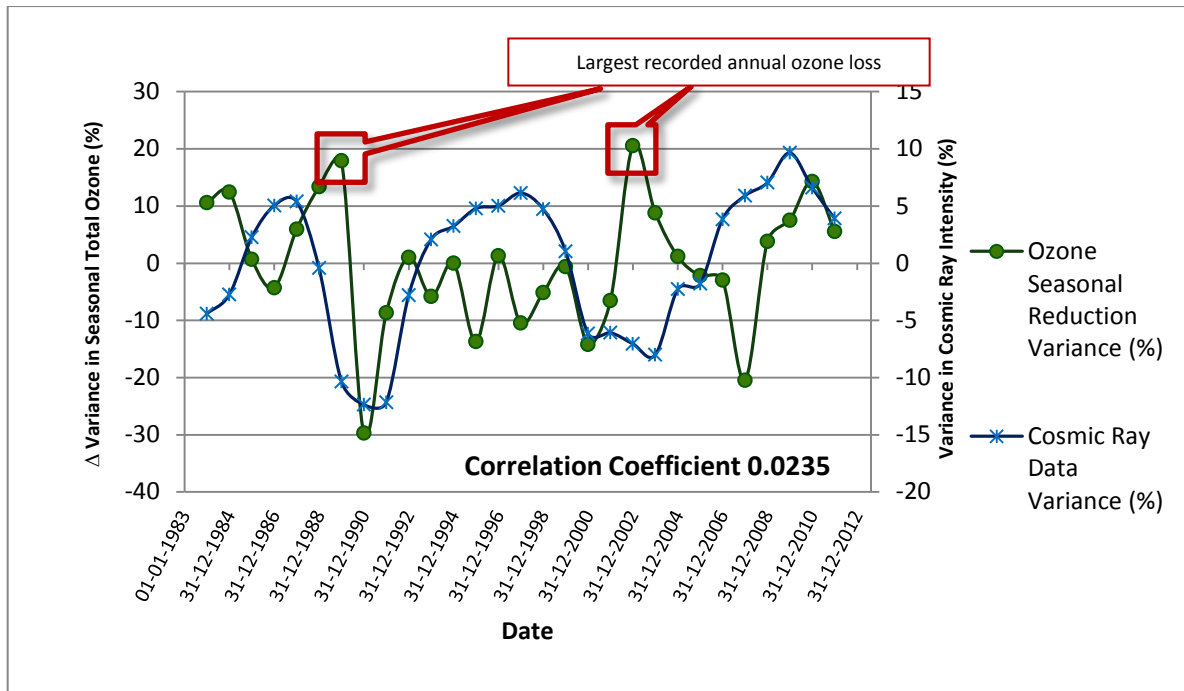


**Figure 5.17: The relationship between neutron monitor cosmic ray intensity data, as a percentage variance, and the seasonal reduction in total ozone over Thule, Greenland.**

The plot in Figure 5.17 illustrates that the years of greatest ozone loss to be 1989 and 2002 over northern Greenland, with other peaks observed in 1984 and 2010. From this plot, though, there is a lack of a significant correlation between recorded incident cosmic rays and these peaks representing the greatest seasonal change in ozone. The correlation coefficient across the datasets is only 0.02. There does appear to be a possible lag effect, where greater atmospheric ionization could be influencing total column ozone two to five years after the peak in recorded incoming cosmic radiation, but the lag period is not consistent (1989 versus 1987 and 2002 versus 1997). This total ozone data does appear to show a cyclical nature, but the 11-year cycle predicted by Lu [2010a] is not clear. The peaks from Figure 5.17 are 13 years apart. The years of greatest ozone depletion from spring to fall seem to be concurrent with years of lows in recorded cosmic ray values. This may be explained that during cosmic radiation low periods, there is a stronger solar influence and thus, greater column ozone build-up in the springtime. There is possibly some mechanism that causes greater reduction in ozone during these periods of excess ozone. Reviewing the ozone data, the largest springtime ozone values (>500 DU) occurred

in the years 1984, 1989, 2002, 2007 and 2008, two of which these also indicated the largest recorded seasonal reductions.

From these data graphs (Figures 5.12-5.15 and 5.17), it is interesting to note that, with the extension of the data to 2011, the cosmic ray activity demonstrates a considerable increase, both to the lowest value noted in 2003 to the following peak value from 2009 (indicated by the red bracket in Figure 5.12). This increase is in the order of fourteen percent (14.18% greater than the annual mean value in 1997), over the previous two cycles. Based on theory, this could significantly impact cloud cover and from Henrik Svensmark, cause a cooling episode for the Earth (Svensmark, 2010).

Since this polar satellite data alone only detects ozone in the presence of sunlight, data is absent over the time period from about mid-October to late February for northern Greenland, making some of the monthly means based on only a partial month of data. The TEMIS dataset that combined several sources of data did allow for a year-round database of values. Below, we compare the results from the collection of TOMS, OMI and SBUV satellite data and the multi-sensor TEMIS product (Figure 5.18).

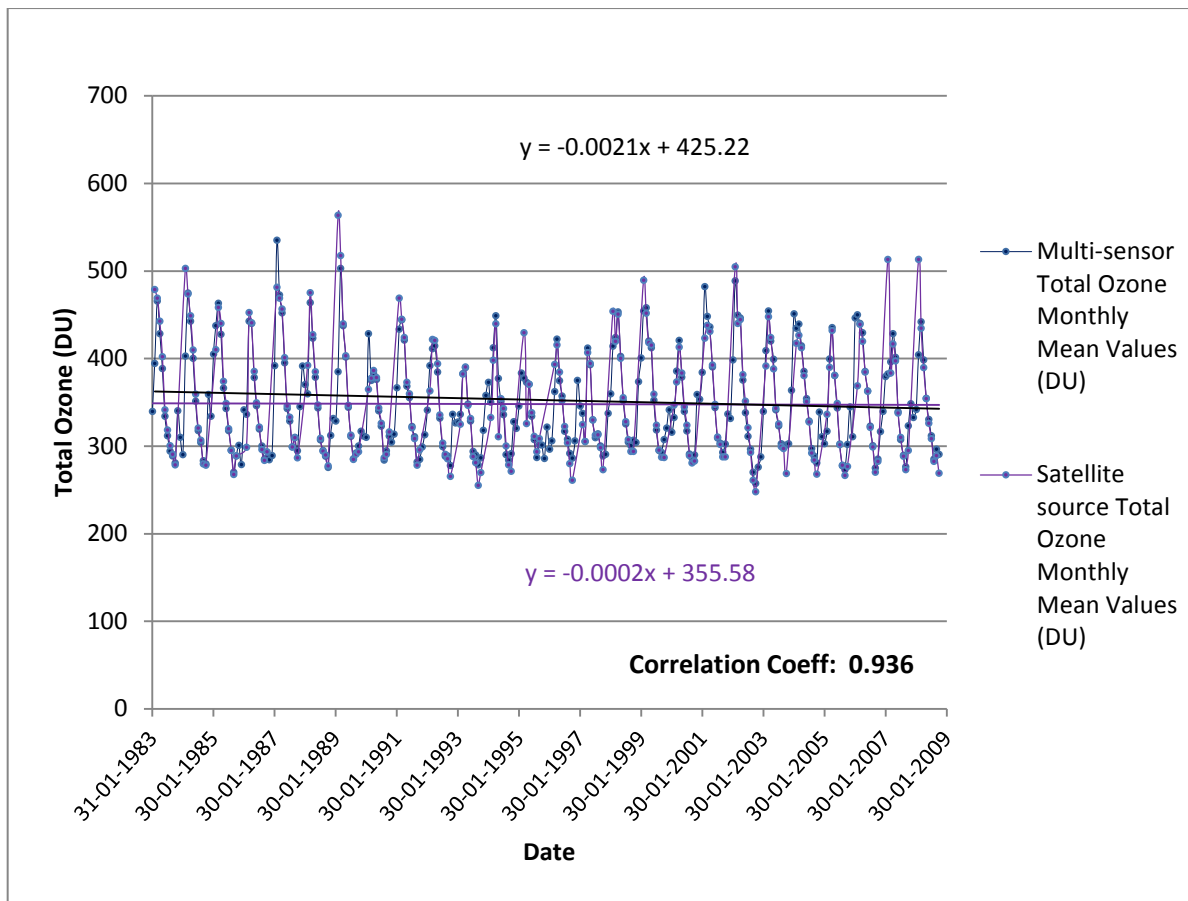


**Figure 5.18: Comparison of total column ozone values from the TOMS-OMI-SBUV collection of satellite data versus the TEMIS Multi-sensor data collaboration.**

From Figure 5.18, The TOMS-OMI-SBUV collection of satellite data and the TEMIS multi-sensor dataset demonstrate a strong correlation (0.94) when examining the monthly mean values. The linear best fit trend line from the TOMS-OMI-SBUV data (black) is displayed at the top of this graph while the TEMIS result (purple) is shown at the bottom of the figure. From this, it does indicate a slight decreasing trend of the ozone data for both datasets over the study period from 1983 to 2008 with slopes of -0.0021 and -0.0002, respectively.

Charts and correlation coefficients were computed for the TEMIS and cosmic ray datasets, similar to the work done in Figures 5.12-5.15, and the results are provided in Table 5.1.

**Table 5.1: Correlation coefficient results after comparing the percentage variance of the Thule, Greenland cosmic ray intensity to both the TOMS-OMI-SBUV and TEMIS multi-sensor ozone datasets.**

<b>Comparison to Cosmic Ray Intensity Data from the Thule Neutron Monitor station</b>	<b>TOMS-OMI-SBUV Satellite Data Correlation Coefficient</b>	<b>TEMIS Multi-Sensor Data Correlation Coefficient</b>
<b>Ozone Annual Mean</b>	-0.21	-0.054
<b>Ozone Annual Maximum Loss Month</b>	-0.081	0.12
<b>Ozone Annual Mean 3-point Moving Average</b>	-0.51	-0.41
<b>Ozone Annual Maximum Loss Month 3-point Moving Average</b>	-0.21	0.51

From this data, the TEMIS dataset showed a range of correlations that differed from the TOMS-OMI-SBUV satellite collection. The strongest correlation for the TEMIS dataset was 0.51, found in the cosmic ray intensity and TEMIS ozone annual maximum loss month 3-point moving average plot. From this, the value of  $t$  from equation 6.1 is 2.80. With the two-tailed result for 22 degrees of freedom being 2.07 and 2.82 at 0.05 and 0.01 degrees of freedom, respectively, this correlation is significant at 0.01 degrees of freedom.

To examine the TEMIS data similarly to the TOMS-OMI-SBUV plot represented by Figure 5.17, Figure 5.19 is generated.

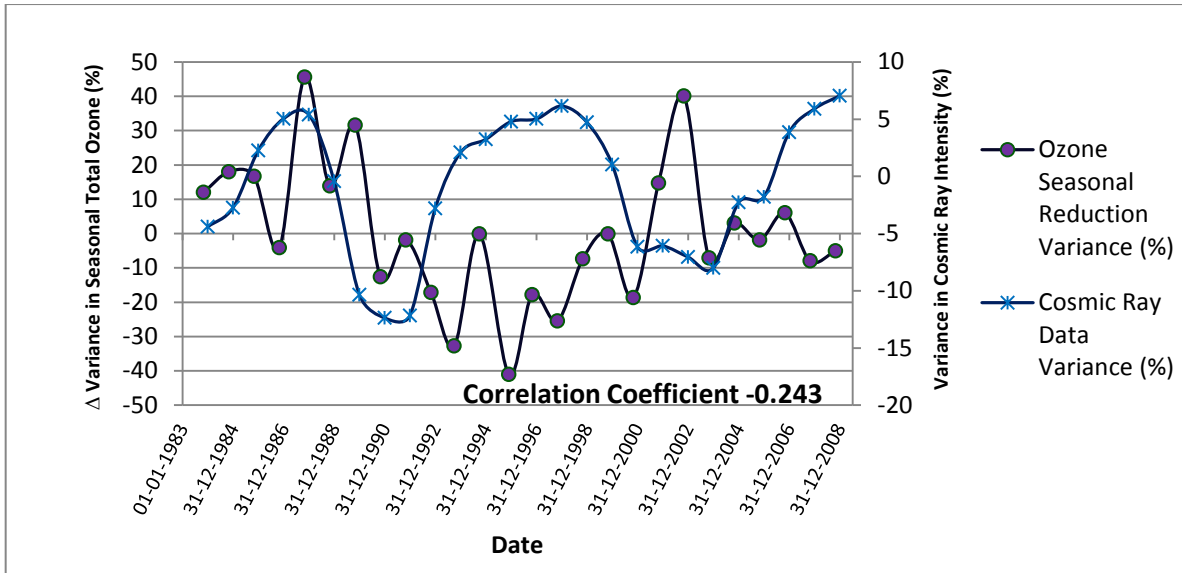


**Figure 5.19: Percentage variance of cosmic ray intensity data charted against the seasonal reduction in total ozone over Thule, Greenland.**

The seasonal annual reduction values, from Figure 5.19, were computed as the difference between the largest springtime and the smallest fall monthly means as recorded in the Arctic from the TEMIS multi-sensor dataset. From this figure, the years of greatest depletion in seasonal ozone occurred during 1987, 1989, 1994 and 2002. Of these findings, only 1987 corresponded to the years found where both cosmic ray activity and ice cloud tau were larger, from Figure 5.3. None of the years of 1983, 1985, 2007 or 2009, where heightened cosmic ray intensity were measured (from Figures 5.5 and 5.11), corresponded with ice cloud persistence over Thule, Greenland. A 15-year separation is noted between the ozone data peaks (Figure 5.19).

In the Arctic, the ozone layer recovers over the winter, showing its greatest column thickness between February and April and thinnest column in September or October (see Table 4.1). Monthly-averaged cosmic ray intensity is charted against monthly change in total ozone, in Figures 5.20 and 5.21.

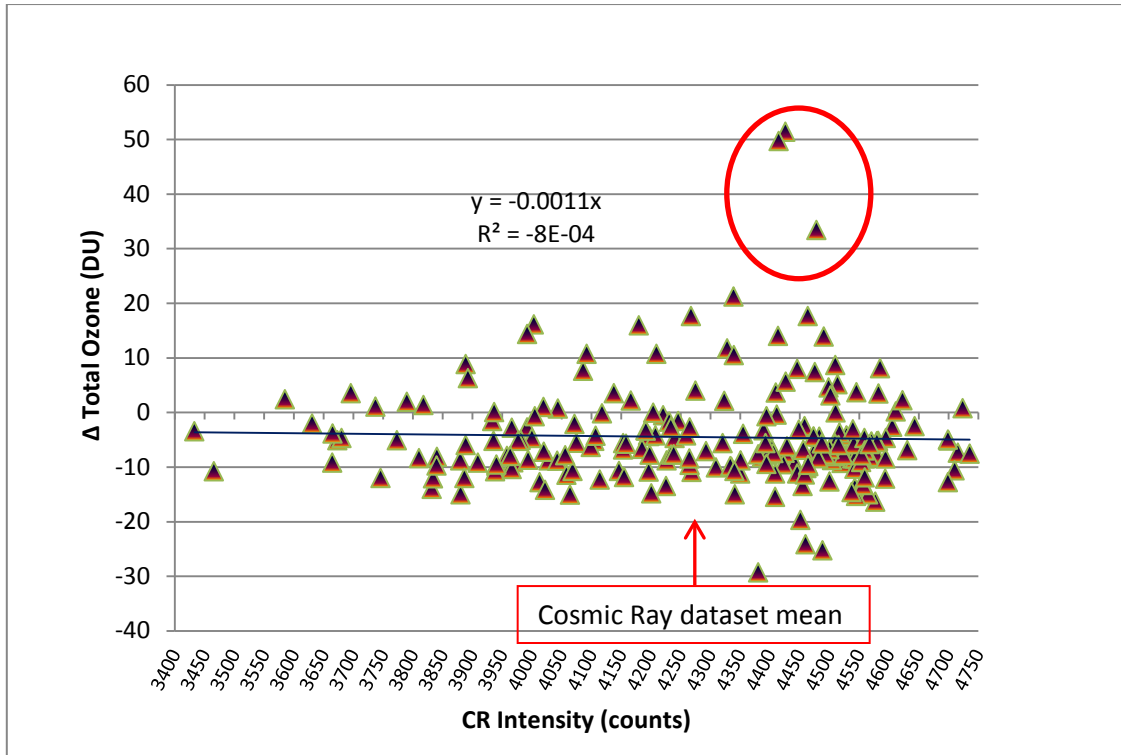


**Figure 5.20: Comparison of cosmic ray intensity data and monthly differences in total column ozone from TOMS-OMI-SBUV satellite sources over Thule, Greenland.**

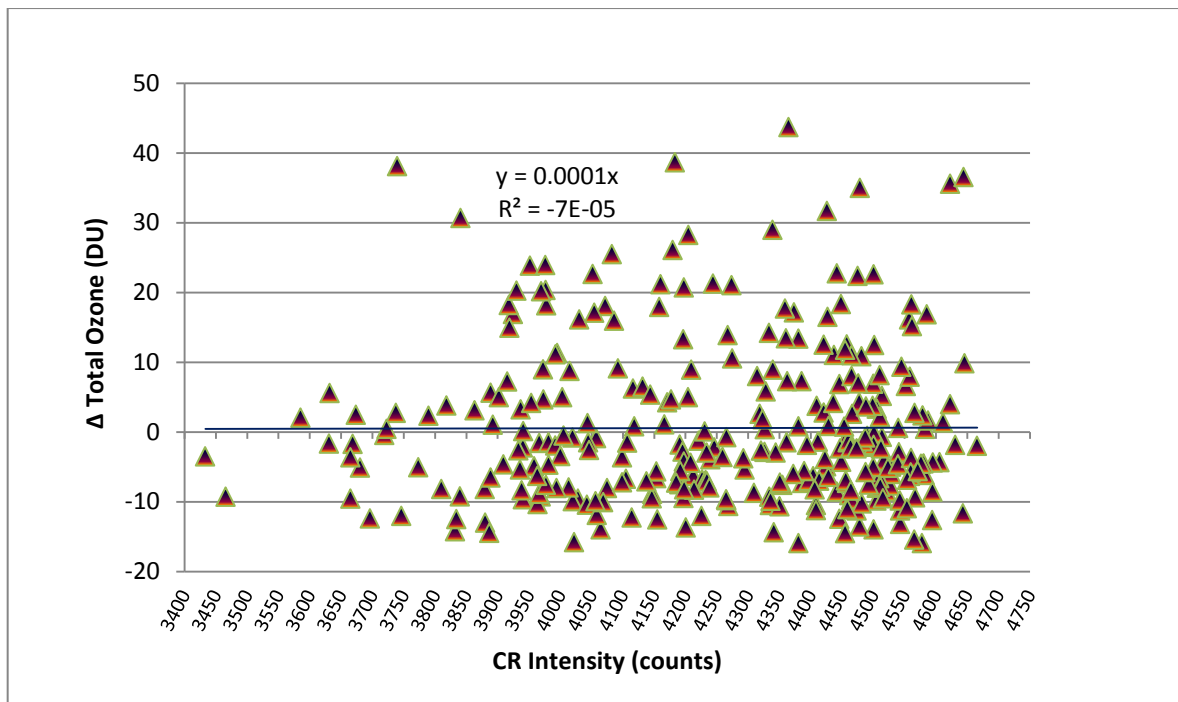


**Figure 5.21. Comparison of cosmic ray intensity data and monthly differences in total column ozone based on TEMIS multi-sensor data over Thule, Greenland.**

The equations and correlation coefficients shown in each of these figures (Figure 5.20 and 5.21) are based on a linear trend line through the data (shown in black). Since the TEMIS ozone product was not missing data during the winter months over the Greenland station, it is interesting to note that there is greater dispersion in this plot (Figure 5.21). This dataset included modeled data generated for the winter months. This is compared to the satellite-sourced data (Figure 5.20) that shows a stronger linear relationship around the trend line. The spurious points, circled in red, are from the dates March 1986, April 1997 and April 2011. These points show that very large changes in monthly ozone values relate to moderately high cosmic ray intensity counts where the CR average for the data is 4274 (marked by red arrow in Figure 5.20).

### 5.3 Polar Ice Cloud and Total Column Ozone Comparisons

Finally, it is critical to do comparisons between ice cloud tau, ice cloud persistence and ozone measurements to understand if any further relationships exist between these datasets. Increase ice cloud presence and persistence, particularly in the case of

stratospheric clouds, should result in increased ozone loss. The charts in Figures 5.22 to 5.29 were generated to replicate on the findings by Harris et al. [2010]. Harris and his team developed a linear relationship between modeled Arctic polar stratospheric cloud volume and ozone loss as illustrated in Figure 2.9.

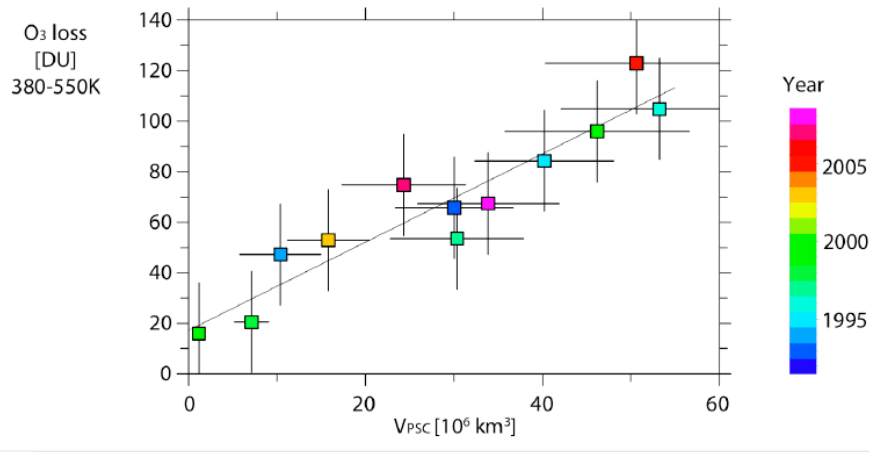


**Figure 2.9: Integrated ozone loss as a function of polar stratospheric cloud volume [from Harris et al., 2010, with permission].**

He stated that ozone loss is effected by “a number of the three-dimensional processes” including

- (1) pressure (altitude)
- (2) the increasing  $Cl_y$  with altitude
- (3) the vertical redistribution of  $NO_y$  in de / re-nitrification
- (4) the inter-annual variation of transport [Harris et al., 2010]

In the following figures, ice cloud tau is substituted for volume of PSCs and seasonal ozone loss (Feburary to September) replaces winter ozone loss (January to March) from the Harris et al. [2010] dataset.

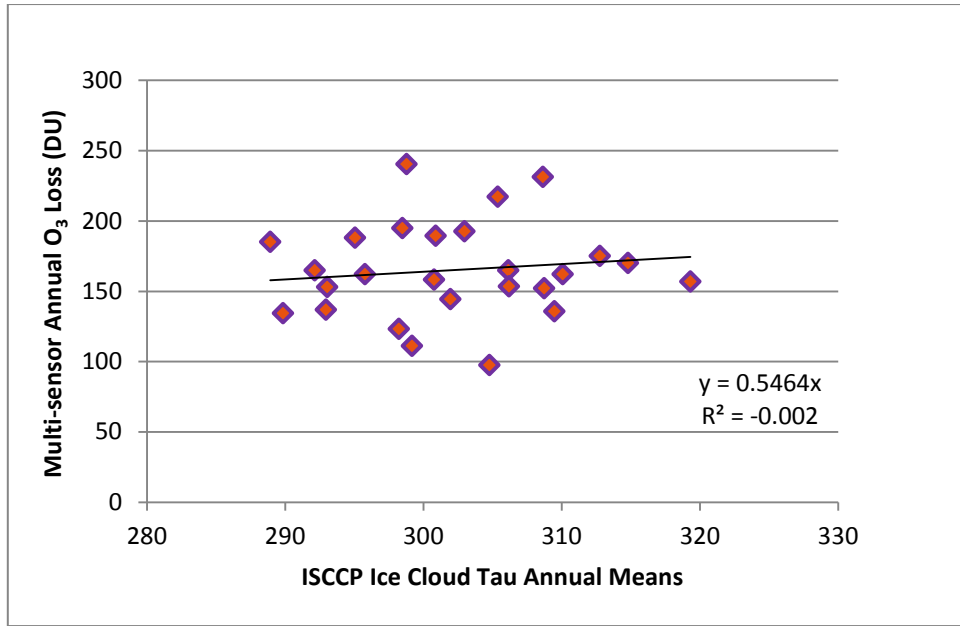


**Figure 5.22: Satellite ISCCP ice cloud tau annual mean data versus TEMIS multi-sensor annual ozone loss data from 1983 to 2008.**

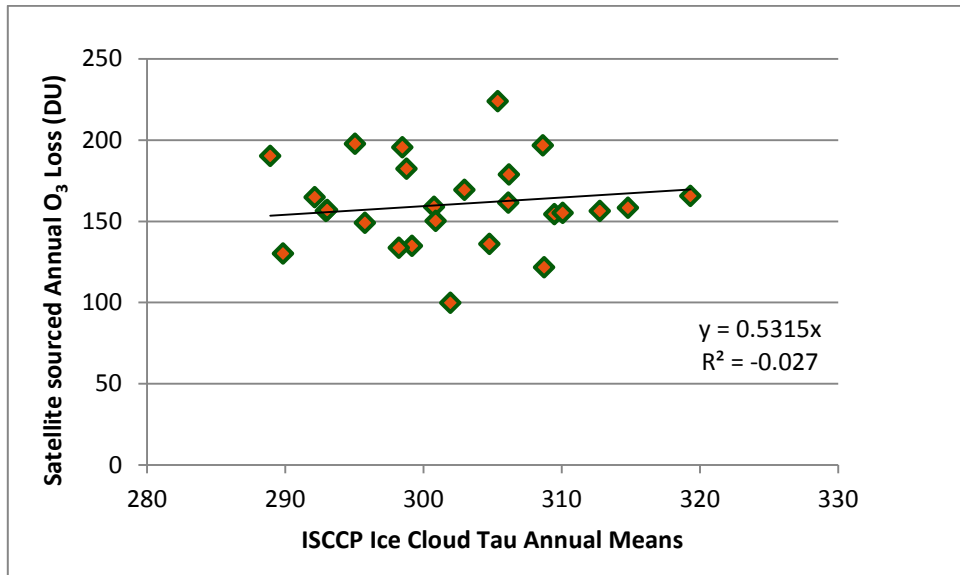


**Figure 5.23: Satellite ISCCP ice cloud tau annual mean data versus TOMS-OMI-SBUV satellite annual ozone loss data from 1983 to 2008.**

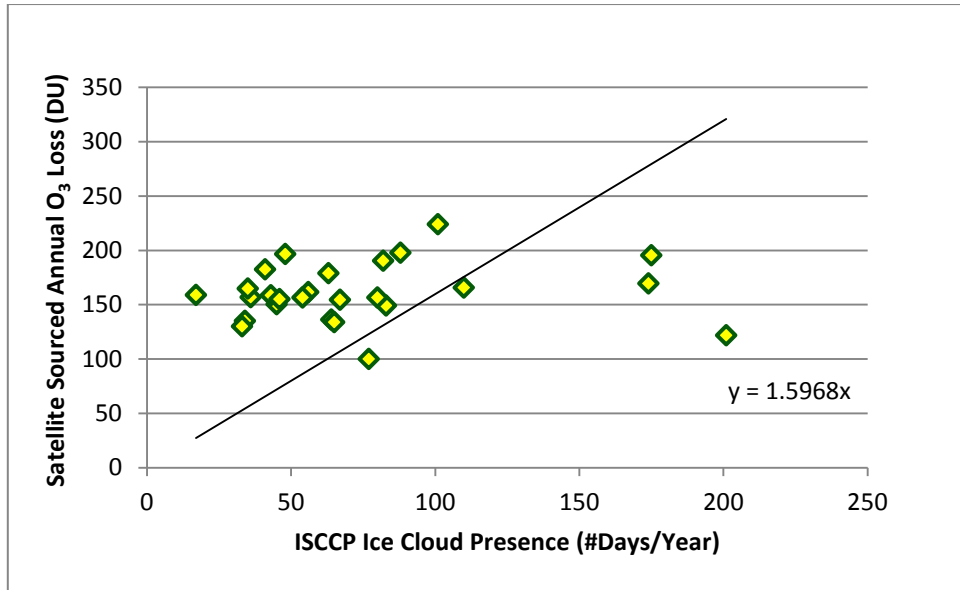


Figure 5.24: Satellite-based ISCCP annual ice cloud persistence versus TOMS-OMI-SBUV satellite annual ozone loss data from 1983 to 2008.

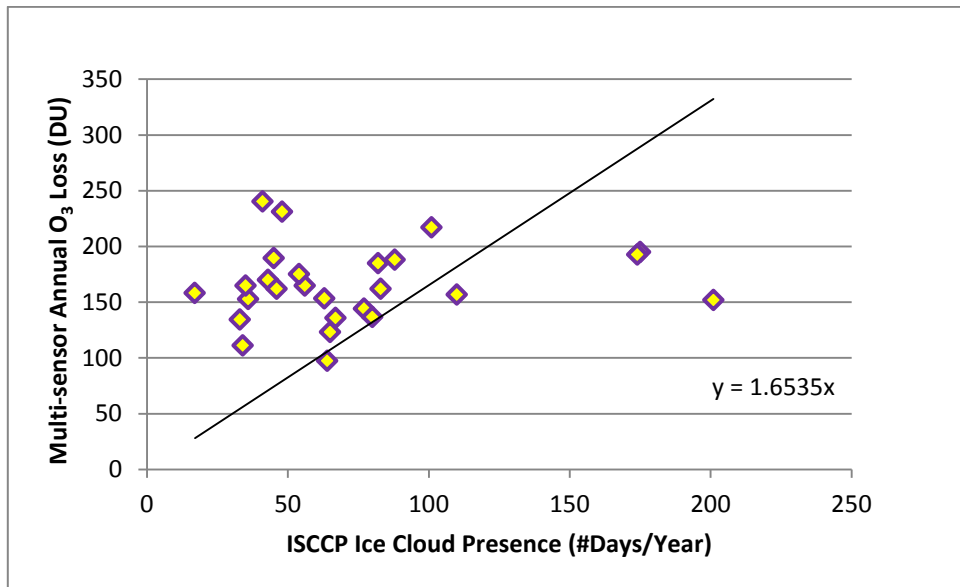
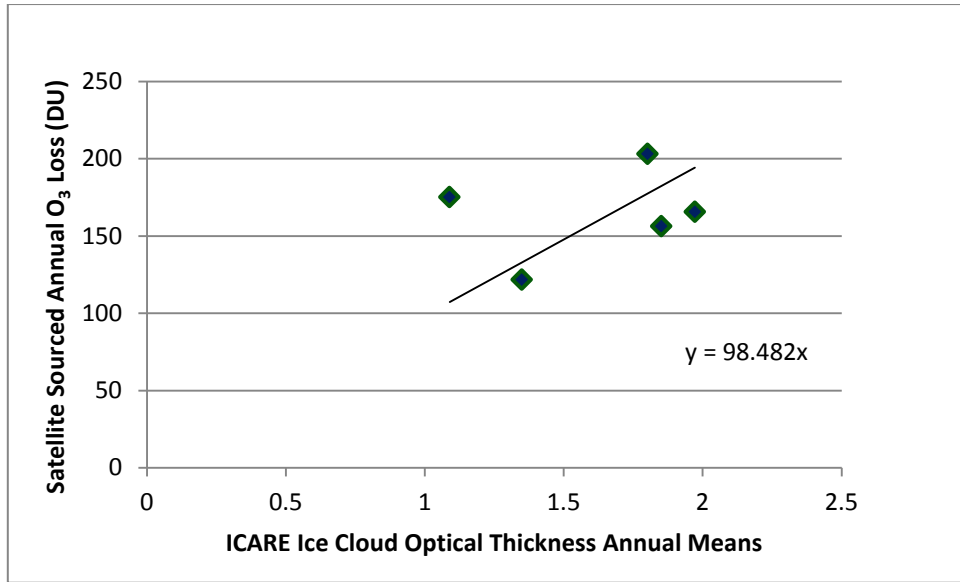
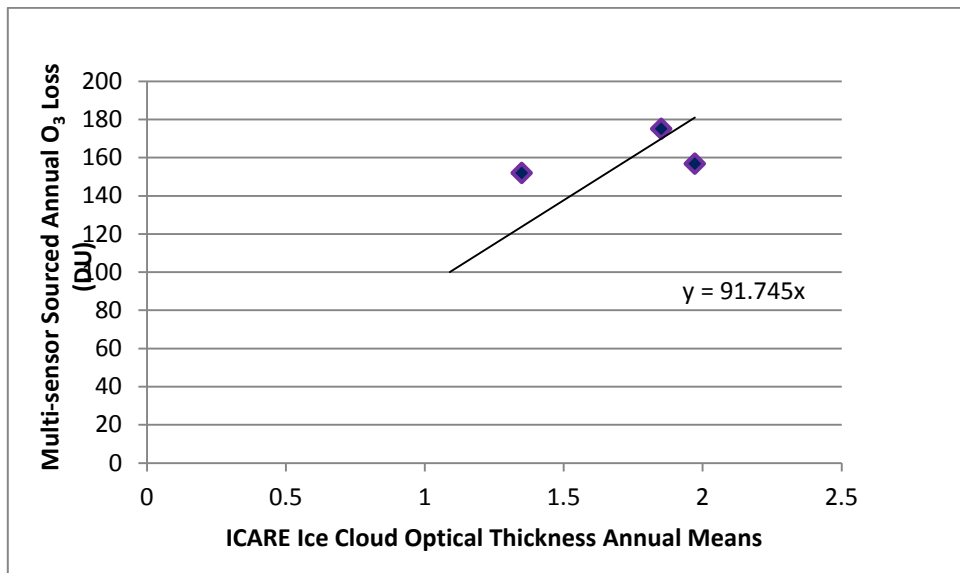


Figure 5.25: Satellite-based ISCCP annual ice cloud persistence versus TEMIS multi-sensor annual ozone loss data from 1983 to 2008.



**Figure 5.26: Satellite ICARE DARDAR ice cloud optical thickness annual mean data versus TEMIS multi-sensor annual ozone loss data from 2006 to 2010.**



**Figure 5.27: Satellite ICARE DARDAR ice cloud optical thickness annual mean data versus TOMS-OMI-SBUV satellite annual ozone loss data from 2006 to 2010.**

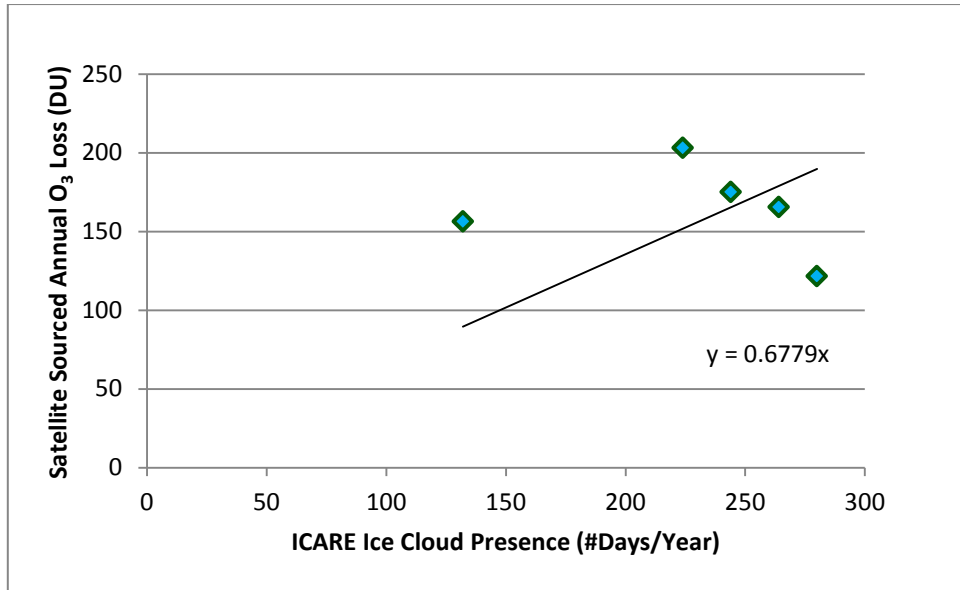


**Figure 5.28: Satellite-based ICARE DARDAR annual ice cloud persistence versus TOMS-OMI-SBUV satellite annual ozone loss data from 2006 to 2010.**

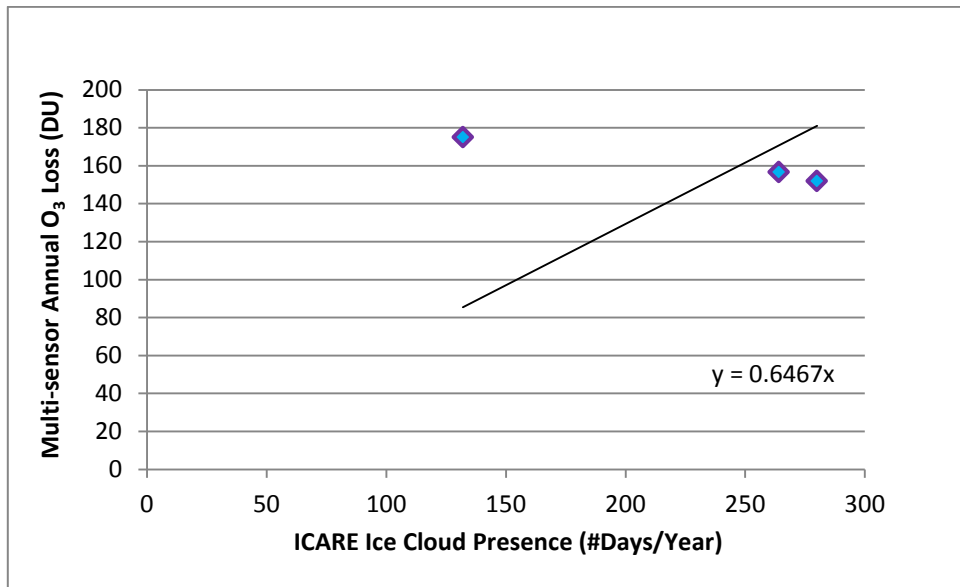


**Figure 5.29: Satellite-based ICARE DARDAR annual ice cloud persistence versus TEMIS multi-sensor annual ozone loss data from 2006 to 2008.**

The results from Figures 5.22 through 5.29, which compared all available datasets of ice clouds and total column ozone for this study, did not produce compelling linear relationships. A positive aspect of both of the DARDAR and TEMIS datasets is that they

provide year-round data products, but there was a lack of data points for the results in Figures 5.26 through 5.29 and reasonable best fit correlations could not be created.

The clustered data in Figures 5.22 to 5.23 detailed the closest results to a linear relationship, but the correlation coefficients are very low at  $-0.002$  and  $-0.027$ , respectively. These were unlike the strong relationship produced by the work of Harris et al. [2010] and Rex et al. [2006]. In their work, Arctic polar stratospheric cloud volume and months of ozone loss, as it relates to a specific layer case expressed by a temperature range, were compared. Although five years of data is excluded from the results in Figure 2.9, it is apparent that the ECMWF ERA-Interim re-analysis product for the cloud data, from Harris et al. [2010], developed using a coupled chemistry climate model, is quite different from the ice cloud tau or optical thickness products used in this study.

Differences between the studies can be expressed as follows:

1. The focus from Harris et al. [2010] was the stratospheric Arctic cloud volume where this study included the full cloud amount (ISCCP) and stratospheric data was not included in the DARDAR ice cloud data product due to its unique nature.
2. Harris et al. [2010] used a winter ozone loss computation based on a 380-550 K partial column defined by the lower stratosphere, where the total ozone column was analyzed over a different portion of the year for this study (spring to fall differences).

#### **5.4 Other Data Comparisons**

The winter of 2005 was identified as being a year of extremely low temperatures as measured in the Arctic polar vortex [Rex et al., 2006]. These cold temperatures were predicted to increase the volume of PSCs and reduce the amount of chlorine and bromine species in the stratosphere. From this work, the volumes of PSCs progressively increased over the years from 1966 to 2005, but also showed greater variability over this growth period (see Figure 5.30).

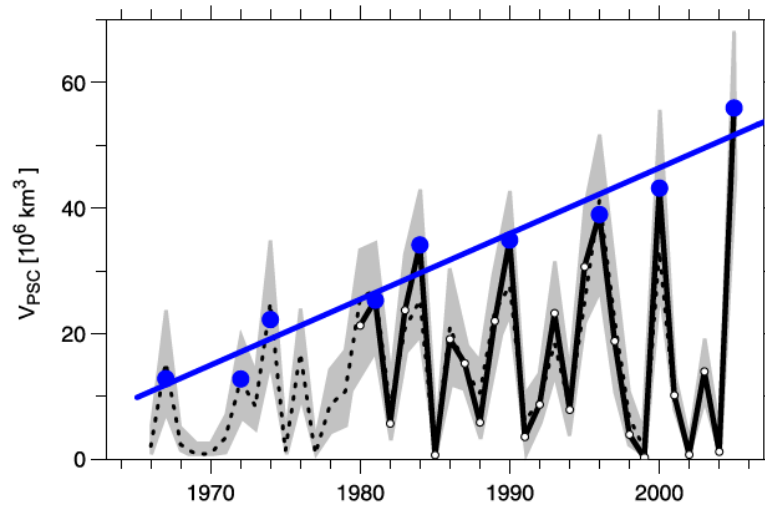


**Figure 5.30: Volume of PSCs sourced from the ECMWF database, computed for temperatures between 380 and 550 K [from Rex et al., 2006, with permission].**

From Figure 5.30, the solid line represents ECMWF data and the dashed line is FU-Berlin data. “The grey shading represents uncertainty of  $V_{PSC}$  due to 1 K uncertainty of the long term stability of radiosonde temperatures” [Rex et al., 2006]. The years of greatest volume of PSCs as 1984, 1988, 1990, 1993, 1996, 2000, and 2005 can be compared to this study’s datasets for total column ozone analysis. Over the similar years of study, lows were seen in 1985, 1990, 1993, 1996, 2000 and 2005 for annual ozone records as shown in Figure 5.12. Extension of this data would be critical to determine if the 2008 and 2011 Arctic ozone loss is reflected in the volume of PSCs.

Lu [2010b] compared the influence of both CFCs and  $CO_2$  on global warming. He identified that CFCs had the greatest influence on atmospheric temperature. Here, we investigate the measured quantities of Arctic atmospheric CFCs and  $CO_2$ , to determine if either of these atmospheric molecules follows the same trends as seen in the previous polar ice cloud or ice cloud tau measurements (see Figure 5.31 and 5.32).

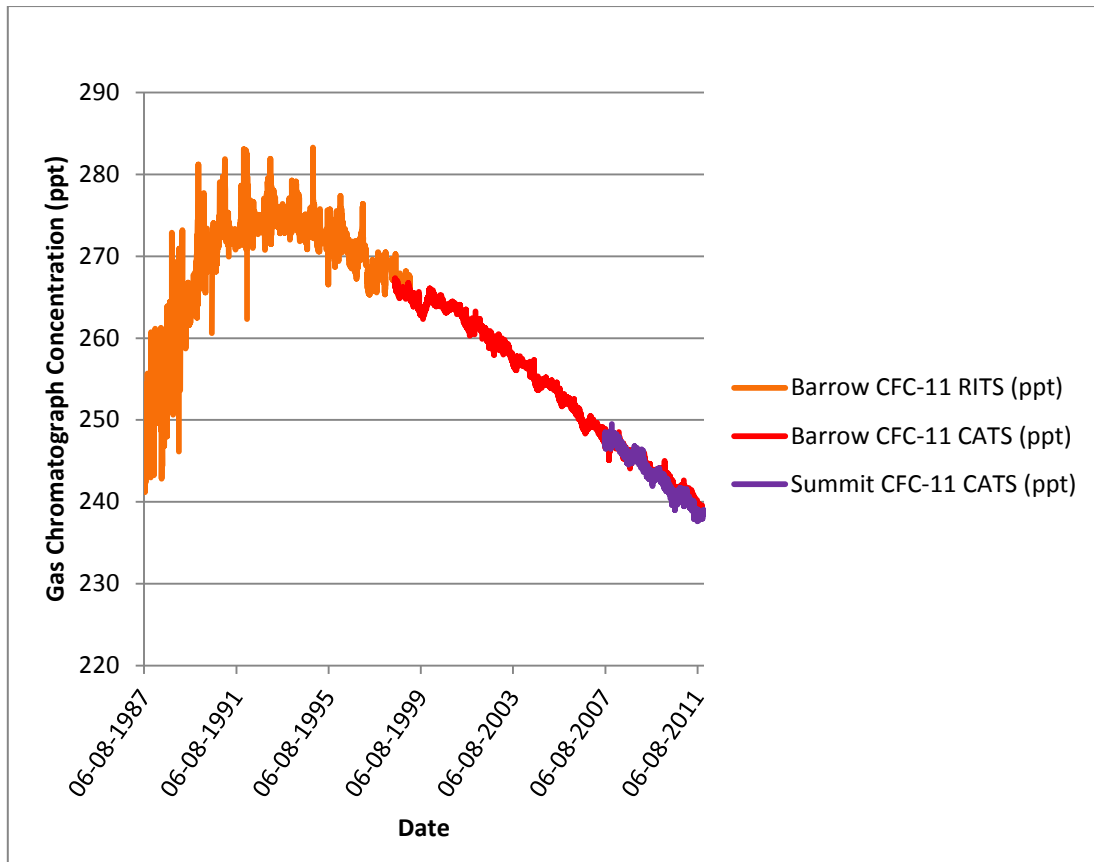


**Figure 5.31: CFC-11 insitu gas chromatograph daily averages from NOAA/ESRL Radiatively Important Trace Species (RITS) and Chromatograph for Atmospheric Trace Species (CATS) programs from Barrow, Alaska (71.3 N, 156.6 W, elevation: 8 m) and Summit, Greenland (72.58 N, 38.45 W, elevation: 3238 m)**

Viewing the data in Figure 5.31, there is no clear indication that increased detection of CFC-11 from 1989 to 1994 has a direct influence on seasonal ozone reduction as shown in Figure 5.16. In Figure 5.16, where the years of greatest month-to-month ozone loss were 1994, 1997, 2002 and 2007, there is no obvious relationship.

The general increase in ice cloud tau, from 1983 to 2006, as observed in Figure 5.1 cannot be explained by the gas chromatograph work shown in Figure 5.31. There is an apparent curvature in the data from 1994 to 1999, but it does not trend downward in the same manner as the CFC-11 gas chromatograph data.

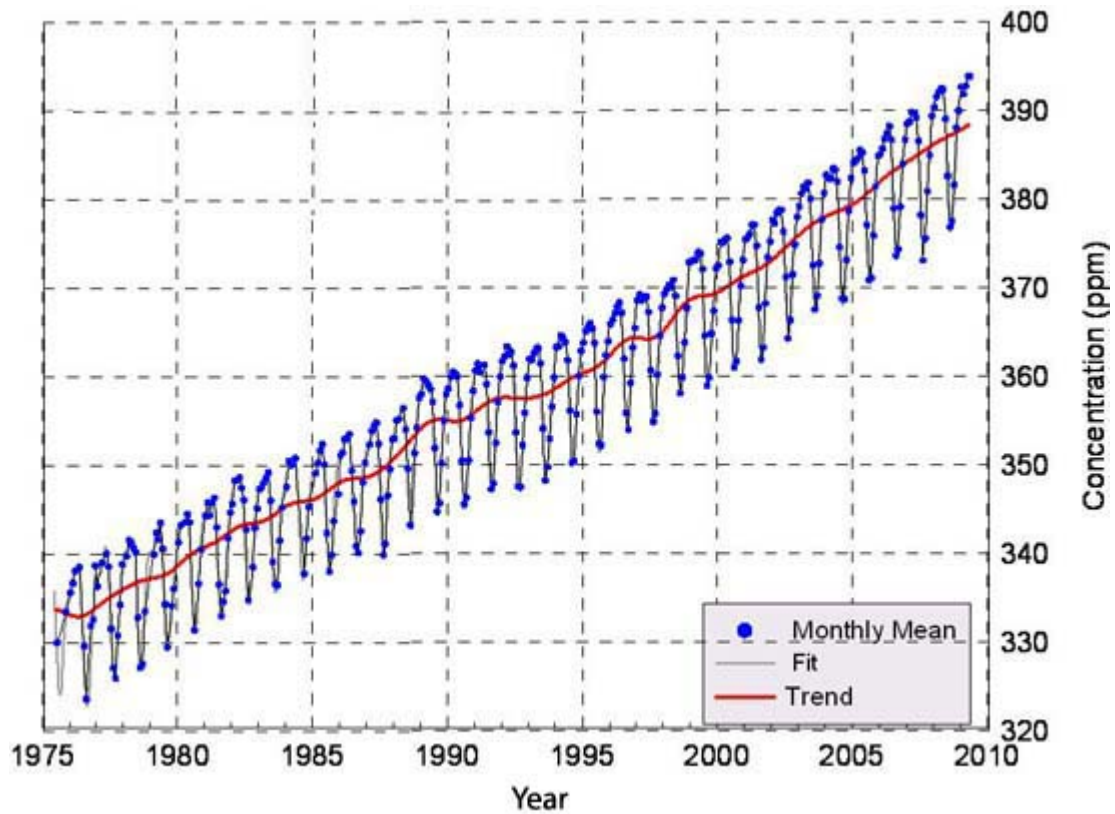


**Figure 5.32: Atmospheric Carbon Dioxide (CO<sub>2</sub>) as measured at Alert, Canada for the period from 1975 to 2009 [from Environment Canada, 2012].**

The increase in CO<sub>2</sub> (Figure 5.32) from 1975 to 2010, is reflected in the overall trends of total column ozone from Figure 5.18 and ISCCP ice cloud tau data from Figure 5.1.

Increased concentration of atmospheric CO<sub>2</sub> would affect aerosol density. Combined with soot and other aerosols, this process would cause incoming solar radiance to be trapped in the lower troposphere between the CO<sub>2</sub> layer and the Earth's surface. This potentially results in surface warming and a cooling of the stratosphere. Cooling of the stratosphere would allow PSCs to form and might ultimately affect the ozone layer that resides at this atmospheric level. The magnitude of the trends must be analyzed further to understand any possible influences between these parameters.

## CHAPTER 6: CONCLUSIONS AND FUTURE WORK

### 6.1 Conclusions

This study examined the potential influence of cosmic rays on polar ice cloud optical thickness ( $\tau$ ) and persistence and their overall effect on total column ozone. The results were varied. The strongest results confirming work from previous studies were found to be:

1. The similarities between the regional Arctic work with cosmic rays and total column ozone compared to the Antarctic results presented by Lu [2009] and
2. The five identified years of lows in total column ozone that matched the peaks in volume of PSCs as previously demonstrated in research by Rex et. al. [2006].

Other findings showed that Arctic CO<sub>2</sub> measurements trended along with ice cloud  $\tau$  and oppositely with total ozone computations over the study timeframe.

Relationships between spring to fall seasonal reductions in ozone were not easily seen as being a result of increased atmospheric ionization, based on the cosmic ray data. Ice cloud optical thickness did not produce strong linear relationships with total column ozone and may not have been the best measure to use in these comparisons. This may be explained by the following statements. In the case of the ISCCP data, there was a focus on the total cloud optical thickness which was complicated by cloud detection errors in the polar vortex due to presence of surface ice and the assumption of temperature of ice clouds based on the total column. In the DARDAR data result, the focus was not on stratospheric ice clouds and possibly, the remainder of the ice cloud volume did not have as great an influence on changes in the ozone column.

Unexpected observations included an exposed cosmic ray data peak that was 14 percent larger than the two previous 11-year cycles when the data length was extended to 2011, and clear differences that existed between the ISCCP ice cloud  $\tau$  and ICARE DARDAR ice cloud optical thickness parameters. Additionally, comparisons of polar ice cloud and

ozone data to atmospheric aerosols produced a more obvious connection to CO<sub>2</sub> rather than chlorofluorocarbons, as measured by CFC-11.

Rossow [2011] suggested that it may be necessary to utilize a more extensive research area, as 300 km was the minimum recommendation from his research. From Enghoff [2011], it is possible that rather than focusing on total ice cloud parameters from the entire cloud column, that specific cloud types, such as low level clouds from Table 3.4, should be the focus.

Overall, this study was very interesting and involved several sources of data to produce the comprehensive results. In many cases, longer-term data was needed and is identified as the key to determining if any strong relationships exist between datasets or periodic cycling of data could be identified. This was particularly important in the cases of monthly and yearly ice cloud presence and persistence.

Due to the noted correspondence between peaks in ice cloud persistence as generated from the ICARE DARDAR database and cosmic ray intensity as recorded by the Thule, Greenland neutron monitor station, it is important to continue this analysis as more data is collected and released for future studies.

## **6.2 Recommendations**

The recent availability of comprehensive datasets, such as ICARE DARDAR collection of data that encompassed inputs of radar, lidar and spectroradiometer data, has created opportunities for further detailed atmospheric research to be conducted. From this work, additional studies that focus on specific parameters, such as iwc or effective radius, may provide better calculations of ice cloud surface area. This could allow for further insight of natural processes that occur in cases of chemical reactions on ice surfaces. Much of this data is also available in layers where the data changes with altitude. Modeling work that includes this additional detail could reveal more intricate solutions and ideas. This may

also improve understanding around global atmospheric models of air transport. Further work may include breaking down comparative datasets over smaller time frames so as to not overlook significant correlations within the datasets.

Continued research, similar to that produced by Rex et al. [2006] and Harris et al. [2010] on PSCs and partial column ozone using a coupled chemistry climate model approach should be completed. This would potentially lead to a clearer understanding of the cause-effect nature that focuses solely on stratospheric processes. Additional work analyzing various types of aerosols, alone or in combination, as they react both in the CERN facility and in the environment are important to understand the changes in the global climate. For example, analysis of organic carbon sources of soot that, as an aerosol, may cause increases in CCN and have an effect on cloud optical thickness and albedo, could be completed.

## REFERENCES

### Publications

- Bieber, John W., Paul Evenson, Wolfgang Dröge, Roger Pyle, David Ruffolo, Maniit Rujiwarodom, Paisan Tooprakai and Thiranee Khumlumlert. 2004. Spaceship Earth observations of the Easter 2001 solar particle event. *The Astrophysical Journal*, Volume 601, Pages L103-L106.
- Brown, P. R. A. and Francis P. N. 1995. Improved measurements of the ice water content in cirrus using a total-water probe. *Journal of Atmospheric and Oceanic Technology*, Volume 12, Pages 410-414.
- Cairns, B. A. A. Lacis and B. E. Carlson. 2000. Absorption within inhomogeneous clouds and its parameterization in general circulation models. *Journal of Atmospheric Science*, Volume 57, Pages 700-714.
- Clem, John M. and Lev I. Dorman. 2000. Neutron Monitor Response Functions. *Space Science Reviews*, Volume 93, Pages 335-359.
- Delanoë, Julien and Robin J. Hogan. 2008. A variational scheme for retrieving ice cloud properties from combined radar, lidar, and infrared radiometer. *Journal of Geophysical Research*, Volume 113, D07204, Pages 1-21.
- Delanoë, Julien and Robin J. Hogan. 2010. Combined CloudSat-CALIPSO-MODIS retrievals of the properties of ice clouds. *Journal of Geophysical Research*, Volume 115, D99H29, Pages 1-17.
- Enghoff, Martin B., Jens Olaf Pepke Pedersen, Ulrik I. Uggerhøj, Sean M. Paling and Henrik Svensmark. 2011. Aerosol nucleation induced by a high energy particle beam. *Geophysical Research Letters*, Volume 38, L09805, Pages 1-4.
- Fabrikant, Ilya I. 2007. Dissociative electron attachment on surfaces and in bulk media. *Physical Review A*, Volume 76, Pages 012902-1 to 012902-12.
- Francis, P. N., P. Hignett and A. Macke. 1998. The retrieval of cirrus cloud properties from aircraft multi-spectral reflectance measurements during EUCREX'93. *Quarterly Journal of the Royal Meteorological Society*, Volume 124, Pages 1273-1291.
- Fortuin, J. Paul F. and Hennie Kelder. 1998. An ozone climatology based on ozonesonde and satellite measurements. *Journal of Geophysical Research*, Volume 103, Number D24, Pages 31,709 - 31,734.
- Frieler, K., M. Rex, R. J. Salawitch, T. Canty, M. Streibel, R. M. Stimpfle, K. Pfeilsticker, M.

- Dorf, D. K. Weisenstein and S. Godin-Beekmann. 2006. Toward a better quantitative understanding of polar stratospheric ozone loss. *Geophysical Research Letters*, Volume 33, L10812, doi:10.1029/2005GL025466.
- Haigh, J.D., Lockwood, M. and Giampapa, M.S. 2005. The Sun, Solar Analogs and the Climate. Edited by Ruedi, I, Gudel, M. and Schmutz, W. *Springer-Verlag Berlin Heidelberg, The Netherlands*.
- Han, Q.-Y., J. Chou, K.-S. Kuo and R.M. Welch. 1999. The effects of aspect ratio and surface roughness on satellite retrievals of ice-cloud properties. *Journal of Quantitative Spectroscopy and Radiative Transfer*, Volume 63, Issues 2-6, Pages 559-583.
- Harris, N.R.P., R. Lehmann, M. Rex and P. von der Gathen. 2010. A closer look at Arctic ozone loss and polar stratospheric clouds. *Atmospheric Chemistry and Physics Discussions*, Volume 10, Pages 6681-6712.
- Harrison, R. Giles. 2008. Discrimination between Cosmic Ray and Solar Irradiance Effects on Clouds, and Evidence for Geophysical Modulation of Cloud Thickness. *Proceedings of the Royal Society A: Mathematical, Physical and Engineering Sciences*. Volume 464, Pages 2575-2590.
- Harrison, R. Giles and Ambaum, Maarten H.P. 2008. Enhancement of Cloud Formation by Droplet Charging. *Proceedings of the Royal Society A: Mathematical, Physical and Engineering Sciences*. Volume 464, Pages 2561-2573.
- Hogan, R. J. 2006. Fast approximate calculation of multiply scattered lidar returns. *Applied Optics*, Volume 45, Pages 5984 - 5992.
- Kirkby, Jasper. 2007. Cosmic Rays and Climate. *Surveys in Geophysics*, Volume 28, Pages 333-375.
- Lin, B. and W.B. Rossow. 1996. Seasonal variation of liquid and ice water path in nonprecipitating clouds over oceans. *Journal of Climate*, Volume 9, Pages 2890-2902.
- Lu, Q.-B. 2009. Correlation between Cosmic Rays and Ozone Depletion. *Physical Review Letters*, Volume 102, Pages 118501-1 to 118501-4.
- Lu, Q.-B. and Theodore E. Madey. 1999. Negative-Ion Enhancements in Electron-Stimulated Desorption of CF<sub>2</sub>Cl<sub>2</sub> Coadsorbed with Nonpolar and Polar Gases on Ru(0001). *Physical Review Letters*, Volume 82, Number 20, Pages 4122-4125.
- Lu Q.-B. and L. Sanche. 2001. Effects of Cosmic Rays on Atmospheric

Chlorofluorocarbon Dissociation and Ozone Depletion. *Physical Review Letters*, Volume 87, Number 7, Pages 078501-1 to 078501-4.

Lu, Qing-Bin. 2010a. Cosmic-ray-driven electron-induced reactions of halogenated molecules adsorbed on ice surfaces: Implications for atmospheric ozone depletion and global climate change. *Physics Reports*, Volume 487, Pages 141-167.

Lu, Qing-Bin. 2010b. What is the Major Culprit for Global Warming: CFCs or CO<sub>2</sub>? *Journal of Cosmology*, Volume 8, Pages 1846-1862.

Mason, B.J. 1971. *Physics of Clouds*. Oxford, UK: Pergamon.

Meehl, Gerald A., Julie M. Arblaster, Katja Matthes, Fabrizio Sassi and Harry van Loon. 2009. Amplifying the Pacific Climate System Response to a Small 11-Year Solar Cycle Forcing. *Science* Volume 28, Pages 1114-1118.

Moraal, H., A. Belov and J. M. Clem. 2000. Design and coordination of multi-station International neutron monitor networks. *Space Science Reviews*, Volume 93, Number 1–2, Pages 285–303.

Muller, Rolf. 2003. Impact of Cosmic Rays on Stratospheric Chlorine Chemistry and Ozone Depletion. *Physical Review Letters*, Volume 91, Number 5, Pages 058502-1 to 058502-4.

Nakayama, Nozomi, Stephen C. Wilson, Laura E. Stadelmann, Hsiao-Lu D. Lee, Casey A. Cable and Christopher R. Arumainayagam. 2004. Low-Energy Electron-Induced Chemistry of CF<sub>2</sub>Cl<sub>2</sub>: Implications for the Ozone Hole? *Journal of Physical Chemistry B*, Volume 108, Pages 7950-7954.

Rex, M., R. J. Salawitch, H. Deckelmann, P. von der Gathen, N. R. P. Harris, M. P. Chipperfield, B. Naujokat, E. Reimer, M. Allaart, S. B. Andersen, R. Bevilacqua, G. O. Braathen, H. Claude, J. Davies, H. De Backer, H. Dier, V. Dorokhov, H. Fast, M. Gerding, S. Godin-Beekmann, K. Hoppel, B. Johnson, E. Kyro, Z. Litynska, D. Moore, H. Nakane, M. C. Parrondo, A. D. Risley Jr., P. Skrivankova, R. Stübi, P. Viatte, V. Yushkov, and C. Zerefos. 2006. Arctic winter 2005: Implications for stratospheric ozone loss and climate change. *Geophysical Research Letters*, Volume 33, L23808, doi:10.1029/2006GL026731, Pages 1-6.

Rossow, William B. and Robert A. Schiffer. 1999. Advances in Understanding Clouds from ISCCP. *Bulletin of the American Meteorological Society*, Volume 80, Issue 11, Pages 2261-2287.

Rossow, William B., Carl Delo and Brian Cairns. 2002. Implications of the Observed

Mesoscale Variations of Clouds for the Earth's Radiation Budget. *Journal of Climate*, Volume 15, Issue 6, Pages 557-585.

Schiermeier, Quirin. 2007. Chemists poke holes in ozone theory. *Nature*, Volume 449, Pages 382-383.

Svensmark, Henrik, Torsten Bondo and Jacob Svensmark. 2009. Cosmic ray decreases affect atmospheric aerosols and clouds. *Geophysical Research Letters*, Volume 36, L15101, Pages 1-4.

Tachikawa, Hiroto and Abe, Shigeaki. 2007. Reaction dynamics following electron capture of chlorofluorocarbon adsorbed on water cluster: A direct density functional theory molecular dynamics study. *The Journal of Chemical Physics*, Volume 126, Pages 194310-1 to 194310-10.

Tinsley, Brian A., G. B. Burns and Limin Zhou. 2007. The Role of the Global Electric Circuit in Solar and Internal Forcing of Clouds and Climate. *Advances in Space Research*, Volume 40, Pages 1126-1139.

Van der A, R. J., M. A. F. Allaart, and H. J. Eskes. 2010. Multi sensor reanalysis of total ozone. *Atmospheric Chemistry and Physics*, Volume 10, Pages 11277-11294.

### **Websites and Other References**

Atmospheric Circulation. 2001. <http://www.ux1.eiu.edu/~cfjps/1400/circulation.html>. Accessed April 16, 2012.

Barry, Patrick L. 2000. Peering into the Ozone Hole. [http://science.nasa.gov/science-news/science-at-nasa/2000/ast02oct\\_1/](http://science.nasa.gov/science-news/science-at-nasa/2000/ast02oct_1/). Accessed January 25, 2012.

Bartol Research Institute. 2012. University of Delaware Bartol Research Institute Neutron Monitor Program. <http://neutronm.bartol.udel.edu/realtime/thule.html>. Accessed February 7, 2012.

Cloudsat Data Processing Center; A NASA Earth System Science Pathfinder Mission. 2012. <http://www.cloudsat.cira.colostate.edu/dpcstatusQL.php?page=42>. Accessed February 12, 2012.

Corprew, Frank. 1997. Climatology Interdisciplinary Data Collection; Ozone from TOMS. Author: <http://yang.gmu.edu/nasacd/www/toms.html>. Accessed December 16, 2011.

Douglass, Anne. National Aeronautics and Space Administration Goddard Space Flight

Center (GSFC): Aura atmospheric chemistry Ozone Monitoring Instrument  
<http://aura.gsfc.nasa.gov/instruments/omi.html> Accessed January 31, 2012.

Environment Canada. 2012. Highlights of Recent Research.

<http://www.ec.gc.ca/sc-cs/default.asp?lang=En&n=0EC06FB9-1>. Accessed May 22, 2012.

Gleason, Karin L. 2008. Stratospheric Ozone; Monitoring and Research in NOAA.

<http://www.ozonelayer.noaa.gov/science/o3depletion.htm> . Last accessed February 26, 2012.

ICARE. 2012. <http://www.icare.univ-lille1.fr/> . Accessed February 2, 2012.

ISCCP Webmaster. 2005. Cloud Analysis – Part 8: Cloud Microphysics.

<http://isccp.giss.nasa.gov/climanal8.html>. Accessed February 2, 2012.

Kusterer, John M. 2010. International Satellite Cloud Climatology Project (ISCCP ) Langley Data Center Data Set Document.

[http://eosweb.larc.nasa.gov/GUIDE/dataset\\_documents/base\\_isccp\\_dx\\_dataset.html](http://eosweb.larc.nasa.gov/GUIDE/dataset_documents/base_isccp_dx_dataset.html) Accessed February 12, 2012.

McPeters, Richard D. (NASA Official). 2011. National Aeronautics and Space

Administration (NASA). Space-Based Measurements of Ozone and Air Quality in the Ultraviolet and Visible. <http://ozoneaq.gsfc.nasa.gov/> Accessed January 31, 2012.

Mishev A., A. Bouklijski and J. Stamenov. 2008. Lead free Neutron Monitor at Basic Environmental Observatory Moussala - first measurements

<http://ecrs2008.saske.sk/dvd/s3.23.pdf>, Accessed February 7, 2012.

NASA. 2001. Pioneer 10 exhibit and the heliosphere solar systems.

<http://www.nasa.gov/centers/ames/news/releases/2001/01images/Pioneer10/pioneer10.html>. Accessed January 10, 2012.

Newman, Dr. Paul A. 2000. What's Happening To Stratospheric Ozone Over The Arctic, And Why? USGRCP Seminar, 14 July 2000, Updated August 2004

<http://www.usgrcp.gov/usgrcp/seminars/000714FO.html>. Accessed January 31, 2012.

NOAA Earth System Research Laboratory Chemical Sciences Division. 2008. ARCPAC:

Aerosol, Radiation and Cloud Processes affecting Arctic Climate, Science and Implementation Plan. <http://www.esrl.noaa.gov/csd/arcpac/>. Accessed January 31, 2012.

- NOAA National Geophysical Data Center; Cosmic Ray Neutron Monitor Data,  
<http://ngdc.noaa.gov/stp/solar/cosmic.html>. Accessed November 9, 2011.
- Ozone Monitoring Instrument (OMI): Optical Assembly. Last update December 16,  
 2008. (<http://www.knmi.nl/omi/research/instrument/optic.php?tag=full>).  
 Accessed January 31, 2012.
- Remer, Lorraine. 2011. NASA Earth Observatory.  
 2012<http://earthobservatory.nasa.gov/IOTD/view.php?id=49874>. Accessed March  
 1, 2012.
- Rossow, William B., Alison W. Walker, Diane E. Beuschel, Miriam D. Roiter. 1996.  
 International Council of Scientific Unions and World Meteorological Organization  
 World Climate Research Programme – International Satellite Cloud Climatology  
 Project (ISCCP) Documentation of New Cloud Datasets.  
<http://isccp.giss.nasa.gov/pub/documents/d-doc.pdf>. Accessed February 12,  
 2012.
- Rossow, William B. 2011. Personal communication.
- Spaceship Earth. 2000. Cosmic Rays on Spaceship Earth.  
<http://neutronm.bartol.udel.edu/catch/title.html>. Spaceship Earth is supported  
 by the United States National Science Foundation under grants ANT-0739620 and  
 ANT-0838839, and by the University of Delaware Department of Physics and  
 Astronomy and Bartol Research Institute. Accessed February 2, 2012.
- Sunrise and Sunset in Qaanaaq. 2012.  
 . Accessed February 7, 2012.
- Svensmark, Henrik et al. 2010. The Nature of Things: When North Goes South. Air date  
 January 5, 2012.
- Tropospheric Emission Monitoring Internet Service (TEMIS); Tropospheric Data Products.  
 2011. <http://www.temis.nl/protocols/O3global.html> Accessed February 12, 2011
- Ulysses Mission Report. Solar Wind Loses Power, Hits 50-year Low. 09.23.2008.  
[http://science.nasa.gov/headlines/y2008/23sep\\_solarwind.htm](http://science.nasa.gov/headlines/y2008/23sep_solarwind.htm). Accessed January  
 2, 2012.
- Ulysses Website, University of New Hampshire. Cosmic Ray Overview.  
<http://ulysses.sr.unh.edu/NeutronMonitor/Misc/neutron2.html>. Accessed  
 February 12, 2012.
- U.S. Environmental Protection Agency. Updated 2012. Ozone Layer Protection.

<http://www.epa.gov/ozone/strathome.html>. Accessed January 27, 2012.

Welch, Charles with original documentation by the British Antarctic Study, NASA, Environment Canada, UNEP, EPA and other sources. 2011. The Ozone Hole. <http://www.theozonehole.com/arcticozone.htm>. Accessed February 26, 2012.

## APPENDIX A

To further understand the current density that exists at layer cloud boundaries, physical laws of nature must be applied [the following is extracted from Harrison and Ambaum, 2008]. For a simple, horizontally extensive one-dimensional cloud, as depicted in Figure 2.4, the space charge density at the cloud base is explained by both Ohm's and Gauss' Laws,

$$J_c = \sigma * E \quad (A.1)$$

where  $E$  is the vertical electric field and  $\sigma$  is the air conductivity and

$$\frac{dE}{dz} = \frac{\rho}{\epsilon} \quad (A.2)$$

where  $\epsilon$  is the permittivity of the cloud layer

The vertical heterogeneity of the current disappears during semi-stable background conditions and  $\rho$  is defined as:

$$\rho = -\epsilon J_c \frac{d}{dz} \left( \frac{1}{\sigma} \right) \quad (A.3)$$

where  $\sigma$  is the total conductivity understood as

$$\sigma = e(\mu_+ n_+ + \mu_- n_-) \quad (A.4)$$

where  $\mu_{\pm}$  describes the bipolar ion mobilities,  $n_{\pm}$  defines the bipolar ion number concentrations and  $e$  is the elementary charge.

$n_{\pm}$  are inversely proportional to the radius-dependent, ion-capture coefficients  $\beta_{\pm}$  written as

$$n_{\pm} = \frac{q}{Z\beta_{\pm}} \quad (\text{A.5})$$

where  $Z$  is the droplet concentration and  $q$  is the volumetric ion production rate.

Based on values determined for  $\beta_{\pm}$ , the following equation is established:

$$\sigma = \frac{2q\varepsilon}{|j|Z} \sinh(2\lambda|j|) \quad (\text{A.6})$$

where  $|j|$  is the absolute value of elementary charges for a single droplet and the droplet radius is defined as:

$$\lambda = \frac{e^2}{(8\pi\varepsilon akT)} \quad (\text{A.7})$$

where  $k$  is Boltzmann's constant and  $T$  is the ambient temperature.

When  $\lambda|j|$  is small,  $\sinh(2\lambda|j|)$  is linearized in a manner such that:

$$\frac{\sigma_{haze}}{\sigma_{cloud}} \geq \frac{a_{cloud}}{a_{haze}} \quad (\text{A.8})$$

where  $a_{cloud}$  is the cloud droplet radii and  $a_{haze}$  is the haze droplet radii

In the condition where  $a_{cloud}$  and  $a_{haze}$  vary by an at least one order of magnitude from each other, the conductivity will be an order of magnitude smaller compared to the conductivity existing in the haze layer below the cloud. In this state where  $\sigma_{cloud} \ll \sigma_{haze}$ , equation (4) becomes

$$\rho \approx -(\epsilon J_c) / D \sigma_{cloud} \quad (\text{A.9})$$

where  $D$  is the depth of the haze to cloud transition layer.

If an assumption is made that all of the charge within a cloud is carried by its droplets

$$\rho = -Zj_e \quad (\text{A.10})$$

then,

$$\sinh(2\lambda|j|) = \frac{J_c}{2Deq} \quad (\text{A.11})$$

From this series of equations, the following scenario can be established. For the depth of the haze cloud transition layer,  $D$ , of 1-10m,  $a_{cloud}$  is approximately 10-100  $\mu\text{m}$ ,  $J_c$  is 1-2  $\text{pAm}^{-2}$  and  $q$  ranges from 2 to  $5 \cdot 10^6$  ion pairs  $\text{m}^{-3}\text{s}^{-1}$ . In this situation,  $j$ , the value of elementary charges for a single droplet, increases to about 1000. This droplet charge would be adequate enough to reduce the critical supersaturation as defined by Figure 2.6.

## APPENDIX B

### ISCCP Data Products

Record Variables	Description	Units
SATTYP	Satellite Type code	unitless
NCHANS	Number of channels	unitless
IWEST	Western-most longitude	degrees
IEAST	Eastern-most longitude	degrees
INORTH	Northern-most latitude	degrees
ISOUTH	Southern-most latitude	degrees
NPIX	Number of pixels reported in data area	unitless
IOUT	Number of bytes packed in data buffer	unitless
LONBUF(NPIX)	Longitudes for NPIX pixels	degrees

LATBUF(NPIX)	Latitudes for NPIX pixels	degrees
XBUF(NPIX)	X-positions for NPIX pixels (1-1440)	unitless
YBUF(NPIX)	Y-positions for NPIX pixels (1-550)	unitless
<hr/>		
DX Data Variables	Description	Units
LNDWTR	Land/water flag (0-1) 1 = Water pixel	unitless
HITOPO	Topography flag (0-1) 1 = high topography pixel	unitless
SNOICE	Snow/ice code (0-3) 0 = no sea ice (water), no snow or ice (land) 1 = partial ice cover (water), ice (land) 2 = full ice cover (water), full snow cover (land) 3 = ice margin (water), snow or ice margin (land)	unitless
MUE	Cosine of satellite zenith angle*100 (0-100)	unitless
IRAD	IR radiance (0-254 counts)	Kelvin
GLINT	Glint flag (0-1) 1 = glint condition exists	unitless
MUO	Cosine of solar zenith angle*100 (0-100)	unitless
PHI	Relative azimuth angle (0-180)	degrees
VRAD	VIS radiance (0-254 counts)	unitless
DAYNIT	Day / Night flag 0 = Day pixel 1 = Night pixel	unitless
ITHR	Final IR threshold result (0-5) 4,5 - cloudy	unitless
VTHR	Final VIS threshold result (0-5) 4,5 - cloudy	unitless
SHORE	Shore flag (0-1) 1 = near-coastal pixel	unitless
IRET	IR retrieval code (0-12)	unitless
ICSRET	IR clear sky composite retrieval code (0-12)	unitless
ICSRAD	IR clear sky composite radiance (0- 254 counts)	
ITMP	IR-retrieved cloud top or surface temperature (0-254 counts)	Kelvin
IPRS	IR-retrieved cloud top or surface pressure (0-254 counts)	millibars

ICSTMP	IR-retrieved clear sky composite temperature (0-254 counts)	Kelvin
ICSPRS	IR-retrieved clear sky composite pressure (0-254 counts)	millibars
NREF	NIR reflectivity (0-254 counts)	
NTHR	NIR threshold result (1-13) >8 = cloudy	unitless
NCSREF	NIR clear sky composite reflectance (0-254 counts)	
VRET	VIS retrieval code (0-14)	unitless
VCSRET	VIS clear sky composite retrieval code (0-14)	unitless
VCSRAD	VIS clear sky composite radiance (0-254 counts)	
VALBTA	VIS-retrieved liquid cloud tau or surface reflectance (0-254 counts)	
VCSALB	VIS-retrieved clear sky composite reflectance (0-254 counts)	
VTMP	VIS-adjusted cloud top temperature (0-254 counts)	Kelvin
VPRS	VIS-adjusted cloud top pressure (0-254 counts)	millibars
VTAUIC	VIS-retrieved ice cloud tau (0-254 counts)	unitless
VTMPIC	VIS-adjusted ice cloud top temperature (0-254 counts)	Kelvin
VPRPIC	VIS-adjusted ice cloud top pressure (0-254 counts)	millibars

[from Rossow, et al. 1996]

## APPENDIX C

### ICARE DARDAR Data Products

Variables (one-dimensional)	Description	Units
time	Time UTC	seconds
latitude	Latitude of co-located CloudSat-Calipso footprints on the ground	degrees
longitude	Longitude of co-located CloudSat-Calipso footprints on the ground	degrees
vis_optical_depth	Visible Optical Depth; Line integral of ice cloud visible extinction along a vertical path through the atmosphere	unitless
vis_optical_depth_error	Visible Optical Depth Error	unitless
day_night_flag	Day night flag for lidar 0 = night 1 = day	unitless
land_water_mask	Land water mask, indicating the	unitless

	surface type at the laser footprint, from Calipso files	
	0=shallow ocean	
	1=land	
	2=coastline	
	3=shallow inland water	
	4=intermittent water	
	5=deep inland water	
	6=continental ocean	
	7= deep ocean	
Tropopause_Height	Altitude to estimated height of tropopause	meters
height	Altitude of radar and lidar common range gates above mean sea level	meters
n_iterations	Number of iterations before convergence	unitless
wavelength	Wavelength of center of radiance (infrared) channel	meters
<b>Variables (two-dimensional)</b>	<b>Description</b>	<b>Units</b>
chi2	Chi squared value for each iteration	unitless
chi2_split	Chi-squared value for final iteration for each type of measurement, normalized by number of gates	unitless
radiance	Forward-modeled radiance	$W/m^2 * um * sr$
radiance_sat	Satellite radiance	$W/m^2 * um * sr$
radiance_flag	Radiance flag	
	0 = radiance not used	
	1= radiance used	unitless
radiance_difference_flag	Radiance difference flag	
	0 = radiance not used	
	1= first radiance used	
	2= second radiance used	
	3= third radiance used	unitless
Z	Radar reflectivity	$mm^6/m^3$
bscat	Lidar attenuated backscatter	$1/m * sr$
bscat_perp	Perpendicular lidar attenuated backscatter	$1/m * sr$
DARMASK_Simplified_Categorization	DARDAR categorization	
	-9 = ground	
	-1 = unidentified	
	0 = clear	
	1 = ice	
	2= ice + supercooled	
	3 = liquid warm	unitless

	4 = supercooled	
	5 = rain	
	6 = aerosol	
	7 = maybe insects	
	8 = stratospheric feature	
Target_Lidar_Mask	Target Lidar Mask	unitless
instrument-flag	Instrument flag	
	0 = nothing	
	1 = lidar	
	2 = radar	
	3 = radar+lidar)	unitless
Z_fwd	Forward-modelled 94 GHz radar reflectivity factor	$mm^6/m^3$
bscat_fwd	Forward-modelled lidar attenuated backscatter	$1/m * sr$
extinction	Retrieved visible extinction coefficient	$1/m$
lidar_ratio	Retrieved extinction-to-backscatter ratio	$sr$
iwc	Retrieved ice water content (mass of ice per unit volume of air)	$kg/m^3$
effective radius	Retrieved effective radius, proportional to the ratio of ice water content to visible extinction coefficient	meters
NOstar	Retrieved intercept parameter NO* of the normalized size distribution of ice particles	$1/m^4$
ln_extinction_error	1-sigma random error in natural logarithm of visible extinction coefficient	$\ln(1/m)$
ln_lidar_ratio_error	1-sigma random error in natural logarithm of extinction-to-backscatter ratio	$\ln(sr)$
ln_iwc_error	1-sigma random error in natural logarithm of iwc	$\ln(kg/m^3)$
ln_effective_radius_error	1-sigma random error in natural logarithm of effective radius	$\ln(1/m)$
ln_NO_error	1-sigma random error in natural logarithm of normalized number concentration parameter	$\ln(1/m^4)$
temperature	Temperature from ECMWF	Kelvin

## APPENDIX D

SBUV data showing dates past June 10, 1993 when data was both available from the source and used for this study. The used data was averaged with TOMS and OMI data to complete the dataset for analytical purposes.

SBUV N-14 Data				SBUV N-11 Data			
Available		Data Used		Available		Data Used	
From	To	From	To	From	To	From	To
				10/06/1993	12/06/1993	10/06/1993	12/06/1993
				18/06/1993	20/06/1993	18/06/1993	20/06/1993
				26/06/1993	28/06/1993	26/06/1993	28/06/1993
				04/07/1993	06/07/1993	04/07/1993	06/07/1993
				12/07/1993	14/07/1993	12/07/1993	14/07/1993
				20/07/1993			
				22/07/1993	23/07/1993		
				29/07/1993	31/07/1993		
				06/08/1993	08/08/1993		
				14/08/1993	16/08/1993		
				22/08/1993	24/08/1993		
				30/08/1993	01/09/1993		
				07/09/1993	10/09/1993		
				16/09/1993	18/09/1993		
				24/09/1993	26/09/1993		
				02/10/1993	05/10/1993	02/10/1993	05/10/1993
				09/10/1993		09/10/1993	
				04/03/1994	07/03/1994		
				13/03/1994	15/03/1994		
				21/03/1994	24/03/1994		
				30/03/1994	01/04/1994		
				07/04/1994	09/04/1994		
				15/04/1994	17/04/1994		
				23/04/1994	25/04/1994		
				01/05/1994	03/05/1994	01/05/1994	03/05/1994
				09/05/1994	11/05/1994	09/05/1994	11/05/1994
				17/05/1994		17/05/1994	
				19/05/1994		19/05/1994	
				25/05/1994	27/05/1994	25/05/1994	27/05/1994
				02/06/1994	04/06/1994		
				10/06/1994	12/06/1994		
				18/06/1994	20/06/1994		
				27/06/1994	29/06/1994		
				05/07/1994	07/07/1994	06/07/1994	07/07/1994

				13/07/1994	13/07/1994
				15/07/1994	15/07/1994
				21/07/1994	23/07/1994
				21/07/1994	23/07/1994
				29/07/1994	31/07/1994
				29/07/1994	31/07/1994
				06/08/1994	08/08/1994
				06/08/1994	08/08/1994
				14/08/1994	16/08/1994
				14/08/1994	16/08/1994
				22/08/1994	24/08/1994
				22/08/1994	24/08/1994
				30/08/1994	01/09/1994
				30/08/1994	01/09/1994
				07/09/1994	09/09/1994
				07/09/1994	09/09/1994
				15/09/1994	17/09/1994
				15/09/1994	17/09/1994
				24/09/1994	25/09/1994
				24/09/1994	25/09/1994
				02/10/1994	03/10/1994
				02/10/1994	03/10/1994
				12/03/1995	14/03/1995
				12/03/1995	14/03/1995
				20/03/1995	22/03/1995
				20/03/1995	22/03/1995
27/03/1995	31/03/1995	27/03/1995		28/03/1995	30/03/1995
				28/03/1995	30/03/1995
				15/07/1997	17/07/1997
16/04/1995	19/04/1995	16/04/1995	19/04/1995	23/07/1997	
26/04/1995		26/04/1995		25/07/1997	
28/04/1995		28/04/1995		31/07/1997	02/08/1997
05/05/1995	08/05/1995	05/05/1995	08/05/1995	08/08/1997	10/08/1997
14/05/1995	17/05/1995	14/05/1995	17/05/1995	16/08/1997	18/08/1997
24/05/1995	26/05/1995	24/05/1995	26/05/1995	24/08/1997	26/08/1997
02/06/1995	04/06/1995	02/06/1995	04/06/1995	01/09/1997	03/09/1997
11/06/1995	14/06/1995	11/06/1995	14/06/1995	09/09/1997	11/09/1997
20/06/1995	23/06/1995	20/06/1995	23/06/1995	17/09/1997	19/09/1997
30/06/1995		30/06/1995		25/09/1997	27/09/1997
01/07/1995	02/07/1995	01/07/1995	02/07/1995	03/10/1997	05/10/1997
09/07/1995	10/07/1995	09/07/1995	10/07/1995	12/10/1997	
12/07/1995		12/07/1995		03/03/1998	05/03/1998
18/07/1995	21/07/1995	18/07/1995	21/07/1995	11/03/1998	13/03/1998
28/07/1995	30/07/1995	28/07/1995	30/07/1995	19/03/1998	21/03/1998
06/08/1995	09/08/1995	06/08/1995	09/08/1995	27/03/1998	29/03/1998
15/08/1995	18/08/1995	15/08/1995	18/08/1995	04/04/1998	06/04/1998
24/08/1995		24/08/1995		12/04/1998	14/04/1998
26/08/1995	27/08/1995	26/08/1995	27/08/1995	20/04/1998	22/04/1998
03/09/1995	05/09/1995	03/09/1995	05/09/1995	28/04/1998	30/04/1998
12/09/1995	15/09/1995	12/09/1995	15/09/1995	06/05/1998	
08/03/1996		08/03/1996		14/05/1998	16/05/1998
25/03/1996	27/03/1996	25/03/1996	27/03/1996	31/05/1998	01/06/1998
03/04/1996	05/04/1996	03/04/1996	05/04/1996	07/06/1998	09/06/1998
12/04/1996	14/04/1996	12/04/1996	14/04/1996	15/06/1998	17/06/1998
21/04/1996	24/04/1996	21/04/1996	24/04/1996	23/06/1998	25/06/1998
01/05/1996	03/05/1996	01/05/1996	03/05/1996	01/07/1998	03/07/1998

10/05/1996	12/05/1996	10/05/1996	12/05/1996	09/07/1998	11/07/1998
19/05/1996	21/05/1996	19/05/1996	21/05/1996	17/07/1998	19/07/1998
29/05/1996	31/05/1996	29/05/1996	31/05/1996	26/07/1998	27/07/1998
06/06/1996		06/06/1996		02/08/1998	04/08/1998
15/06/1996	18/06/1996	15/06/1996	18/06/1996	10/08/1998	12/08/1998
25/06/1996	27/06/1996	25/06/1996	27/06/1996	18/08/1998	20/08/1998
04/07/1996	06/07/1996	04/07/1996	06/07/1996	26/08/1998	28/08/1998
13/07/1996	15/07/1996	13/07/1996	15/07/1996	03/09/1998	05/09/1998
22/07/1996	26/07/1996	22/07/1996	24/07/1996	10/09/1998	13/09/1998
31/07/1996				18/09/1998	21/09/1998
01/08/1996	03/08/1996			26/09/1998	29/09/1998
10/08/1996	12/08/1996			04/10/1998	07/10/1998
19/08/1996	21/08/1996			06/03/1999	07/03/1999
28/08/1996	31/08/1996			13/03/1999	15/03/1999
06/09/1996	09/09/1996			21/03/1999	23/03/1999
15/09/1996	17/09/1996			29/03/1999	31/03/1999
26/03/1997	30/03/1997			06/04/1999	08/04/1999
05/04/1997	08/04/1997			14/04/1999	16/04/1999
14/04/1997	17/04/1997			22/04/1999	24/04/1999
24/04/1997	26/04/1997			30/04/1999	02/05/1999
03/05/1997	05/05/1997			08/05/1999	
12/05/1997	14/05/1997			10/05/1999	
21/05/1997	24/05/1997			16/05/1999	18/05/1999
30/05/1997	01/06/1997			23/05/1999	26/05/1999
08/06/1997	11/06/1997			01/06/1999	02/06/1999
17/06/1997	20/06/1997			08/06/1999	10/06/1999
26/06/1997	29/06/1997			15/06/1999	18/06/1999
06/07/1997	08/07/1997			24/06/1999	26/06/1999
15/07/1997	17/07/1997			02/07/1999	04/07/1999
24/07/1997	26/07/1997			10/07/1999	12/07/1999
02/08/1997	05/08/1997			18/07/1999	20/07/1999
11/08/1997	14/08/1997			26/07/1999	27/07/1999
20/08/1997	23/08/1997			02/08/1999	05/08/1999
29/08/1997	01/09/1997			10/08/1999	12/08/1999
07/09/1997	10/09/1997			18/08/1999	20/08/1999
16/09/1997	18/09/1997			26/08/1999	28/08/1999
25/03/1998	28/03/1998			03/09/1999	05/09/1999
03/04/1998	06/04/1998			11/09/1999	13/09/1999
12/04/1998	15/04/1998			19/09/1999	21/09/1999
21/04/1998	24/04/1998			26/09/1999	28/09/1999
01/05/1998	03/05/1998			05/10/1999	07/10/1999
09/05/1998	13/05/1998			14/10/1999	
18/05/1998	21/05/1998			02/03/2000	04/03/2000

28/05/1998	30/05/1998		09/03/2000	11/03/2000	
09/06/1998			17/03/2000	19/03/2000	
15/06/1998	17/06/1998		25/03/2000	27/03/2000	
03/07/1998	05/07/1998		01/04/2000	03/04/2000	
12/07/1998	14/07/1998		09/04/2000	11/04/2000	
21/07/1998	23/07/1998		17/04/2000	19/04/2000	
30/07/1998	01/08/1998		25/04/2000	27/04/2000	
08/08/1998	10/08/1998		02/05/2000	04/05/2000	
18/08/1998	19/08/1998		10/05/2000	12/05/2000	
26/08/1998	28/08/1998		18/05/2000	20/05/2000	
04/09/1998	06/09/1998		26/05/2000	29/05/2000	
12/09/1998	15/09/1998		02/06/2000	04/06/2000	
29/03/1999	01/04/1999		10/06/2000	12/06/2000	
07/04/1999	09/04/1999		18/06/2000	20/06/2000	
16/04/1999	19/04/1999		26/06/2000	28/06/2000	
25/04/1999	27/04/1999		03/07/2000	05/07/2000	
04/05/1999	06/05/1999		11/07/2000	13/07/2000	
13/05/1999	15/05/1999		19/07/2000	21/07/2000	
22/05/1999	24/05/1999		26/07/2000	28/07/2000	
30/05/1999	02/06/1999		03/08/2000	05/08/2000	
08/06/1999	11/06/1999		11/08/2000	12/08/2000	
17/06/1999	20/06/1999		19/08/2000	21/08/2000	
26/06/1999	28/06/1999		26/08/2000	28/08/2000	
05/07/1999	07/07/1999		03/09/2000	05/09/2000	
14/07/1999	16/07/1999		11/09/2000	13/09/2000	
22/07/1999	25/07/1999		18/09/2000	20/09/2000	
30/07/1999	02/08/1999		26/09/2000	28/09/2000	
09/08/1999	12/08/1999		04/10/2000	06/10/2000	
18/08/1999	20/08/1999		06/03/2001	08/03/2001	
27/08/1999	29/08/1999		13/03/2001	14/03/2001	
05/09/1999	07/09/1999		21/03/2001	23/03/2001	
13/09/1999	14/09/1999				
20/09/1999					
01/04/2000	03/04/2000				
10/04/2000	12/04/2000				
18/04/2000	20/04/2000				
27/04/2000	29/04/2000				
05/05/2000	07/05/2000				
08/05/2000					
14/05/2000	16/05/2000				
22/05/2000	25/05/2000				
31/05/2000	03/06/2000				
09/06/2000	11/06/2000				

17/06/2000	19/06/2000		
26/06/2000	28/06/2000		
04/07/2000	07/07/2000		
13/07/2000	15/07/2000		
21/07/2000	24/07/2000		
30/07/2000	01/08/2000		
07/08/2000	10/08/2000		
16/08/2000	18/08/2000		
25/08/2000	27/08/2000		
02/09/2000	04/09/2000		
11/09/2000	13/09/2000		
31/03/2001	02/04/2001		
17/04/2001	19/04/2001		
25/04/2001	27/04/2001		
04/05/2001	06/05/2001		
12/05/2001	14/05/2001		
20/05/2001	22/05/2001		
29/05/2001	31/05/2001		
06/06/2001	08/06/2001		
14/06/2001	16/06/2001		
22/06/2001	25/06/2001		
01/07/2001	03/07/2001		
09/07/2001	11/07/2001		
17/07/2001	19/07/2001		
25/07/2001	28/07/2001		
03/08/2001	05/08/2001		
11/08/2001	13/08/2001		
19/08/2001	22/08/2001		
28/08/2001	30/08/2001		
05/09/2001	07/09/2001		
04/04/2002	06/04/2002		
12/04/2002	14/04/2002		
20/04/2002			
22/04/2002			
28/04/2002	01/05/2002		
06/05/2002	08/05/2002		
14/05/2002	16/05/2002		
22/05/2002	24/05/2002		
30/05/2002	01/06/2002		
07/06/2002	09/06/2002		
15/06/2002	17/06/2002		
23/06/2002	25/06/2002		
01/07/2002	03/07/2002		

09/07/2002	11/07/2002			
17/07/2002	19/07/2002			
25/07/2002	27/07/2002			
02/08/2002	04/08/2002	03/08/2002	04/08/2002	
10/08/2002	12/08/2002	10/08/2002	11/08/2002	
18/08/2002	20/08/2002			
26/08/2002	27/08/2002			
03/09/2002	06/09/2002			
12/09/2002				
27/09/2002				
03/10/2002				
10/03/2003	11/03/2003			
18/03/2003	20/03/2003			
26/03/2003	28/03/2003			
03/04/2003	04/04/2003			
11/04/2003	13/04/2003			
18/04/2003	19/04/2003			
21/04/2003				
27/04/2003	28/04/2003			
04/05/2003				
06/05/2003				
19/05/2003	21/05/2003	19/05/2003	21/05/2003	
28/05/2003	30/05/2003			
05/06/2003	07/06/2003			
13/06/2003	15/06/2003			
21/06/2003	23/06/2003			
28/06/2003	30/06/2003			
06/07/2003	08/07/2003			
14/07/2003	16/07/2003			
22/07/2003	24/07/2003			
30/07/2003	01/08/2003			
07/08/2003	09/08/2003			
15/08/2003	16/08/2003			
22/08/2003	28/08/2003			
07/09/2003	09/09/2003			
16/09/2003	17/09/2003			
23/09/2003	25/09/2003			
30/09/2003	03/10/2003			
05/03/2004				
11/03/2004	13/03/2004			
20/03/2004	21/03/2004			
24/03/2004				
26/03/2004	27/03/2004			

05/04/2004			
11/04/2004	13/04/2004		
19/04/2004	22/04/2004		
27/04/2004	29/04/2004		
06/05/2004	07/05/2004		
13/05/2004	14/05/2004		
20/05/2004	22/05/2004		
28/05/2004	30/05/2004		
05/06/2004	07/06/2004		
13/06/2004	15/06/2004		
28/06/2004	30/06/2004		
07/07/2004	08/07/2004		
14/07/2004	15/07/2004		
21/07/2004	24/07/2004		
30/07/2004	31/07/2004		
06/08/2004	09/08/2004		
14/08/2004	16/08/2004		
22/08/2004	24/08/2004		
05/03/2005	07/03/2005		
14/03/2005	15/03/2005		
21/03/2005	23/03/2005		
28/03/2005	30/03/2005		
05/04/2005	07/04/2005		
13/04/2005	15/04/2005		
21/04/2005			
23/04/2005			
28/04/2005	30/04/2005		
06/05/2005	08/05/2005		
14/05/2005	16/05/2005		
22/05/2005	24/05/2005		
29/05/2005	31/05/2005		
06/06/2005			
08/06/2005			
14/06/2005	16/06/2005		
22/06/2005	24/06/2005		
29/06/2005	30/06/2005		
07/07/2005	09/07/2005		
15/07/2005	17/07/2005		
25/07/2005			
30/07/2005	01/08/2005		
07/08/2005	09/08/2005		
15/08/2005	17/08/2005		
23/08/2005	25/08/2005		

31/08/2005	01/09/2005			
07/09/2005	09/09/2005			
15/09/2005	17/09/2005			
23/09/2005				
30/09/2005	02/10/2005			
08/10/2005				
26/02/2006		26/02/2006		
05/03/2006	07/03/2006			
11/03/2006	14/03/2006			
19/03/2006	21/03/2006			
27/03/2006	29/03/2006			
04/04/2006				
06/04/2006				
11/04/2006	13/04/2006			
26/04/2006	29/04/2006			